Characterization of Irradiated Zircaloys: Susceptibility to Stress Corrosion Cracking

NP-1557
Research Project 1027

Final Report, October 1980

Prepared by

ARGONNE NATIONAL LABORATORY
9700 South Cass Avenue
Argonne, Illinois 60439

Principal Investigators
F. L. Yaggee
R. F. Mattas
L. A. Neimark

Prepared for

Electric Power Research Institute
3412 Hillview Avenue
Palo Alto, California 94304

EPRI Project Manager
H. Ocken

Fuels, Waste, and Environment Program
Nuclear Power Division

ORDERING INFORMATION

Requests for copies of this report should be directed to Research Reports Center (RRC), Box 50490, Palo Alto, CA 94303, (415) 965-4081. There is no charge for reports requested by EPRI member utilities and affiliates, contributing nonmembers, U.S. utility associations, U.S. government agencies (federal, state, and local), media, and foreign organizations with which EPRI has an information exchange agreement. On request, RRC will send a catalog of EPRI reports.

NOTICE

Prepared by
Argonne National Laboratory
Argonne, Illinois

EPRI PERSPECTIVE

PROJECT DESCRIPTION

Utilities are guided by vendor proposals that limit the rate of power increases in nuclear fuel rods so as to minimize pellet-cladding interaction (PCI) failures. The phenomenon responsible for these failures is the stress corrosion cracking (SCC) of the Zircaloy cladding. The restrictions on the rate of power increases are undesirable; they lead to reduced plant capacity factors and the need to provide more costly replacement power. This project (RP1027) was designed to provide data on the SCC response of irradiated Zircaloy to aggressive iodine environments. Earlier results were reported in EPRI Interim Report NP-1155. The response of unirradiated Zircaloy subjected to similar tests was described in EPRI Final Reports NP-717 and NP-1329. These experimental data form the basis for a model of the SCC of Zircaloy that is being developed under RP700.

PROJECT OBJECTIVE

This study was initiated to determine the susceptibility of irradiated Zircaloy to iodine-induced SCC. The effects of preirradiation metallurgical condition, fluence, fission-product chemistry and morphology, and the role of the oxide layer that forms on the inner surface of the cladding were evaluated. The response of the cladding was determined by using tube burst tests, uniaxial tensile tests, scanning electron microscopy, and optical microscopy.

PROJECT RESULTS

Irradiation generally increases the susceptibility of Zircaloy to SCC. Tests on specimens obtained from fuel rods that had been exposed to at least one cycle of reactor operation showed that the minimum stress required to fail the specimens varied by less than 10%, regardless of the initial metallurgical condition of the cladding. In the absence of significant fission-product releases, a uniformly thick zirconium oxide layer that formed on the inner surface of one type of cladding reduced its susceptibility to SCC. Defining the conditions required to form and maintain this oxide intact over the entire irradiation history of a fuel rod would permit a simpler approach to a PCI-resistant fuel rod design than the barrier

designs being pursued in programs sponsored by the Department of Energy (DOE). SCC failures usually occurred at very low strains. Limited data suggest an inverse correlation between the yield strength of irradiated cladding and the threshold stress for SCC.

This report should be of interest to utility personnel with responsibilities in the area of reactor fuel design and performance.

H. Ocken, Project Manager
Nuclear Power Division

ABSTRACT

Irradiated Zircaloy cladding specimens that reached burnups from 6 to 30 MWd/kg U were exposed to iodine to investigate their stress corrosion cracking (SCC) susceptibility. Constant-stress and stress-change tests were performed. Cladding from several sources (including BWRs and PWRs) was tested. Test temperatures ranged from 320 to 360°C and applied hoop stresses ranged from 150 to 500 MPa (22 to 72 ksi). Two iodine concentrations, 6.0 and 0.6 mg/cm^2, were used. Failure times ranged from 360 s (0.1h) at high stresses to 5 x 10^5 s (142 h) at low stresses. The 24-h failure stress was 171 ± 18 MPa (24.8 ± 2.6 ksi) regardless of the preirradiation metallurgical condition for all specimens that reached a burnup >10 MWd/kg U. This failure stress is lower than is typically measured on unirradiated Zircaloy. The effect on SCC behavior of an oxide that formed on the inner surface of one cladding type was evaluated. Uniaxial tensile tests were performed on some specimens. An analytical model for iodine-induced SCC of Zircaloy was developed that correlates reasonably well with the measurements.

ACKNOWLEDGMENTS

We gratefully acknowledge the efforts and helpful contributions of ANL Engineering, Central Shops, and Materials Science Division personnel in the successful completion of the program work reported here. An expression of thanks is extended to H. Russell for equipment design, C. Hendrickson and F. Basso for hardware fabrication, R. Haglund for conducting the SCC tests, A. Baudino, F. Pausche, and C. Gebo for posttest optical microscopy and photography, D. Butler for tensile testing, and J. Sanecki for posttest scanning electron microscopy (SEM). An expression of appreciation is extended to the Electric Power Research Institute (EPRI) for program support, to H. Ocken (EPRI) for helpful comments, and D. Nellis (ANL) for typing and assemblying the manuscript.

CONTENTS

ILLUSTRATIONS

TABLES

SUMMARY

A study was conducted at Argonne National Laboratory (ANL) to address the problem of the susceptibility of irradiated Light Water Reactor (LWR) cladding to failure by stress-corrosion cracking (SCC), in the presence of iodine, during periods of pellet cladding interaction (PCI) in an operating LWR. Pellet-cladding interaction has been identified as a cause of fuel-rod failures during rapid power increases in commercial power reactors, when the accrued burnup of the fuel has achieved a level $\geq$10 MWd/kg U. In the present study laboratory techniques were used to simulate reactor operating conditions with respect to cladding stress and temperature and iodine concentration, while exercising a high degree of control over these test parameters. Iodine was used as the fission-product species because it has been shown that I_2 SCC fractures in Zircaloy closely resemble PCI failures in irradiated LWR cladding.

The ANL study investigated the susceptibility of irradiated Zircaloy to I_2 SCC failure as influenced by preirradiation metallurgical condition, fluence, and fission-product chemistry and oxide layer character on the cladding inner surface. Irradiated claddings from commercial Boiling Water Reactors (BWRs) and a Pressurized Water Reactor (PWR) were used, representing cladding fluences in the range 0.1 to 6 x 10^{21} n/cm^2 (E > 0.1 MeV). Unirradiated and irradiated Zircaloy-2 and -4 claddings were tested, in both the annealed and stress-relieved conditions. The I_2 SCC tests were conducted over the temperature range 320-360°C, the stress range 177-483 MPa (26-70 ksi), and iodine concentrations of 0.6 and 6.0 mg/cm^2. Test specimens included cladding from three BWR reactors [Oskarshamn-1 (Bu $\sim$13 MWd/kg U), Quad Cities-1 (Bu $\sim$8.5-11 MWd/kg U), and Big Rock Point (Bu 0.7, 7-8, and 17-24 MWd/kg U)] and one PWR reactor [H. B. Robinson (Bu $\sim$27-30 MWd/kg U)]. Test specimens from the Oskarshamn-1 BWR represented cladding from both failed and unfailed fuel rods, while all other specimens came from unfailed fuel rods. The results of tests with Oskarshamn-1, and Quad Cities-1 cladding and some tests with Big Rock Point and H. B. Robinson cladding were reported in an interim report, EPRI NP-1155 (September 1979).

The I_2 SCC tests were conducted in the Alpha-Gamma Hot Cell Facility on (nominally) 15-cm-long specimens with the fuel removed. Analytical-grade iodine crystals (~25 and 250 mg) were added to the internal volume of the tube specimen before sealing the ends, and the specimen hoop stress was generated by internal gas pressure loading with either helium or argon. Curves relating hoop stress and the time to failure by I_2 SCC were determined for each cladding type. The low-stress portion of the S-shaped I_2 SCC curve represents a minimum (threshold) stress required to cause SCC cladding failure. Because this low-stress portion of the curve had a slightly negative slope, the stress at 24 h in all cases was considered to be the threshold stress because of the relationship of this period to in-reactor failure times. This portion of the I_2 SCC curve was determined by increasing the specimen pressure incrementally after each 24-h period until specimen failure occurred. The high-stress portion of the same curve was determined by maintaining the specimen pressure constant at levels required to produce hoop stresses of 276 and 483 MPa (40 and 70 ksi) until specimen SCC failure occurred.

Cumulative damage tests under I_2 SCC conditions were also conducted on a limited number of cladding specimens. In these tests the hoop stress was held constant for half the time to failure, as determined from previous SCC tests, and increased or decreased rapidly to a second constant stress level and held until specimen failure occurred.

In addition, a small number of uniaxial tensile tests were conducted on tubular specimens of Big Rock Point and Quad Cities cladding. The purpose of these tests was to establish whether tensile data can be used as an indicator of SCC susceptibility, as well as to obtain data on the work-hardening characteristics of irradiated cladding.

Posttest examinations were conducted on a representative number of failed specimens using both scanning electron microscopy (SEM) and optical light microscopy. The SEM examination was used to confirm SCC failure and to obtain detailed information on the morphology of the fracture surface. Stress-corrosion cracking failures by rupture, axial crack formation, and pinhole leakage were examined. Optical microscopy was used to determine the path of the through-wall cladding breach, to detect incipient inner-surface cracking and crack branching during crack propagation, and to determine the thickness and the uniformity of the inner-outer-surface oxide layers. Similar SEM and metallographic characterizations were carried out on untested sibling specimens to ascertain the pretest condition of the cladding.

The results of the ANL study indicate that irradiated LWR cladding is more susceptible to I_2 SCC failure than unirradiated cladding of the same type, that this susceptibility increases with increasing cladding fluence, that susceptibility is sensitive to fission-product release and deposition in the individual fuel rod, and that the morphology of the fracture surface varies with the stress and temperature at which the I_2 SCC failure occurs. Also, a uniformly thick, high-quality oxide layer on the inner cladding surface can afford a degree of protection to I_2 SCC in the absence of gross cesium compound deposits on the cladding. Failure by the rupture mode predominated at high stresses; failure by pinhole mode predominated at low (threshold) stresses. Failure by the axial cracking mode occurred at intermediate stresses. Although differences in threshold-stress levels for different claddings could be discerned within ±8 MPa, the average threshold stress for all claddings at fluences $>1 \times 10^{21}$ n/cm^2 (>0.1 MeV), or fuel burnups ~10 MWd/kg U, is 171 ± 30 MPa at 325°C regardless of fission-product deposition on the cladding. The limited tensile test data suggest a linear correlation between postirradiation yield strength and the SCC threshold stress, the higher the yield stress the lower the threshold stress. Such a correlation suggests that the effect of cladding fluence on the threshold stresses arises from the higher yield stress as a function of fluence. The results of the complete cumulative-damage test matrix are compatible with linear cumulative damage.

An analytical model was developed for the I_2 SCC failure of irradiated Zircaloy cladding based on the test results and the posttest observation that SCC failure initiates by intergranular fracture at the inner surface and changes to cleavage and fluting fracture at some point during crack growth. The model assumes that the initiating intergranular fracture can be the result of chemical attack by iodine, while the cleavage and fluting fracture can be treated by the methods of linear elastic fracture mechanics (LEFM). An important feature of the model is that it incorporates mechanical-property parameters which can be determined independently by other testing methods. The time to I_2 SCC failure, t_f, for an irradiated cladding specimen is predicted to be

$$t_f = \frac{B}{A_o}\left[\exp\left(\frac{K^2_{ISCC}}{y^2\sigma^2 B}\right) - 1\right] + \frac{C}{\sigma^4 y^4}\left[\frac{\sigma^2 y^2}{K^2_{ISCC}} - \frac{\sigma_B}{W(\sigma_B - \sigma)}\right]$$

where t_f is the time to failure, A_o, B, and C are rate constants, K_{ISCC} is the threshold-stress intensity for cleavage and fluting fracture, y is a geometric constant, σ is the applied stress, W is the cladding wall thickness, and σ_B is the burst stress of the cladding.

Section 1

INTRODUCTION

BACKGROUND

Pellet-cladding interaction (PCI) has been identified as a cause of fuel-rod failures in commercial reactors. These failures have usually occurred in fuel rods that had experienced a fuel burnup $\geq$10 MWd/kg U and were then subjected to a rapid power transient. To minimize PCI failures, fuel vendors introduced reactor operational procedures to reduce the risk of unacceptable power increases to old and reshuffled fuel rods. These procedures, while workable, can be expensive in terms of lost plant output. Therefore, a strong incentive exists to provide a more quantitative understanding and control of the PCI phenomena to enable operating restrictions to be relaxed and eventually removed.

Cracks examined in failed fuel rods are tight and exhibit little or no gross plastic deformation (1). They are usually located at pellet-pellet interfaces, often adjacent to fuel-pellet cracks. The fracture surfaces consist predominantly of cleavage-like planes with a small percentage of fluting. The cleavage-like planes are regions of flat, featureless surface that have been interpreted to be the result of chemically assisted cleavage along crystal planes that are close to the basal plane; the fluting has been interpreted as plastic failure of grains not properly oriented for cleavage (2). The PCI crack characteristics are typical of failures due to stress-corrosion cracking (SCC) (3). The aggressive species are believed to be fission products produced during irradiation. Early laboratory tests were aimed at comparing SCC cracks with PCI failures. Rosenbaum et al. (4) first showed that fission-product iodine produced SCC fractures which closely resembled PCI failures. More recently, it was shown that the fracture surfaces of Zircaloy specimens that failed in either cadmium or cesium environments also closely resembled PCI fracture surfaces (5). However, iodine is viewed as the fission product mostly likely responsible for PCI failures. It provides the most representative results in laboratory tests, and thus practically all laboratory tests to date have been concerned with the effects of iodine on the SCC of Zircaloy.

OBJECTIVES AND SCOPE

The present program was undertaken to investigate the influence of microstructure, fission-product chemistry, and mechanical properties on the susceptibility of irradiated Zircaloy cladding to iodine SCC. Several cladding sources were used in the program, and both PWR and BWR claddings were tested. The results of the program are expected to aid in the development of PCI models that can more accurately predict fuel-rod failure conditions, and to provide insight into the mechanisms responsible for iodine SCC.

The work performed in the program is divided into four tasks:

1. SCC susceptibility
2. Inner-surface and substructure characterization
3. Mechanical properties
4. Data analysis

The SCC susceptibility tests consist of short term (<200 h) biaxial gas-pressurization tests in an iodine environment. Two types of SCC tests have been used in the program. The first type involved holding the stress and temperature levels constant until failure occurred in the cladding. The second type, designed to assess cumulative damage effects, was similar to the first except that the stress level was changed during the test to establish the effects of prior stress history on the time to failure. The surface and substructure characterization consisted of cladding examinations by scanning electron microscopy (SEM), energy-dispersive X-ray analysis, and optical metallography. The objectives of these examinations were to characterize the fission-product deposits on the cladding inner surface, the inner-surface oxide film, and the deformation and fracture at the SCC failure sites. The mechanical-property tests consisted of uniaxial tensile tests at elevated temperature. The purpose of these tests was to determine the work-hardening characteristics of irradiated cladding and to determine a relationship between tensile properties and SCC susceptibility. The data-analysis task combined the results of the other tasks to develop a coherent picture of the factors that may control the SCC of Zircaloy cladding.

This final report emphasizes the work completed since an interim report, EPRI-1155 (6), was issued in September 1979. The interim report presented the details of specimen preparation, equipment, test procedures, pre- and posttest cladding charac-

terization by metallography and SEM, the then available iodine SCC test results, and a preliminary empirical/mechanistic model that explained the SCC crack-propagation process. The available SCC data that was reported consisted of the low-stress regime for H. B. Robinson (HBR) cladding at 633 K; the low- and high-stress regimes* for Oskarshamn-I (OSK-I) cladding at 617 K; the low- and high-stress regimes for Quad Cities (QC) cladding at 598 K; and the low-stress regime for medium- and high-burnup Big Rock Point (BRP) cladding at 598 K. The additional work that has been done includes the high-stress SCC regime for HBR cladding at 633 K; high-stress tests with HBR cladding at 598 K to determine the effect of test temperature; the high-stress regime for high-burnup BRP cladding at 598 K; the low- and high-stress regimes at 598 K for high-burnup BRP cladding from high-fission-gas-release rods; the low-stress regime at 598 K for medium burnup BRP cladding from a high-fission-gas-release rod and additional data points for a low-gas-release rod; and the low- and high-stress regimes for low-burnup BRP cladding at 598 K. Also cumulative-damage SCC tests were conducted with QC and high-burnup BRP cladding, and uniaxial tensile tests were conducted with the QC and low-burnup BRP cladding. In addition, pretest and posttest cladding characterization was performed for fuel rods not previously used in the program. Where appropriate the earlier data are reported with the additional data for continuity.

*"Low"- and "high"-stress regimes are used here to describe the "flat" and "ascending" portions, respectively, of the complete SCC stress vs. time-to-failure curve. In some cases the magnitude of the "low"-stress values is actually greater than that of some "high"-stress values.

Blank

Section 2

CLADDING CHARACTERIZATION

CLADDING MATERIALS

The cladding materials tested in this program came from a number of different sources. These cladding sources are summarized in Table 2-1. The Zircaloy-4 cladding came from the H. B. Robinson (HBR) reactor and is the only PWR cladding used in the program. The annealed Zircaloy-2 cladding came from the Quad Cities I (QC) reactor; the cold-worked, stress-relieved Zircaloy-2 cladding came from the Big Rock Point (BRP) reactor. The cladding fluence ranged from 0.1 to 6 x 10^{21} n/cm^2 (E > 0.1 MeV).

SUMMARY OF PREVIOUS CHARACTERIZATIONS

The surface oxides, hydride content, and inner surfaces of most of the claddings were characterized earlier (6). The hydrides and surface oxides were characterized by optical metallography and their characteristics are summarized in Table 2-2. In general, the hydride concentration was low (<100 ppm by weight), which indicates that the hydrogen pickup during irradiation was small. The inner-surface oxides were nonuniform and varied from <1 to 18 μm in thickness, except for the medium-burnup (8-10 MWd/kg U) BRP cladding. This inner-surface oxide was uniformly thick (3-4 μm) around the entire circumference of the cladding.

The inner surfaces of the various claddings were characterized by scanning electron microscopy (SEM) and energy-dispersive X-ray analysis. Both the HBR and QC cladding were relatively clean and free of deposits. Fuel particles were randomly scattered over the surface, and wormlike or nodular growths, which have been observed in most irradiated claddings, were also present. No fission products were detected, except for cesium. The medium-burnup BRP cladding (165E) exhibited a charge buildup in the SEM that is an indicator of the nonconducting nature of the inner surface. Light circular areas, ~100 μm in diameter, were observed on the surface. These areas were structurally similar to the surrounding areas, but they contained high uranium and cesium concentrations. Wormlike growths were also observed. The high-burnup BRP cladding (165W) exhibited significant fuel/cladding

Table 2-1

SUMMARY OF IRRADIATED ZIRCALOY CLADDING MATERIALS

Material	Condition	Reactor	Rod Vendor	Tube Fabricator	Fuel Burnup (MWd/kg U)	Fluence (10^{21} n/cm^2, >0.1 MeV)	Nominal Dimensions (mm) OD	Nominal Dimensions (mm) Wall	Ovality	Rod No.	ANL No.	Gas Release %
Zircaloy-2	Annealed	OSK	ASEA-ATOM	Sandvik	13	2.2	11.78	0.85	∿.02	383/A1	183	NA
Zircaloy-2	Annealed	OSK	ASEA-ATOM	Sandvik	14	2.3	12.24	0.80	∿.02	290/D4	183	NA
Zircaloy-2	Annealed	OSK	ASEA-ATOM	Sandvik	10.6	1.8	12.24	0.80	∿.02	414/A4	183	NA
Zircaloy-2	Annealed	OSK	ASEA-ATOM	Sandvik	14	2.2	11.78	0.85	∿.02	185/A7	183	NA
Zircaloy-2	Annealed	OSK	ASEA-ATOM	Sandvik	14	2.2	12.24	0.80	∿.02	185/C1	183	NA
Zircaloy-2	Annealed	QC	GE	GE	8.5-11	1.3-1.6	14.30	0.94	< .01	G-1	190D	NA
Zircaloy-4	CW-SR	HBR	Westinghouse	Westinghouse	27-30	5-6	10.70	0.61	.09-.38	F-9	155B	0.2
Zircaloy-4	CW-SR	HBR	Westinghouse	Westinghouse	27-30	5-6	10.70	0.61	.09-.38	G-6	155C	0.2
Zircaloy-2	CW-SR	BRP	Exxon	Sandvik	24	4	14.28	1.29	∿.03	DB30 0005	165W	2.1
Zircaloy-2	CW-SR	BRP	Exxon	Sandvik	8	0.6-1.0	11.38	0.86	< .01	JJ40 0002	165F	17.8
Zircaloy-2	CW-SR	BRP	Exxon	Sandvik	7	0.6-1.0	11.38	0.86	< .01	JK40 0001	165E	0.4
Zircaloy-2	CW-SR	BRP	Exxon	Sandvik	0.7	0.1	14.26	1.14	< .01	XA30 303	165A	0.3

Table 2-1 (Cont'd.)

SUMMARY OF IRRADIATED ZIRCALOY CLADDING MATERIALS

Material	Condition	Reactor	Rod Vendor	Tube Fabricator	Fuel Burnup (MWd/kg U)	Fluence x 10^{21} n/cm^2 >0.1 MeV	Nominal Dimensions (mm) OD	Wall	Ovality	Rod No.	ANL No.	Gas Release %
Zircaloy-2	CW-SR	BRP	Exxon	Sandvik	17.3	2.6	14.22	1.04	.01	DK50 014	165U	0.4
Zircaloy-2	CW-SR	BRP	Exxon	Sandvik	22.9	3.4	14.27	1.30	.02	DJ50 004	165V	15.0
Zircaloy-2	CW-SR	BRP	Exxon	Sandvik	22.9	3.4	14.22	1.29	.02	DJ50 001	165T	16.6
Zircaloy-2	CW-SR	BRP	Exxon	Sandvik	22.4	3.3	14.27	1.30	.01	DJ50 0007	165AG	18.6

Table 2-2

RESULTS OF PRETEST CLADDING CHARACTERIZATION MEASUREMENTS

Source	Oxide Thickness (μm) and Distribution		Hydride Distribution and Amount	ANL No.
	Inner Surface	Outer Surface		
H. B. Robinson	0.5-7	20-30 (uniform)	Circumferential (medium)	155B
Quad Cities	0.5-6 (nonuniform)	1-40 (nodular)	Random (low)	190D
Big Rock Point (medium burnup)	3-4 (uniform)	2-5 (uniform)	Random (low)	165E
Big Rock Point (high burnup)	0.5-18 (nonuniform)	50-70 (uniform)	Random (low)	165W

interactions in the form of circular growths that were ~150 μm in diameter and ~18 μm thick. The surface of the deposits was composed of large nodular or wormlike growths. Back-scattered electron images of the deposits indicated that they had a high uranium concentration. Both BRP rods (165E and 165W) had exhibited low fission-gas release.

LATER CHARACTERIZATIONS

The samples examined previously were all from low-gas-release rods. Because of the potential influence of fission products on the SCC susceptibility, the later characterizations of the various cladding concentrated on the differences between high- and low-gas-release rods. Samples from three additional rods from the BRP reactor were examined in detail. These were rods JJ400002 (165F), DK50014 (165U), and DJ500007 (165AG). The 165F rod had the same burnup as the previously examined 165E rod, but an appreciably higher gas release (14.3% vs 0.2%). The 165U and 165AG rods had comparable burnups (17.3 and 22.4 MWd/kg U, respectively) but significantly different gas releases (0.4 and 18.6%, respectively). The cladding from rod 165E (low gas release) exhibited a uniformly thick inner-surface oxide around the circumference, as shown in Fig. 2-1a. A high-quality inner-surface oxide layer is uniform in thickness, and is continuous and without breaches. In contrast, sections of the inner-surface oxide in specimens from rod 165F (high gas release) appeared to have been degraded by fission-product deposits, as shown in Fig. 2-1b. It is believed that the degradation of the oxide layer is related to the greater amount of fission-product deposition associated with high fission-gas release.

The cladding from rod 165U (low gas release) exhibited relatively clean areas as well as areas covered by particles composed of uranium and zirconium, as shown in Fig. 2-2. Wormlike growths were observed in isolated areas. In contrast, cladding from rod 165AG (high gas release) exhibited a wide range of deposit formations and compositions. Typical features of the surface are shown in Fig. 2-3. Figure 2-3a shows beads at the edge of a smooth film that covers much of the surface. This film is composed primarily of uranium, with small amounts of zirconium, cesium, and possibly tellurium. Figure 2-3b shows the wormlike growths that are observed in most irradiated samples. Several types of deposits containing iodine were also observed on the inner surface, as shown in Fig. 2-4. The deposit shapes are elongated (Fig. 2-4a), spherical (Fig. 2-4b), needlelike (Fig. 2-4c), and rodlike (Fig. 2-4d). The elemental composition of these deposits is primarily cesium and iodine with smaller amounts of zirconium and uranium.

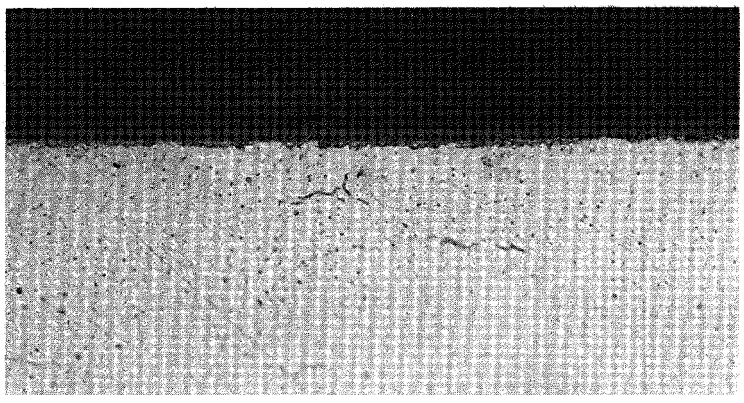

(a)

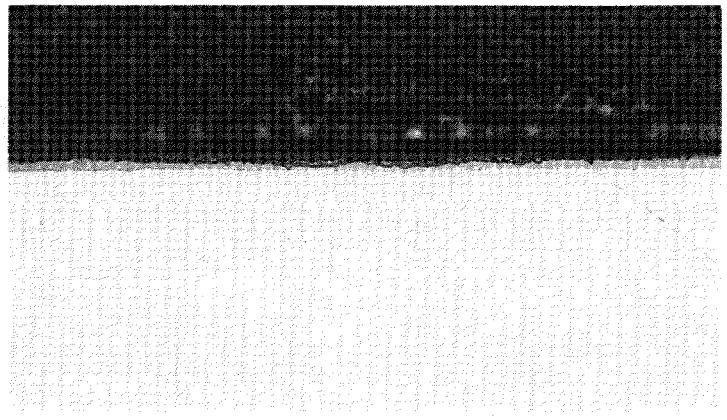

(b)

Fig. 2-1. Inner-surface oxide on high burnup BRP cladding: (a) ID oxide on low-fission-gas-release rod 165E, (b) ID oxide on high-fission-gas-release rod 165F.

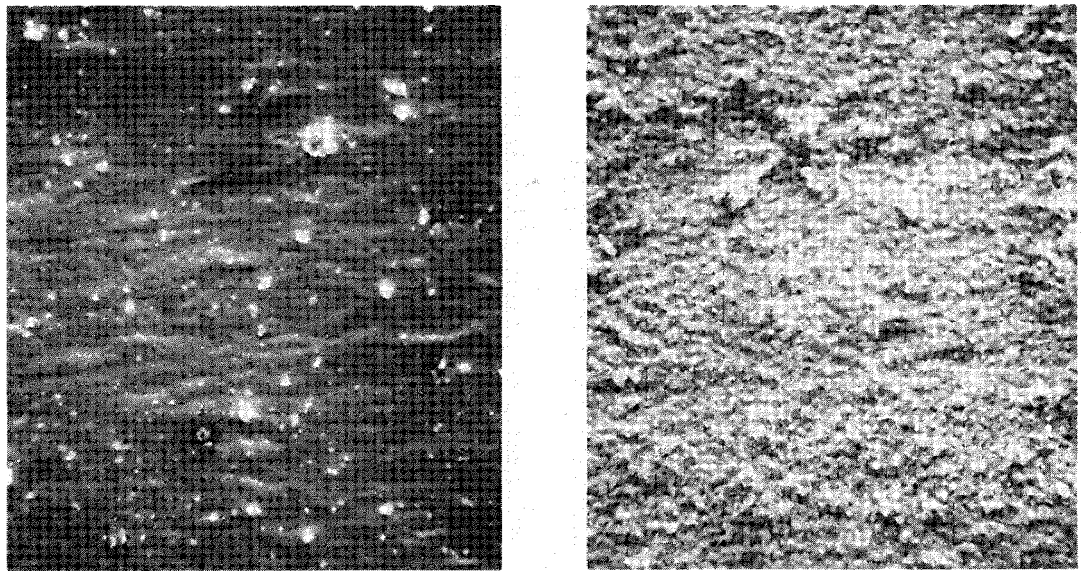

(a) (b)

Fig. 2-2. Typical surface appearance of BRP cladding from low-gas-release rod 165U.

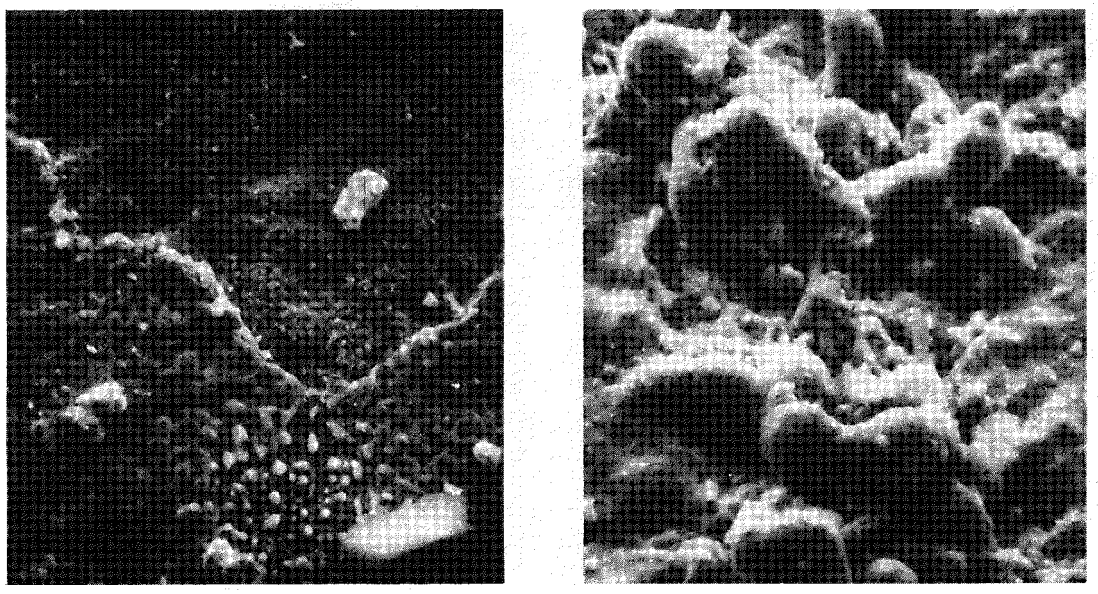

(a) (b)

Fig. 2-3. Inner-surface appearance of BRP cladding from high-gas-release rod 165AG.

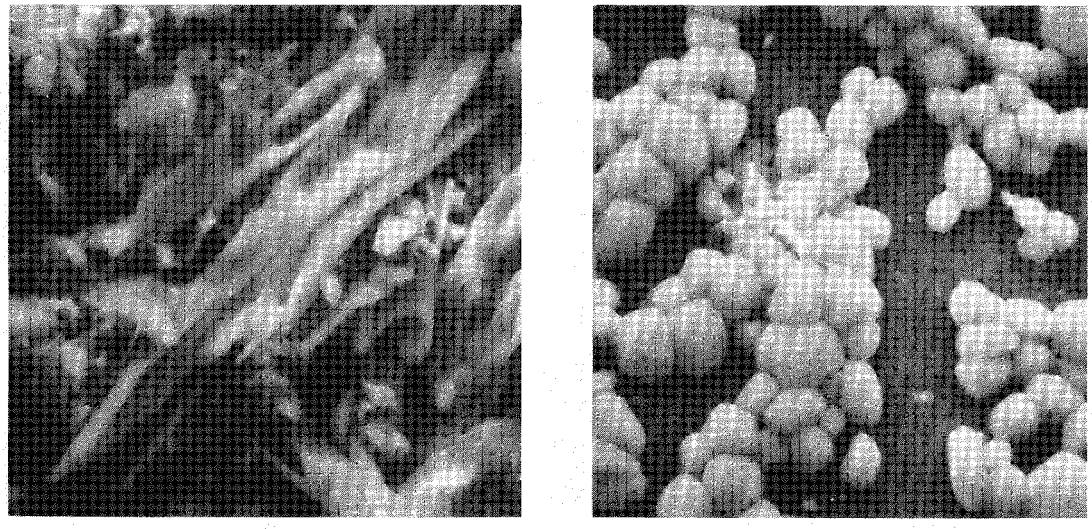

(a) (b)

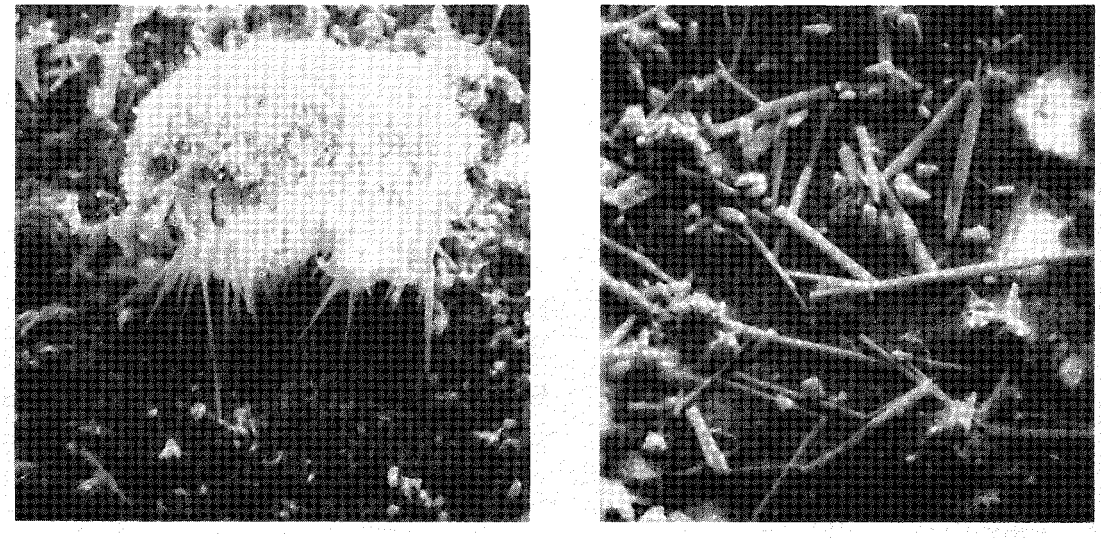

(c) (d)

Fig. 2-4. Iodine-cesium deposits observed on inner-surface of BRP cladding from high-gas-release rod 165AG. (a) elongated, (b) spherical, (c) needle-like, and (d) rod-like.

Two significant conclusions are drawn from these observations. First, the amount of volatile fission products deposited on the cladding inner-surface is directly related to the amount of fission gas released. This fission-product deposition is related to gas release but not to burnup. Thus, low-burnup, high-fission-gas-release fuel rods will exhibit larger amounts of fission-product deposits than high-burnup, low-fission-gas-release fuel rods. Second, extensive fission-product deposition can result in the degradation of a high-quality zirconium oxide layer on the cladding surface. The effect of this high-quality ZrO_2 layer and also its degradation by fission-product deposits on the susceptibility of the cladding to iodine SCC will be shown in a later section.

Blank

Section 3

TEST OPERATIONS

SPECIMEN PREPARATION

The preparation of specimens used in the iodine-induced SCC tests, the iodine-containing cumulative damage tests, and the iodine-free uniaxial tensile tests reported here was essentially the same as the specimen preparation described for SCC tests in the interm report (6). A brief review of the specimen-preparation procedures for HBR, QC, and BRP specimens is included here to promote continuity of text material.

The 15-cm-long BRP cladding specimens were cut from fuel-rod sections with fuel intact, as previously reported for HBR and QC cladding specimens. Fuel-rod sectioning was performed dry with a high-speed cut-off wheel (SiC), in the nitrogen atmosphere (<50 ppm of oxygen and moisture) of the Alpha Gamma Hot Cell Facility (AGHCF). An eddy-current inspection was not performed on BRP fuel rods before sectioning as previously done for HBR cladding because of the uncertainty in the interpretation of eddy-current results in the presence of fission-product deposits on the inner surface of the cladding. While the tightly packed fuel in specimens of HBR cladding had to be forcefully removed, the loosely packed fuel in the lower-burnup BRP rods was easily removed by light tapping of inverted specimens. The ends of as-cut specimens were deburred to ensure smooth specimen assembly by remote means. Profilometry measurements were made on individual specimen lengths at 45° angular increments to determine specimen ovality and inner- and outer-surface roughness. To minimize the adverse effects of surface roughness on the specimen-sealing operation, the outer-surface oxide and "crud" layer were polished with a fine emery cloth, and the specimen outer diameter was remeasured with a hand-operated micrometer. Specimen inner-diameter measurements were made with an "Intermik" inside micrometer after cleaning the inner surface with a nylon tube brush. In general, the inner- and outer-surface measurements of as-cleaned HBR and BRP cladding used in tests reported here varied $\leq \pm 1\%$ for specimens cut from a common fuel rod. The low ovality (≤ 0.02 mm) found in HBR and BRP cladding used in the present tests made the special handling techniques (annealing and rounding of specimen ends) developed

for previously reported high-ovality (≥0.08 mm) HBR cladding (6) unnecessary. The outer and inner measurements were used to establish the dimensional tolerances for the machined components of the mechanical seal, to determine the wall thickness of the cladding, and in hoop stress calculations. The cladding wall thickness was taken as (OD - ID)/2.

APPLICATION OF SCC PRESSURE SEALS

Cladding specimens used in the iodine SCC tests and cumulative-damage tests were mechanically sealed with modified "Swagelok" fittings as previously described elsewhere (6,7). Components of the mechanical pressure seal are shown in Fig. 3-1, a schematic representation of a mechanically sealed test specimen. These components include the tolerance-fitted, top and bottom zirconium end plugs and the tolerance-modified "Swagelok" fittings. Solid Vycor-glass rods were used to displace 98% of the specimen internal volume, and thereby limit the total system volume to 85 cm^3. A nominal 25 mg of elemental iodine crystals were added to the specimen in a small Vycor ampule as illustrated in Fig. 3-1. This ampule was broken during the specimen-sealing operation.

Profilometer data indicated some variation in the surface roughness of BRP cladding obtained from low-, medium-, and high-burnup fuel rods. Where the surface roughness of high-burnup BRP cladding was >0.015 mm (∿0.006 in.), slight changes were made in the dimensional tolerances of the mechanical seal components to ensure the pressure integrity of the seal. The torque rate applied by the motor-driven variable-speed torque wrench (6,7) in sealing BRP cladding specimens was varied depending on the cladding fluence. A faster torque rate and a higher level of torque were applied in the sealing of cladding from low-burnup BRP fuel rods; a slower torque rate and a slightly lower level of final torque was applied to cladding from high-burnup BRP fuel rods. On the average, each mechanical pressure seal was completed within 15-20 min, depending upon surface roughness and cladding fluence, with a seal reliability ≥95% on the initial application.

APPLICATION OF UNIAXIAL TENSILE GRIPS

The tensile grips for tubular cladding specimens were based on a variation of the "Swagelok" design used in the mechanical pressure seal. These grips were applied remotely to each end of the cladding tensile specimen, and the gripping action was actuated with the same in-cell equipment used to tighten the mechanical pressure seals for the SCC tests. Since the gripping action is applied to both the outer

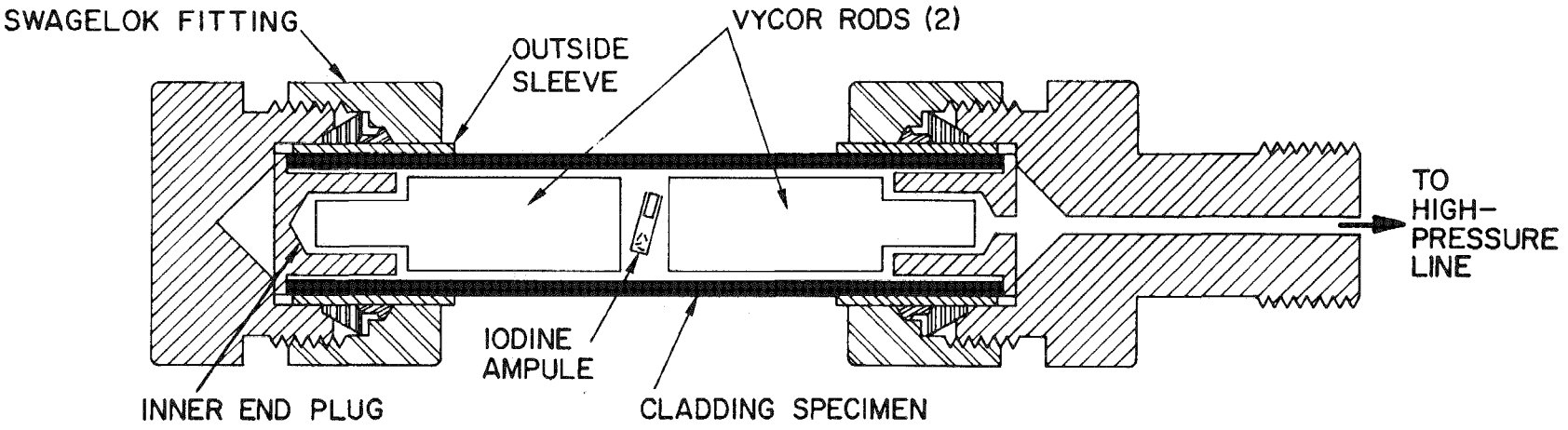

Fig. 3-1. Cutaway schematic drawing of specimen-sealing method and location of internal specimen components.

and inner surfaces of the specimen, the tensile grips were expected to support a maximum axial tensile load of ∿3200 g (∿7000 lb), without slippage, at temperatures up to ∿673 K (400°C). The grip was designed to test 14.3-mm (0.564-in.)-OD by 12.4-mm (0.490-in.)-ID irradiated Zircaloy-2 cladding with an estimated yield and ultimate stress of 641 and 689 MPa (∿93 and ∿100 ksi), respectively, at 325°C (8). A single proof tensile test was successfully conducted on a specimen of unirradiated BRP cladding at about 25°C.

TEST PROCEDURE

General

The SCC tests and the cumulative-damage tests on irradiated HBR, QC, and BRP cladding reported here were performed in-cell using the Mark-I Biaxial Creep Apparatus, a gas-pressurization system using helium. The system was described in detail in the interim report (6). In each SCC and cumulative-damage test the specimen was tested in a flanged stainless steel chamber, which served the dual role of an environmental enclosure and containment for material fragments produced in rare instances of violent specimen rupture. Specimen protection against the nitrogen hot-cell atmosphere was provided by a helium cover gas flowing at ∿400 cm^3/min. After initial specimen pressurization from a 1-liter vessel in the Mark I system, all tests were conducted under "short" volume conditions, in which the sum of the specimen and equipment volumes was limited to ∿85 cm^3. Specimen pressurization was completed within 30 s. Before each test, the stainless steel chamber was cleansed of residual iodine by heating to 450°C for 1 h while purging with flowing helium. Likewise, the internal specimen volume was purged with helium to minimize the concentrations of nitrogen, oxygen, and water vapor which could affect the test results. Specimen purging consisted of six or more successive cycles of specimen pressurization and depressurization within the pressure range ∿7 and 3 MPa. Iodine loss from the specimen was discounted on the basis of its very low vapor pressure ($Vp < 10^{-4}$ atm) (9), and the extremely low vapor pressure of cesium or zirconium iodide ($Vp \sim 10^{-14}$ atm) (10) that might form within the specimen at the 27°C ambient cell temperature. The effectiveness of the specimen purging operation in reducing gaseous impurities is supported by the results of Garzarolli et al. (11) who found that the threshold iodine pressure required to cause SCC cracking in Zircaloy cladding at constant specimen pressure (stress) increased as the oxygen and water-vapor content of the inert pressurizing gas increased. Iodine-induced SCC crack formation was obtained consistently in all the present tests on irradiated Zircaloy cladding as a result of the initial 25 mg of iodine added. During each test, specimen temperature and pressure were controlled within ±2°C and ±2%, respectively, and both were monitored continuously and recorded.

Iodine SCC Tests

Figure 3-2 is a schematic representation of the pressurization sequences used in SCC tests and cumulative-damage tests. The minimum (threshold)-stress portion of the complete SCC curve shown in Fig. 3-2d was determined by the threshold-stress tests illustrated in Fig. 3-2a. Each pressure (stress) step was held constant for 24 h, then increased to a higher stress in the absence of specimen failure during the previous holding period. The magnitude of individual stress increments was largely a matter of judgment based on initial tests on previously untested cladding, and was influenced by such factors as cladding type (Zircaloy-2 or -4), cladding fluence as indicated by fuel burnup, and experience gained from previous tests on similar cladding. The high-stress portion of the SCC curve was determined by the high-stress tests illustrated in Fig. 3-2b.

Cumulative-Damage Tests

Cumulative-damage tests were conducted at 598 K (325°C) on medium-burnup QC and high-burnup BRP cladding using the stress-increment and stress-decrement techniques illustrated in Fig. 3-2c. The specimen stress (pressure) was held constant at the initial stress, σ_1, for about half the time determined for failure at σ_1 in SCC tests ($t_1 = 1/2t_f$ at σ_1), then changed abruptly to a stress σ_2, and held constant to failure. The value of σ_2 was greater than σ_1 for stress-increment tests and less than σ_1 for stress-decrement tests. All cumulative-damage tests were conducted with 25 mg of iodine, in the same equipment, and under comparable test conditions, as used in the constant-stress SCC tests. The initial holding time, t_1, at each value of the initial stress, σ_1, was estimated from the appropriate SCC curve for the cladding being tested.

In stress-increment cumulative-damage tests, the 1-liter vessel was used during the initial pressurization and again when the stress was incremented from σ_1 to σ_2 ($+\Delta\sigma$). About 30 s after the initiation of each pressure step the 1-liter vessel was isolated from the pressurizing system, and the test was conducted under "short-volume" conditions as in the case of SCC tests.

In stress-decremented cumulative-damage tests, the 1-liter vessel was used in the initial specimen pressurization only. The subsequent stress decrement ($-\Delta\sigma$) was accomplished with a variable-volume, dead-end cavity. In cumulative-damage stress-decrement tests ($-\Delta\sigma$), the cavity was isolated from the pressurization system at "zero" gage system pressure. The stress (pressure) decrement was achieved by

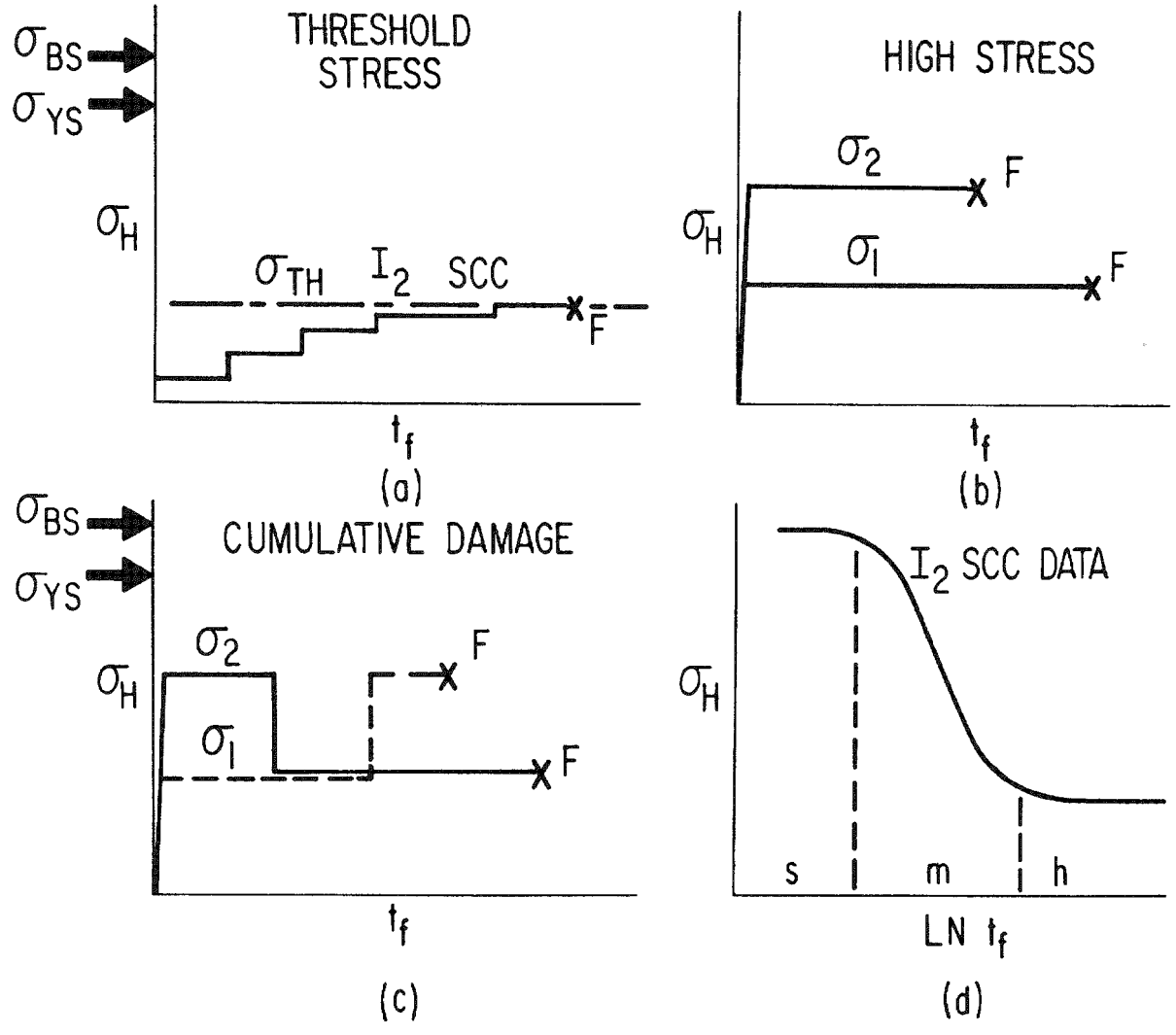

Fig. 3-2. Schematic representations of pressurizing sequences used in SCC tests and the resultant data plot: (a) pressure-step tests to determine σ_{th}. (b) tests to determine steep portion of I_2 SCC curve. (c) tests to determine damage accumulated in upward and downward power ramps, (d) complete I_2 SCC curve.

suddenly opening a hand-operated isolation valve. System pressure equalization at the lower pressure P_2 was accomplished in about 6 s. Iodine concentration within the specimen is unaffected by the addition of the cavity volume to the initial system volume, because the total moles of both helium and iodine remain the same. The isolation valve was then closed and the cumulative-damage test continued to failure at the lower stress (pressure), P_2, under "short-volume" conditions. Specimen pressure control was immediately assumed by the electronic system.

The step-wise stress (pressure) decrements and increments shown in Fig. 3-2c are idealized representations of experimental goals. These stress decrements and increments could not be achieved experimentally, but they could be closely approximated. Figure 3-3a is a schematic representation of an experimentally achieved stress (pressure) decrement. On initial pressurization from the 1-liter volume, pressure equalization occurs in about 30 s, as was the case for SCC tests. When the stress decrement is initiated, the specimen pressure falls over a 1-s period to a minimum value about 20% below the desired pressure (P_2), then equilibrates at the desired value P_2 in 6 s. The shape of the pressure-decrement curve is influenced by the physical characteristics of the system and by the cooling effect of an expanding gas from P_1 to P_2 ($P_2 < P_1$). The system characteristics include the frictional resistance to gas flow through a small-bore tube, the low system volume, and the flow restrictions of the in-line orifice.

Figure 3-3b is a schematic representation of an experimentally achieved stress (pressure) increment. Both sections of this curve are approximately identical and also represent pressurizing conditions achieved for SCC tests.

Uniaxial Tensile Tests

Four uniaxial tensile tests were conducted in the program. Two tensile tests were conducted on medium-burnup QC cladding, and two were conducted on low-burnup ($\sim$1 MWd/kg U) BRP cladding. The four tensile specimens, obtained from the fuel rods by the same procedures used for the SCC specimens, were ultrasonically cleaned in acetone to remove loose activity from the outer surface and fuel particles from the inner surface, rinsed in alcohol, and gas (nitrogen)-dried. After cleaning, the gamma activity of the low-burnup BRP cladding was $\sim$100 mr/hr while the gamma activity of QC cladding was $\sim$1 R/hr. The residual gamma activity of all four specimens was sufficiently low to permit the transfer of individual specimens to a low-level beta-gamma hot-cell facility for tensile testing. The tensile grips were

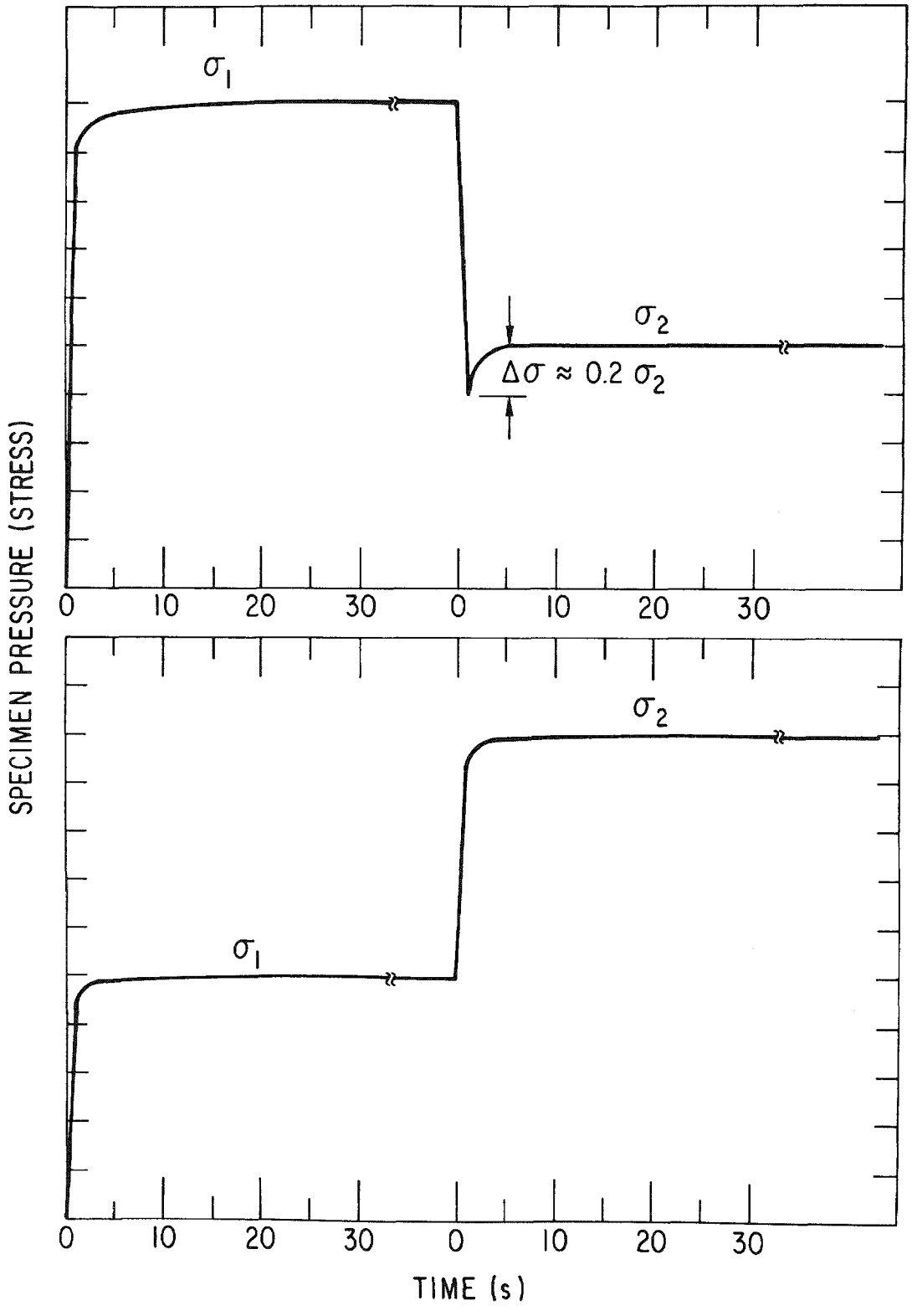

Fig. 3-3. Schematic representation of experimentally achieved stress (pressure) decrements and increments in cumulative-damage tests. (a) top-stress decrement. (b) bottom-stress increment.

attached to each specimen by remote means in the air atmosphere of the clean area of the high-level, hot-cell facility, and transferred to the low-level hot cell with pull bars in place. The tensile tests were performed in a floor-model Instron tensile machine with a 5000-kg (∿11,000-lb) load-cell capacity. The load-strain record for each tensile test was obtained with a SATEC, Model PSH 8MS high-temperature extensometer, and the load-strain curve was recorded on the Instron X-Y plotter. Axial strain was measured over a 5.08-cm-long specimen gage length. The specimen and tensile grips were heated in a three-zone, split-tube, resistance furnace, with power and temperature control provided for each zone. Specimen temperature was monitored with three Chromel-Alumel thermocouples located at the center and at each end of the 5.08-cm-long gage section. The thermocouples were held in contact with the specimen surface by spring clips. During the tensile test, specimen temperature was controlled within ± 7°C and recorded on a strip chart. The tensile tests were conducted to axial strains considerably beyond the yield stress, but below the ultimate stress, to prevent cladding rupture. This precaution was taken to avoid possible contamination of the low-level hot-cell facility by particulate activity that might be released from the inside of the ruptured specimen.

Blank

Section 4

TEST RESULTS

SCC TESTS

The nominal hoop stress for all SCC tests was calculated by the standard expression used for a pressurized thin-wall cylinder (12):

$$\sigma_{nom} = \frac{(r_o^2 + r_i^2)}{(r_o^2 - r_i^2)} P, \qquad (4\text{-}1)$$

where r_o and r_i are the external and internal radii, respectively, of the cylinder and P is the internal pressure. Diametral strain at failure was determined from posttest micrometer measurements of the outer specimen diameter taken at axial locations on either side of the failure site, but not less than one specimen diameter away from the failure. The diametral strain (e_f) was calculated with the expression

$$e_f = \frac{D_o - D_f}{D_o} \qquad (4\text{-}2)$$

where D_f is the nominal posttest specimen diameter and D_o is the outer specimen diameter before testing.

The iodine-induced SCC failure strain observed in irradiated Zircaloy cladding covered a wide range from about 0.5 to 1% for HBR cladding tested at 633 K (360°C) to $\leq$0.01% for QC cladding and BRP cladding tested at 598 K (325°C). An important point to note is not the relative magnitude of the failure strain, but the fact that it was always very low, and within the strain range normally associated with brittle failure. An additional point to be emphasized is that most of the SCC failures occurred or initiated near the center of the gage length, the region of minimum end effects. In the following tables listing the results of SCC tests, the axial location of the failure site is given in terms of the specimen diameter. The letter M indicates a failure site at the middle of the gage length; 2TE indicates a failure site located two specimen diameters from the top end of the specimen.

Therefore, in a 12.7-mm (0.5-in.)-diameter specimen the 2TE designation locates the failure site about 25.4 mm (1.0 in.) below the Swagelok closure at the top of the specimen.

Irradiated H. B. Robinson Cladding (Stress-relieved Zircaloy 4)

Two SCC tests were conducted on high-burnup HBR cladding at 633 K (360°C) to complete the partial SCC curve reported previously (6). These specimens, 155BC7 and 155BC8, were SCC tested at nominal hoop stresses of 273 and 413 MPa (39.6 and 60 ksi), respectively. The completed SCC curve at 633 K is shown in Fig. 4-1, and the data are tabulated in Table 4-1. Specimen 155BC7, tested at the lower stress, failed by a pinhole breach; specimen 155BC8 tested at the higher stress failed by rupture. Three additional SCC tests (155BC9, 155BC5, and 155BC6) were conducted on HBR cladding at 598 K (325°C) to determine the temperature effect on SCC failure time for high-burnup Zircaloy cladding. In these latter three tests, specimens 155BC6 and 155BC9 were tested at a nominal hoop stress of 275 MPa (40 ksi), while specimen 155BC5 was tested at a nominal hoop stress of 414 MPa (60 ksi). The results do indicate a temperature effect on SCC failure time in the temperature range 598-633 K (325-360°C). The curves in Fig. 4-1 suggest a "threshold" (minimum) stress for iodine-induced SCC failure within 24 h for irradiated HBR cladding that is <200 MPa (29 ksi) at 633 K (360°C) and <275 MPa (40 ksi) at 598 K (325°C). The open squares with arrows shown in Fig. 4-1 represent SCC tests that were terminated without specimen failure at the indicated stress levels and test times. Finally, specimen 155BC9 tested at 598 K (325°C) and a hoop stress of 275 MPa (40 ksi) failed in 1.1×10^2 s (0.03 h) by a pinhole breach through the cladding wall. The observed time to failure is about 1/500th of the time to failure determined for the duplicate specimen 155BC6 (1.1×10^2 s vs. 5.5×10^4 s) tested at the same temperature and nominal hoop stress. This difference in SCC behavior might be explained by the fact that specimen 155BC9 was tested at 598 K and 275-MPa stress for 1.8×10^5 s (50.6 h) without the addition of iodine. This was done to determine whether any trace of residual iodine (or iodine compound) remaining on the inner surface after fuel removal could be effective in initiating SCC failure. If it is assumed that the time required for crack initiation and growth to a critical length is very large compared to the time required to propagate a crack of critical length to SCC failure, then it would follow that the crack ultimately responsible for the failure had grown to near critical length during the initial 50.6-h test period. Such a crack could have originated as an existing crack in the irradiated cladding or could have been initiated at the site of trace quantities

Table 4-1

RESULTS OF BIAXIAL IODINE SCC TESTS ON IRRADIATED HBR CLADDING AT 325 AND 360°C

Specimen Number	Preflaw Depth (μm)	Iodine Amount (mg)	Iodine Conc. (mg/cm²)	Test Temp. (°C)	Pressure Steps	Hoop Stress,[a] MPa (ksi)	Stress Intensity Factor (MPa·m^½)	Time (h)	Total Time (h)	Failure Mode[b]	Failure Strain (%)[f]	Failure Location[c]	Remarks
155BD-1	200	250	7.9	360	1	115 (16.88)	2.4	24					
					2	140 (20.30)	2.9	24					Developed leaks at both end seals after 5.2 h. Cut and resealed twice.
					3	160 (23.21)	3.3	5.2					
					4	380 (55.11)	7.9	0.53[d]	53.73	P[e]	0.68	M	
155CA-1	80	250	7.9	360	1	220 (31.91)	3.7	0.53					
					2	220 (31.91)	3.7	2.0					Iodine SCC failures in area of SS end plugs.
					3	220 (31.91)	3.7	0.5[d]	3.0	P		TE,BE	
155CA-3	30	250	7.9	360	1	205 (29.73)	2.2	0.5[d]	0.5	C	0.26	1 TE,1 BE	Iodine SCC failures in area of SS end plugs.
155BD-3	60	250	7.9	360	1	215 (31.18)	3.1	24					
					2	225 (32.63)	3.3	10.5[d]	34.5	C	0.25	M	SCC failure away from preflaw.
155BD-5	0	250	7.9	360	1	200 (29.01)	-	14.3[d]	14.3	P	1.1	M	--
155BD-4	0	0	-	360	1	200 (29.01)	-	7.4[d]	7.4	R	0.4	M	Tested with fuel in specimen.
155BB-3	0	0	-	360	1	221 (32.1)	-	41.3					
					2	278 (40.3)		4.0					
					3	376 (53.2)		4.2					
					4	441 (63.9)		22.6					
					5	485 (70.4)		3.0[d]	75.2	R	0.8	BE	Tested with fuel in specimen.
155BC-7	0	25	0.79	360	1	273 (39.61)	-	0.61[d]	0.61	P	0.1	2BE	
155BC-8	0	25	0.79	360	1	413 (59.96)	-	0.18[d]	0.18	R	ND	M	
155BC-9	0	25	0.79	325	1	275 (39.95)	-	0.03[d]	0.03	P	<0.01	2TE	Tested 50.6 h at 275 MPa without iodine.

Table 4-1 (Cont'd.)

RESULTS OF BIAXIAL IODINE SCC TESTS ON IRRADIATED HBR CLADDING AT 325 AND 360°C

Specimen Number	Preflaw Depth (μm)	Iodine Amount (mg)	Iodine Conc. (mg/cm²)	Test Temp. (°C)	Pressure Steps	Hoop Stress,[a] MPa (ksi)	Stress Intensity Factor (MPa·m^½)	Time (h)	Total Time (h)	Failure Mode[b]	Failure Strain (%)	Failure Location[c]	Remarks
155BC-5	0	25	0.79	325	1	414 (60.03)	-	1.49[d]	1.49	P	∿0.19	2BE	--
155BC-6	0	25	0.79	325	1	276 (40.07)	-	15.3[d]	15.3	P	∿0.10	M	--

[a] Nominal hoop stress for unflawed specimens; net hoop stress for flawed specimens.

[b] P indicates pinhole; C indicates axial cracking; R indicates rupture.

[c] M indicates middle of specimen; numbers indicate distance from top end (TE) or botton end (BE), in tube ODs.

[d] Time when specimen failed.

[e] Failure occurred at site of preflaw.

[f] ND indicates not determined.

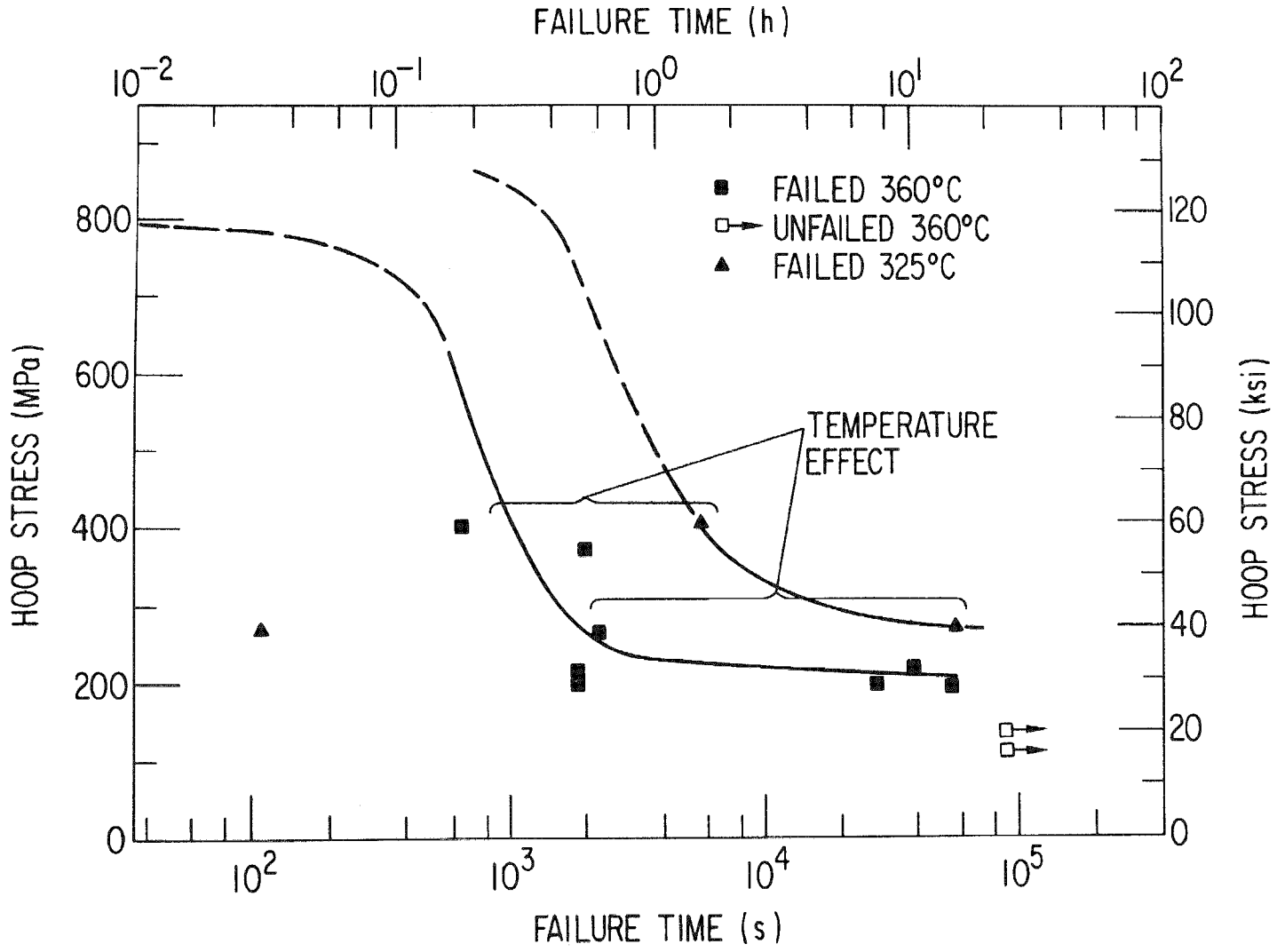

Fig. 4-1. Results of Iodine SCC Tests on Irradiated HBR Cladding at 598 and 633 K.

of iodine or iodine compounds. With the addition of iodine (25 mg), the crack growth rate to a critical crack length was increased, and the subsequent propagation of the critical length crack to failure was instantaneous.

High-burnup, Low-fission-gas-release, Big Rock Point Cladding (Stress-relieved Zircaloy-2)

The test results at 598 K (325°C) for high-burnup BRP cladding from low-fission-gas-release fuel rods (DB300005 - DK50014) are listed in Table 4-2. The cladding fluence is estimated to be 4 x 10^{21} n/cm^2 (E > 0.1 MeV) at a reported fuel burnup of 24 MWd/kg U. The (solid) SCC curve for this cladding is shown in Fig. 4-2. Figure 4-2 indicates that the "threshold" stress required to promote iodine-induced SCC failure within 24 h is about 165 MPa (24.0 ksi).

High-burnup, High-fission-gas-release, Big Rock Point Cladding (Stress-relieved Zircaloy-2

The cladding characterization studies showed a marked increase in fission-product deposition on the cladding of high (>10%)-fission-gas-release rods and the apparent degradation of the possibly protective nature of the inner oxide layer. Attempts to use cladding from high-gas-release rods to complete the high-burnup SCC curve gave results inconsistent with previous data. Therefore, to determine whether the greater fission-product deposition affects the SCC threshold stress, a series of tests was conducted with cladding from high-gas-release rods DJ50004, DJ50001, and DJ500007. Unfortunately, sufficient cladding was not available from one rod to cover the desired stress-time regime. Test results at 598 K (325°C) for these rods are listed in Table 4-3. The cladding fluence is estimated to be 4 x 10^{21} n/cm^2 (E > 0.1 MeV) at a reported fuel burnup of 23 MWd/kg U. The (dashed) SCC curve for this cladding is also shown in Fig. 4-2 and indicates that the "threshold" stress required to promote iodine-induced SCC failure within 24 h is about 139 MPa (20.1 ksi). Although the difference in the "threshold" stress of high-burnup BRP cladding from high- and low-fission-gas-release fuel rods is only ~12% (165 MPa vs. 139 MPa), this difference is real and not the result of experimental data scatter. This view is supported by the stress-increment data for specimen 165AG-12 given in Table 4-3. Between pressure steps 5-6 and 6-7, the hoop stress in specimen 165AG-12 was increased by increments of 5.6% and 5.3%, respectively, in an attempt to determine the "threshold" stress for failure in 24 h. These stress increments are about half as large as the 12% difference in the "threshold" stress for high- and low-fission-gas-release cladding shown in Fig. 4-2. Open symbols with arrows in Fig. 4-2 represent tests terminated without failure at the stresses and times indicated.

Table 4-2

RESULTS OF BIAXIAL IODINE SCC TESTS AT 325°C ON HIGH-BURNUP BRP CLADDING FROM LOW-FISSION-GAS-RELEASE RODS

Specimen Number	Iodine Amount (mg)	Iodine Conc. (mg/cm^2)	Pressure Step	Hoop Stress MPa	Hoop Stress (ksi)	Failure Time (h)	Failure Mode[a]	Failure Strain (%)[c]	Failure Location[b]
165W-8	25.5	0.61	1	180	(26.14)	4.0	P	~0.05	M
165W-10	25.2	0.60	1	172	(24.89)	6.8	P	~0.05	2 1/2 BE
165W-12	25.2	0.60	1	156	(22.65)	142.0	C	~0.05	M
165W-18	25.0	0.60	1	275	(39.93)	1.98	R	ND	M
165W-19	25.0	0.60	1	408	(59.14)	2.98	R	ND	M
165W-20	25.1	0.60	1	274	(39.82)	15.44	R	ND	1BE
165U-4	25.0	0.60	1	499	(72.33)	0.35	R	<0.01	1BE

[a] P indicates pinhole; C indicates crack; R indicates rupture.

[b] M indicates middle of specimen within 1/2 Tube OD; 2 1/2 BE indicates a distance of 2 1/2 Tube ODs from bottom end.

[c] ND indicates not determined.

Table 4-3

RESULTS OF BIAXIAL IODINE SCC TESTS AT 325°C ON HIGH-BURNUP BRP CLADDING FROM HIGH FISSION-GAS RELEASE RODS

Specimen Number	Fission-gas Release (%)	Iodine Amount (mg)	Iodine Conc. (mg/cm^3)	Pressure Step	Hoop Stress MPa	Hoop Stress (ksi)	Time (h)	Failure Strain (%)	Failure Mode (a)	Failure Location (b)
165V-10	15.0	25.0	0.63	1	414	(59.98)	0.84(c)	∿0.14	R	2 1/2 BE
165T18A	16.6	25.0	0.67	1	151	(21.91)	7.67(c)	∿0.05	P	1BE
165T18B	16.6	25.0	0.67	1	119	(17.22)	3.42(c)	∿0.05	P	4TE
165AG12	18.6	25.0	0.67	1	104	(15.05)	24.0			
				2	111	(16.12)	24.0			
				3	114	(16.56)	71.7			
				4	118	(17.10)	24.3			
				5	125	(18.08)	24.0			
				6	132	(19.10)	24.0			
				7	139	(20.12)	69.0(c)	∿0.04	P	2 1/2 BE
165AG19	17.1	25.0	0.67	1	221.3	(32.10)	2.95(c)	∿0.04	P	2 1/2 TE
165AG20	17.1	25.0	0.67	1	221.3	(32.10)	2.25(c)	∿0.04	P	2TE
165V5	13.5	25.0	0.63	1	273	(39.64)	1.18(c)	∿0.05	P	1/4 TE

(a) P indicates pinhole; C indicates crack; R indicates rupture.

(b) M indicates middle of specimen within 1/2 Tube OD; 4TE indicates a distance of 4 Tube ODs.

(c) indicates failure time.

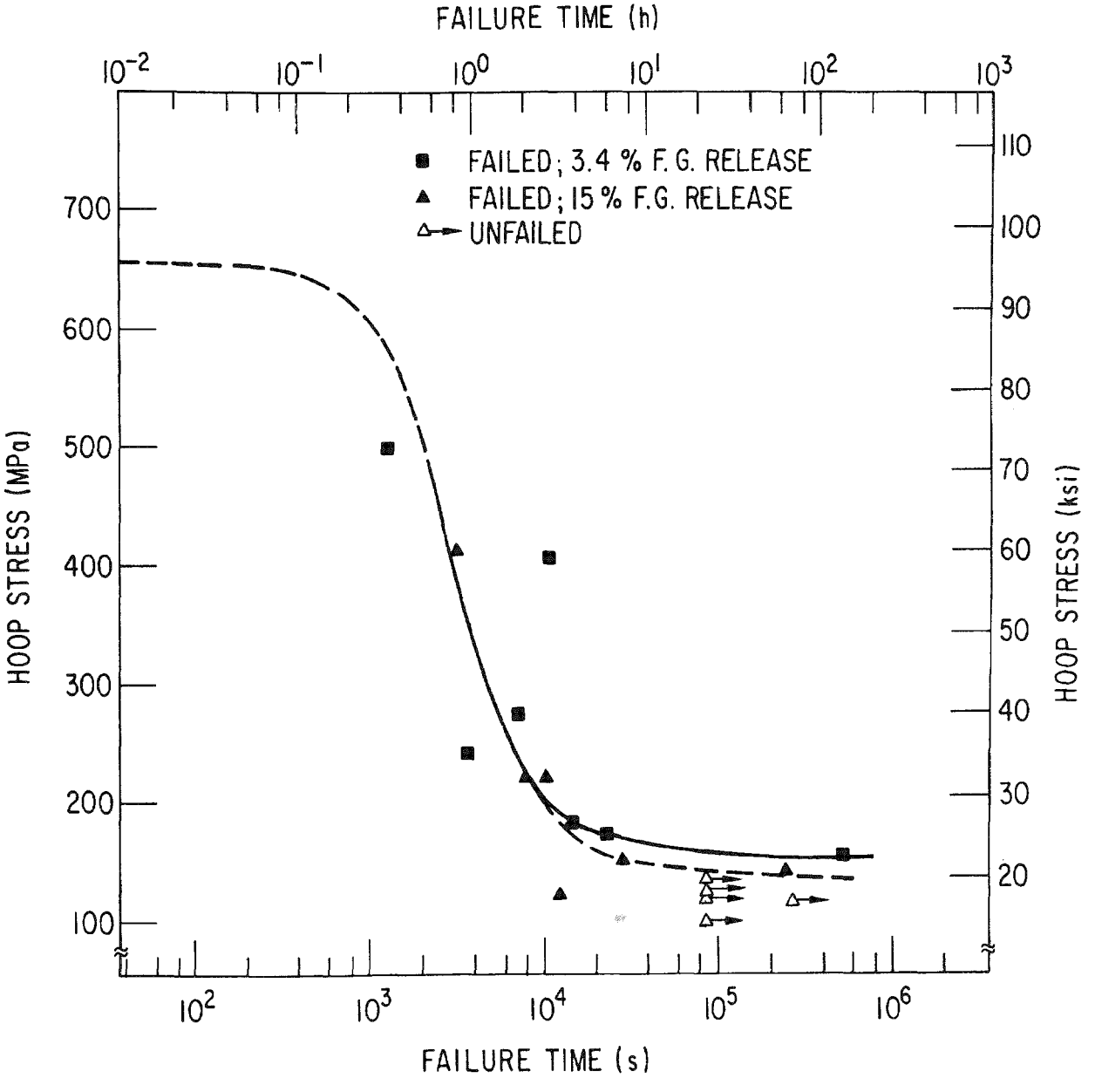

Fig. 4-2. Results of iodine SCC tests at 598 K on high-burnup BRP cladding from high- and low-fission-gas-release fuel rods.

Figure 4-2 also indicates that the SCC curves for high- and low-fission-gas-release cladding from high-burnup BRP fuel rods tend to merge into one SCC curve for hoop stresses above 221 MPa (32.1 ksi). The stress level at which a merger of the two SCC curves appears to occur is established by the SCC test results for duplicate specimens 165AG-19 and -20 given in Table 4-3. Both specimens were tested at a hoop stress of 221 MPa, and their corresponding failure times were 1.06×10^4 and 8.10×10^3 s (2.95 and 2.25 h).

Medium-burnup, Low-fission-gas-release, Big Rock Point Cladding (Stress-relieved Zircaloy-2)

Three tests on medium-burnup, low-gas-release BRP cladding were among the tests reported in the interim report, where they were referred to as "low-burnup" cladding. Because even lower-burnup BRP cladding was subsequently added to the program, these specimens are now referred to as "medium-burnup" cladding. The results of these tests at 598 K, together with the results of two additional tests conducted since the interim report, are given in Table 4-4 and plotted as the solid circles in Fig. 4-3. The specimens came from fuel rods JK400001, which had a burnup of ~7 MWd/kg U and a fluence between 0.6 and $1.x\ 10^{21}$ n/cm^2 ($E > 0.1$ MeV). The two additional tests, specimens 165E-10 and -11, were an attempt to extend the threshold-stress data, or low-stress regime, to longer times. However, the specimens failed in generally the same time as the earlier tests. These data and the open circles in Fig. 4-3 from unfailed tests support the conclusion that the probable threshold stress for this cladding is about 280 MPa (40.6 ksi) and that the cluster of data points for failed tests probably lies near the upward bend in the SCC curve. The high-stress portion of the curve, therefore, would be expected to lie near or to the left of the curve for high-burnup cladding, also shown in Fig. 4-3.

Medium-burnup, High-fission-gas-release Big Rock Point Cladding (Stress-relieved Zircaloy-2)

The finding of the fission-product release effect on the high-burnup BRP cladding prompted the limited testing of cladding from high-gas-release, medium-burnup rod JJ400002, to determine the threshold-stress value, the test results at 598 K (325°C) are listed in Table 4-5. The cladding fluence is estimated to be between 0.6 and 1.0×10^{21} n/cm^2 ($E > 0.1$ MeV) at a reported burnup of ~8 MWd/kg U. Fission-gas release was calculated to be about 17.8%. Data points for the four SCC tests conducted on this cladding (specimens 165F-7, -9, -10, and -11) are plotted as the solid squares in Fig. 4-3.

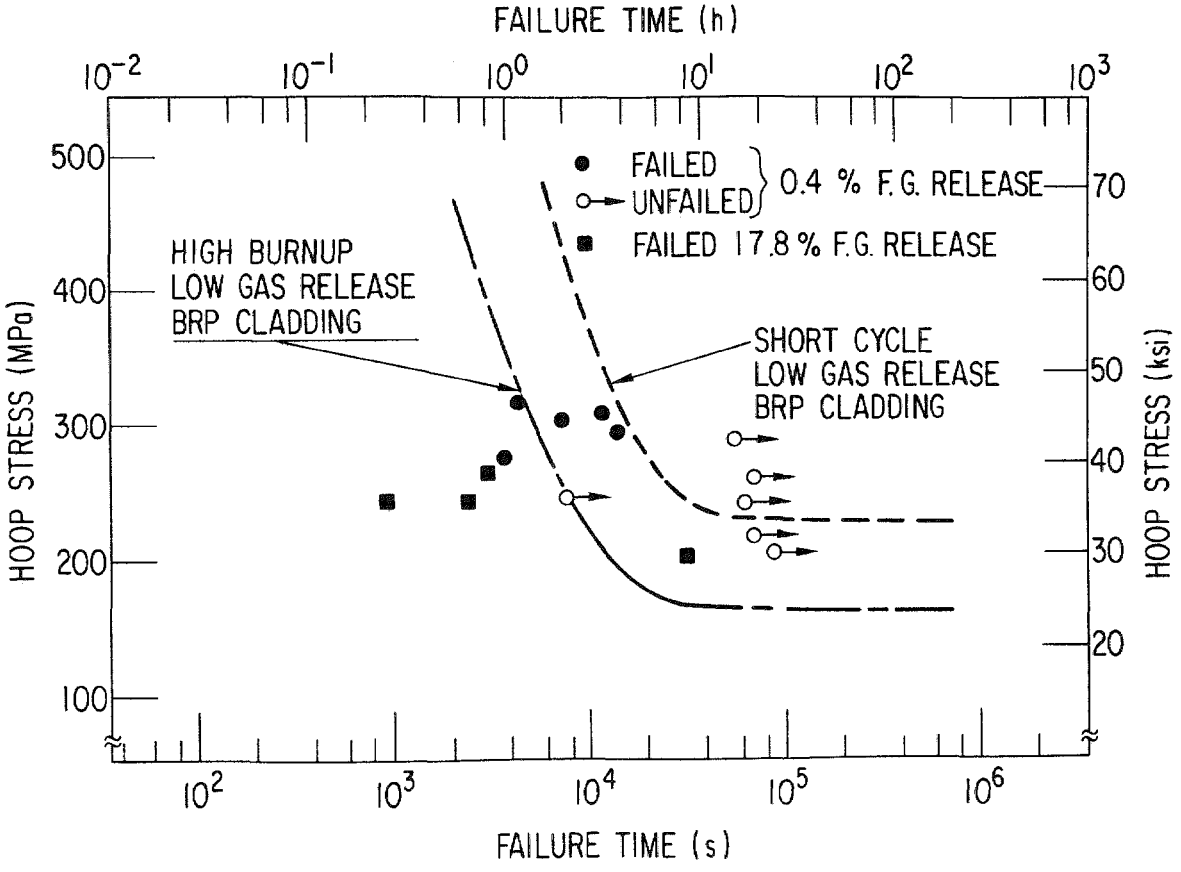

Fig. 4-3. Results of iodine SCC tests on medium-burnup BRP cladding at 598 K.

The four data points for this cladding indicate that the threshold stress is indeed lowered by the presence of extensive fission-product deposition on the cladding surface. The threshold stress appears to be in the vicinity of 200 MPa (29 ksi), compared with 280 MPa (40.6 ksi) for the low-gas-release cladding. This difference is significantly greater than what was found for low and high-gas-release high-burnup cladding, suggesting that the effect is either minimized at higher burnup or that different mechanisms are responsible for the effects. Note also that the high-stress regime of the curve would have shorter times to failure than the low-gas-release cladding.

The behavior of this cladding is believed to be related to the heavy cesium-bearing deposits found on the inner surface of the 165F series specimens. The 165F series specimens listed in Table 4-5 exhibited a gamma activity that was consistently a factor of ten greater than the gamma activity exhibited by the 165E series specimens listed in Table 4-4. Gamma scanning of specimen 165F-9 (Fig. 4-4) indicated that the activity was due primarily to Cs^{137} activity peaks with a period approximately that of a pellet length.

Low-burnup Big Rock Point Cladding (Stress-relieved Zircaloy-2)

Test results for low-burnup (short-cycle) BRP cladding (fuel rod XA30303) at 598 K (325°C) are listed in Table 4-6. The cladding fluence is estimated to be $\sim 0.1 \times 10^{21}$ n/cm^2 (E > 0.1 MeV) at a reported fuel burnup of 0.7 MWd/kg U. The SCC curve defined by the five data points given in Table 4-6 is plotted in Fig. 4-5. A reference SCC curve for high-burnup BRP cladding with an estimated fluence of 4×10^{21} n/cm^2 (E > 0.1 MeV) is also shown in Fig. 4-5 for comparison. The "threshold" stress for iodine-induced SCC failure in low-burnup BRP cladding is about 226 MPa ($\sim$32.7 ksi). This "threshold" stress is about 1.4 times as high as the comparable "threshold"-stress value of 165 MPa (24.0 ksi) determined for high-burnup BRP cladding shown in Fig. 4-2. Since the specimens for both the high- and low-burnup BRP cladding were obtained from low-fission-gas-release fuel-rods, the difference in the SCC curves shown in Fig. 4-5 is attributed to the effect of fluence on the SCC failure of irradiated Zircaloy cladding at 598 K (325°C).

CUMULATIVE-DAMAGE TESTS

Nine cumulative-damage tests were performed: two tests on QC cladding and seven on BRP cladding, all at 598 K (325°C). The results are given in Table 4-7. The holding time (t_1) at the initial stress (σ_1) was determined by the expression $t_1 = (1/2)t_f$ at σ_1, where t_f is the time to failure at σ_1 determined in an SCC test. The SCC curves for these cladding materials were used to obtain the value for t_f

Table 4-4

RESULTS OF BIAXIAL IODINE SCC TESTS AT 325°C ON MEDIUM-BURNUP BRP CLADDING FROM LOW-FISSION-GAS-RELEASE FUEL ROD

Specimen Number	Iodine Amount (mg)	Iodine Conc. (mg/cm^2)	Pressure Steps	Hoop Stress MPa	Hoop Stress (ksi)	Time (h)	Failure Mode[a]	Failure Strain (%)[b]	Failure Location[c]
165E-4	26.7	0.67	1	206	(29.90)	22.9			
			2	220	(31.80)	19.7			
			3	228	(33.04)	2.8			
			4	230	(33.33)	3.1			
			5	244	(35.39)	17.1			
			6	249	(36.09)	2.1			
			7	256	(37.21)	8.0			
			8	262	(38.07)	19.5			
			9	271	(39.36)	0.7			
			10	275	(39.85)	46.6			
			11	287	(41.66)	3.5			
			12	297	(43.02)	15.3			
			13	311	(45.10)	3.1[d]	P	0.19	2TE

Table 4-4 (Cont'd.)

RESULTS OF BIAXIAL IODINE SCC TESTS AT 325°C ON MEDIUM-BURNUP BRP CLADDING FROM LOW-FISSION-GAS-RELEASE FUEL ROD

Specimen Number	Iodine Amount (mg)	Iodine Conc. (mg/cm^2)	Pressure Steps	Hoop Stress MPa	Hoop Stress (ksi)	Time (h)	Failure Mode[a]	Failure Strain[b] (%)	Failure Location[c]
165E-7	25.6	0.64	1	310	(44.95)	2.0[d]	R	>1.2	M
165E-9	25.6	0.64	1	297	(43.02)	3.8[d]	R	>2.0	M
165E-10	25.0	0.64	1	320	(46.41)	1.21[d]	R	ND	M
165E-11	25.0	0.64	1	277	(40.18)	1.02[d]	R	ND	3BE

[a] P indicates pinhole; R indicates rupture.

[b] ND indicates Not Determined.

[c] M indicates middle of specimen with 1/2 tube OD; 2TE indicates distance of 2 tube ODs from top end of specimen.

[d] indicates failure time.

Table 4-5

RESULTS OF BIAXIAL IODINE SCC TESTS AT 325°C ON MEDIUM-BURNUP BRP CLADDING FROM HIGH-FISSION-GAS-RELEASE FUEL ROD

Specimen Number	Iodine Amount (mg)	Iodine Conc. (mg/cm^2)	Pressure Steps	Hoop Stress MPa	Hoop Stress (ksi)	Time (h)	Failure Mode[a]	Failure Strain (%)	Failure Location[b]
165F-9	25	0.64	1	247	(35.80)	0.67[c]	C	0.03	3TE
165F-11	25	0.64	1	248	(35.97)	0.25[c]	C	<0.01	1/2 BE
165F-7	25	0.64	1	266	(35.58)	0.85[c]	C	0.08	1BE
165F-10	0	0	1	245	(35.53)	90.2			
	0	0	2	258	(37.42)	95.0			
	0	0	3	274	(39.74)	70.1			
	25	0.64	4	180	(26.11)	25.0			
			5	192	(27.85)	23.0			
			6	205	(29.73)	8.6[c]	C	<0.01	1/4 TE

[a] C indicates axial crack.

[b] 3TE indicates distance of 3 tube ODs from top of specimen.

[c] indicates failure time.

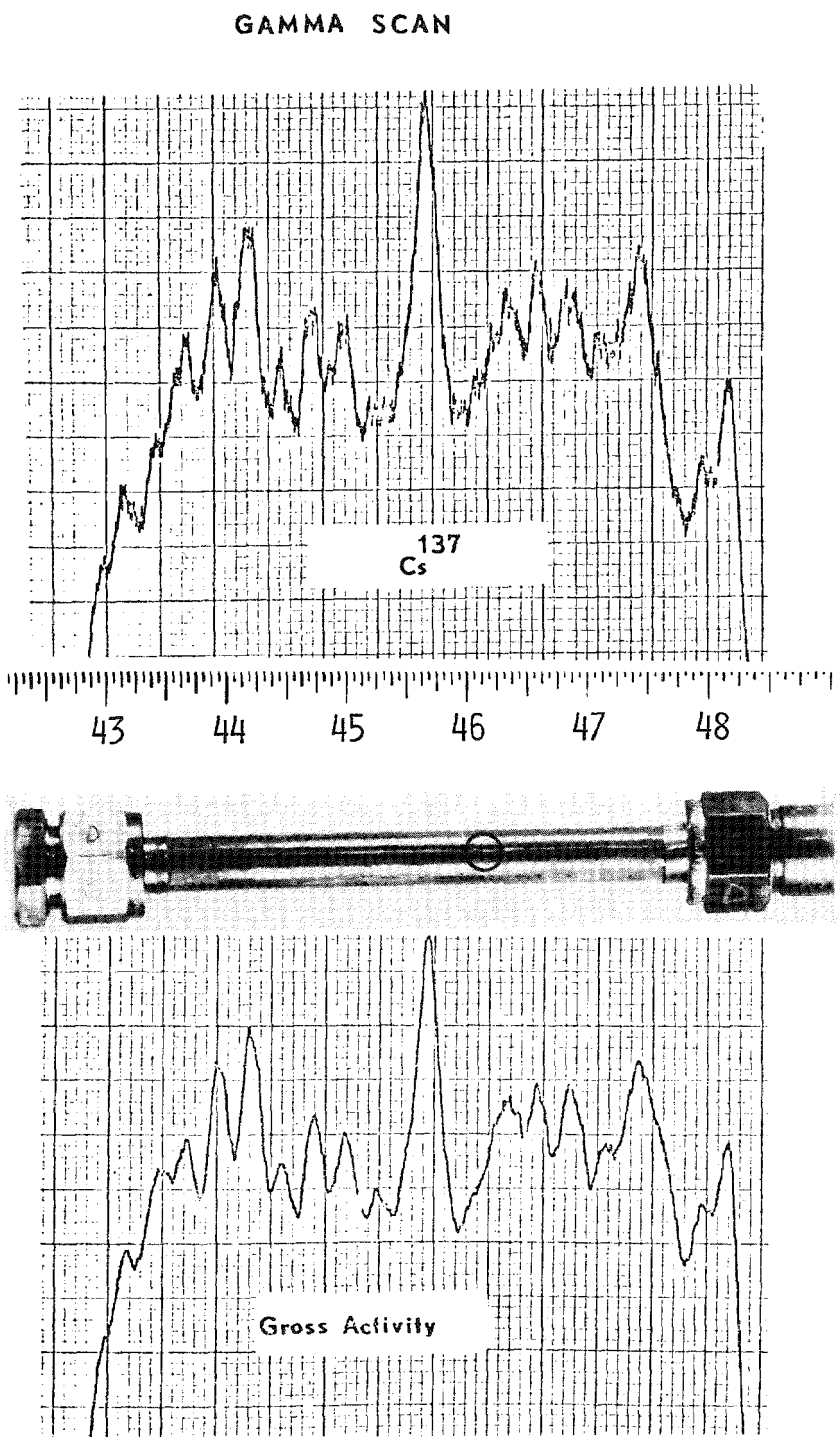

Fig. 4-4. Cs^{137} Profile in specimen 165F-9 from a medium-burnup, high-gas-release BRP fuel rod.

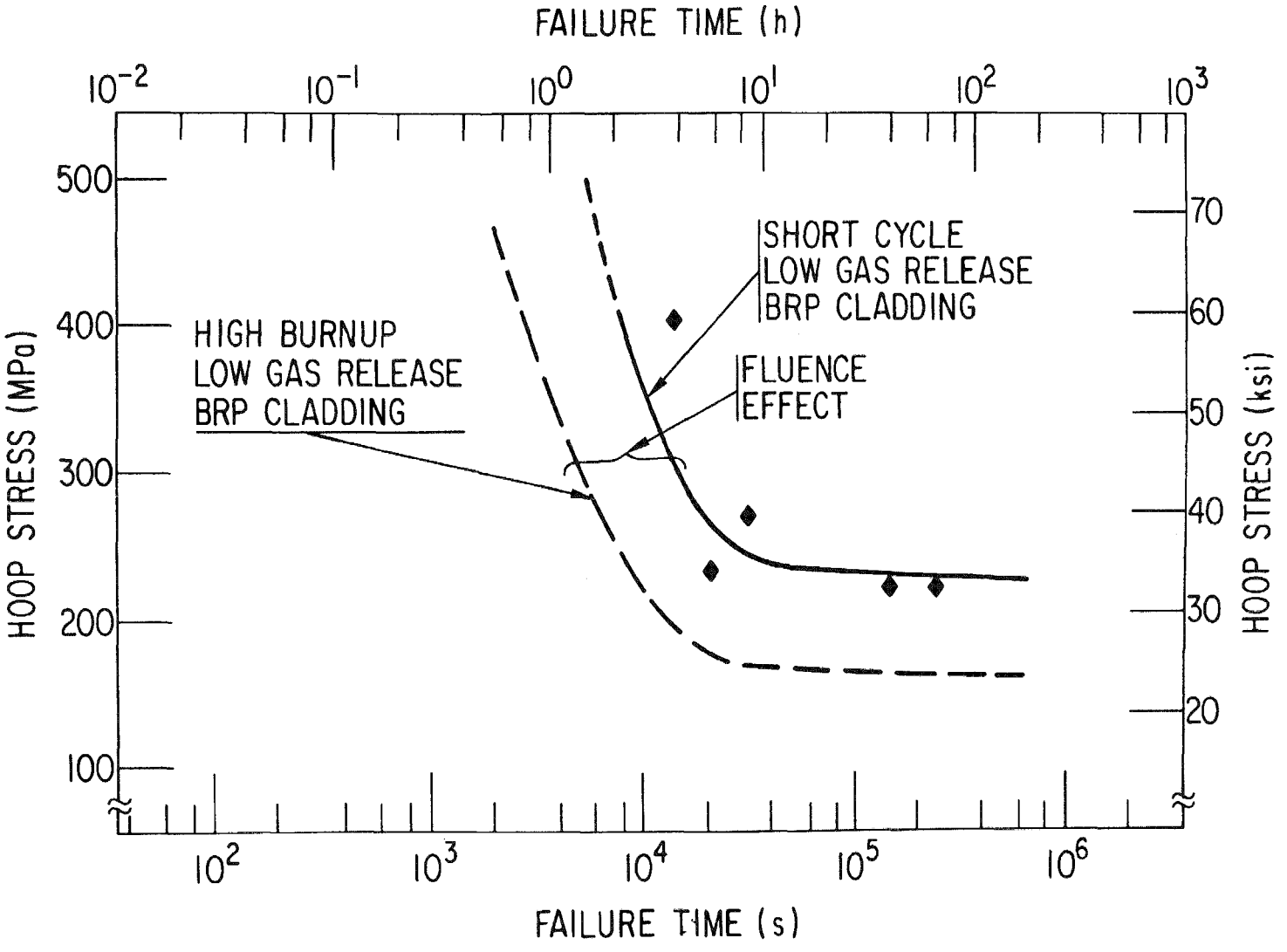

Fig. 4-5. Results of iodine SCC tests on low-burnup BRP cladding at 598 K.

Table 4-6

RESULTS OF BIAXIAL IODINE SCC TESTS ON LOW-BURNUP BRP CLADDING AT 325°C (Bu ∿1 MWd/kg U)

Specimen Number	Iodine Amount (mg)	Iodine Conc. (mg/cm^2)	Pressure Steps	Hoop Stress MPa	Hoop Stress (ksi)	Time to Failure (h)	Failure Mode[a]	Failure Strain (%)	Failure Location[b]
165AA8	25.0	0.65	1	224	(32.41)	68.22	P	∿0.04	2 1/4 TE
165AB12	25.0	0.65	1	227	(32.92)	40.34	P	∿0.04	2 TE
165AA7	25.0	0.65	1	236	(34.18)	5.92	P	∿0.02	1/2 TE
165AA10	25.0	0.65	1	275	(39.87)	8.4	P	∿0.07	3 TE
165AB1	24.9	0.65	1	409	(59.37)	3.77	P	∿0.18	1 TE

[a] P indicates pinhole.

[b] 2 TE indicates failure site located 2 tube diameters from top end.

Table 4-7

RESULTS OF CUMULATIVE DAMAGE TESTS FOR HIGH-BURNUP QC AND BRP CLADDING AT 325°C

Specimen Number	Cladding Type	Fission-gas Release (%)	σ_1 MPa	σ_1 (ksi)	t_1(a) (min)	Ratio $\frac{t_1(\sigma_1)}{t_{f\text{-}1}(\sigma_1)}$	σ_2 MPa	σ_2 (ksi)	Total Time (min)	t_2(b) (min)	Ratio $\frac{t_2(\sigma_2)}{t_{f\text{-}2}(\sigma_2)}$	Failure Mode(c) & Length (cm)	D_c(d)	$\Delta\sigma$(e) MPa
190D2-7	QC Annealed Zircaloy-2	Low	274	(39.76)	57.12	0.440	412	(59.74)	63.92	6.8	0.176	C (1.6)	0.616	+138
190D2-8		Low	418	(60.45)	19.26	0.498	279	(40.42)	79.02	59.76	0.460	C (1.4)	0.958	-139
165U-6	BRP Cladding CW-SR Zircaloy-2	0.22	486	(70.50)	12.0	0.345	278	(40.30)	57.1	45.1	0.501	R (8.9)	0.846	-208
165U-13		0.22	480	(69.67)	12.5	0.353	279	(40.48)	65.88	53.38	0.593	R (6.4)	0.946	-201
165U-12		0.22	449	(65.16)	16.0	0.404	242	(35.15)	81.15	65.15	0.603	R (7.6)	1.007	-207
165V-4		13.5	381	(55.24)	28.0	0.467	246	(35.65)	79.67	51.67	0.506	C (3.8)	0.974	-135
165T-8		14.9	275	(39.87)	45.0	0.497	179	(25.98)	66.91	21.91	0.085	R (6.0)	0.582	- 96
165V-6		13.5	189	(27.43)	57.0	0.306	298	(43.15)	109.5	52.50	0.684	P (-)	0.989	+109
165T-4		14.9	275	(39.87)	45.0	0.497	152	(22.02)	103	58.0	0.016	C (1.2)	0.513	-123

QC cladding Bu ~30 MWd/kg U; BRP cladding Bu ~29 MWd/kg U.

(a) Hold time at initial stress σ_1 [$t_1 = (1/2)t_{f\text{-}1}$]

(b) Time to failure at σ_2

(c) C indicates crack; P indicates pinhole; R indicates rupture

(d) D_c indicates damage coefficient in Eq. [4-3]

(e) $\Delta\sigma = \sigma_2 - \sigma_1$ stress increment ($\sigma_2 > \sigma_1$), decrement ($\sigma_2 < \sigma_1$).

in the above expression. Figure 4-6, reproduced from the interim report, shows the SCC curve for the QC cladding and illustrates the manner in which t_1 was established. The QC data are tabulated in Table 4-8. Figure 4-2 was used for the BRP cladding.

The two cumulative-damage tests on QC cladding included one stress-increment test where σ_1 and σ_2 were 274 and 412 MPa, respectively, and one stress-decrement test where σ_1 and σ_2 were 418 and 279 MPa, respectively.

Six of the seven cumulative-damage tests on BRP cladding were stress-decrement tests; one was a stress-increment test. The stress-decrement tests included specimen 165U-6 with σ_1 = 486 MPa and σ_2 = 278 MPa, specimen 165U-13 with σ_1 = 480 MPa and σ_2 = 279 MPa, specimen 165U-12 with σ_1 = 449 MPa and σ_2 = 242 MPa, specimen 165V-4 with σ_1 = 381 MPa and σ_2 = 246 MPa, specimen 165T8 with σ_1 = 275 MPa and σ_2 = 179 MPa, and specimen 165T-4 with σ_1 = 275 MPa and σ_2 = 152 MPa. The single stress-increment test was conducted on specimen 165V-6 with σ_1 = 189 MPa and σ_2 = 298 MPa. Specimens 165V-4, 165V-6, and 165T-4, and 165T-8 were found to be from high-fission-gas-release fuel rods.

The experimental data are analyzed in accordance with the simple linear damage rule:

$$D_c = \frac{t_1(\sigma_1)}{t_{f_1}(\sigma_1)} + \frac{t_2(\sigma_2)}{t_{f_2}(\sigma_2)} \qquad (4\text{-}3)$$

$$\Delta\sigma = \sigma_2 - \sigma_1 \quad ,$$

where D_c = Damage coefficient leading to SCC failure,

σ_1 = Initial cladding stress,

t_1 = Holding time at σ_1,

t_{f_1} = Time to failure accrued in the initial step of an SCC test,

σ_2 = Final cladding stress,

t_2 = Time to failure at σ_2,

t_{f_2} = Time to failure accrued in the final step of an SCC test,

and

Table 4-8

RESULTS OF BIAXIAL IODINE SCC TESTS ON IRRADIATED QUAD CITIES CLADDING AT 325°C

Specimen Number	Iodine Amount (mg)	Iodine Conc.$_2$ (mg/cm^2)	Pressure Step	Hoop Stress, Mpa (ksi)	Time (h)	Total Time (h)	Failure Mode[a]	Failure Strain (%)	Failure Location[b]
190D1-6	24.6	0.56	1	198.7 (28.82)	6.5	6.5	P	0.01	M
190D1-2	25.5	0.66	1	164.0 (23.79)	20.5				
			2	177.2 (25.70)	26.2				
			3	182.0 (26.40)	18.7[c]	65.4	P	0.06	3/4 BE
190D2-5	26.5	0.60	1	183.9 (26.67)	1.4[c]	1.4	P	0.01	1 BE
190D1-3	24.5	0.55	1	274.2 (39.76)	1.75[c]	1.75	P	0.01	M
190D1-4	24.8	0.56	1	274.2 (39.76)	2.58[c]	2.58	P	0.01	2 BE
190D1-5	24.8	0.56	1	411.9 (59.74)	0.69[c]	0.69	R	0.03	2 BE
190D1-7	25.8	0.58	1	411.9 (59.74)	0.60[c]	0.60	R	0.16	2 BE
190D2-7	25.4	0.57	1	274.2 (39.76)	0.952				
			2	411.9 (59.74)	0.110[c]	1.062	R	0.04	1 BE
190D2-8	24.8	0.56	1	416.8 (60.45)	0.321				
			2	278.7 (40.42)	0.996[c]	1.317	C	0.01	2 TE

[a] P indicates pinhole; R indicates rupture; C indicates axial cracking.

[b] M indicates middle of specimen within 1/2 tube OD; numbers indicate distance from top end (TE) or bottom end (BE), in tube ODs.

[c] Time when specimen failed.

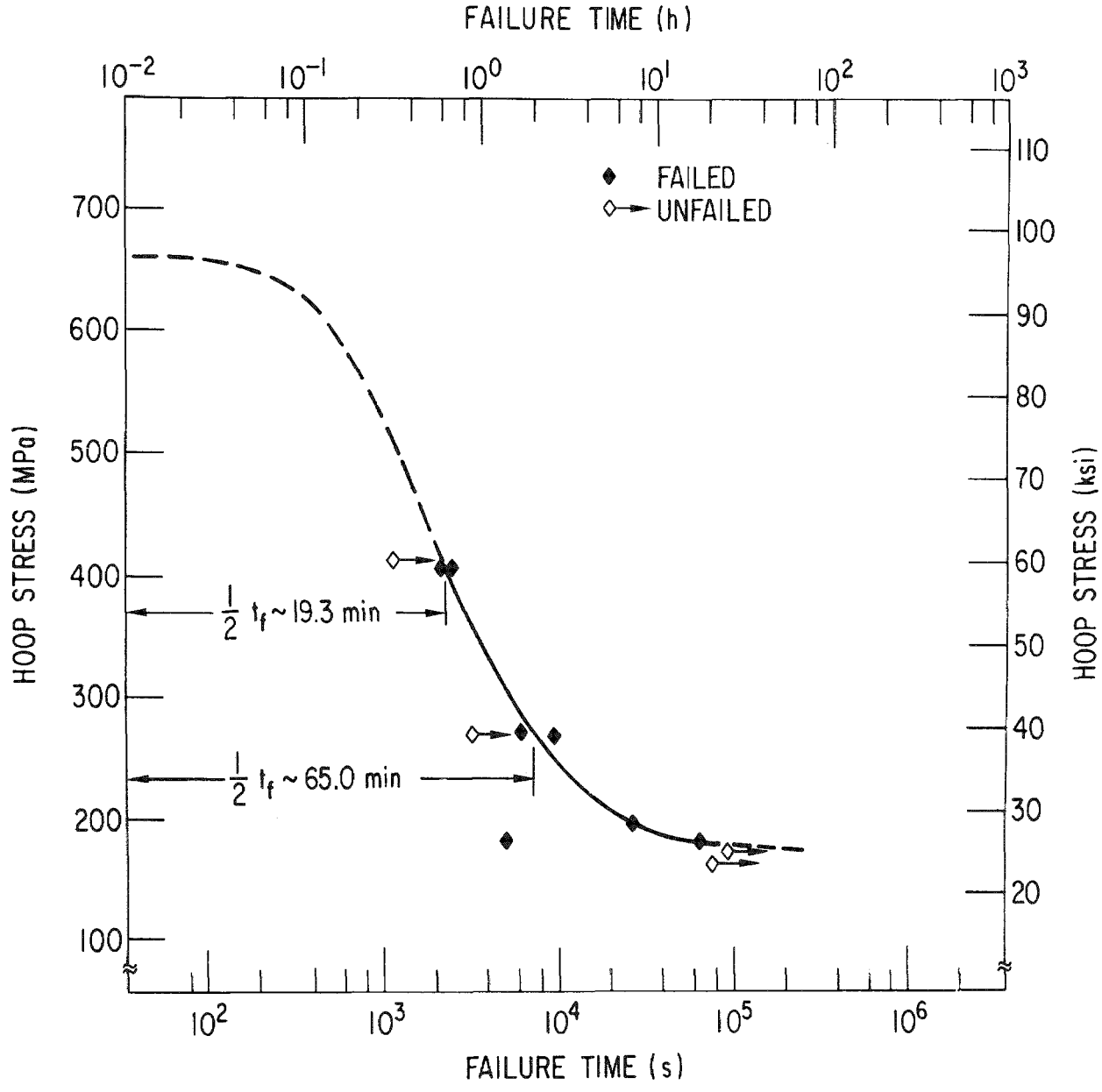

Fig. 4-6. Results of iodine SCC tests on irradiated QC cladding at 598 K illustrating the manner in which cumulative-damage-test parameters were established.

$\Delta\sigma$ = Stress increment when $\sigma_2 > \sigma_1$, and stress decrement when $\sigma_2 < \sigma_1$.

The damage accumulation in the specimen is presumed linear when the value of D_c in Eq. 4-3 approaches unity for iodine-induced SCC failure.

Two of the cumulative-damage results in Table 4-7 do not support the linear-damage rule in Eq. 4-3. Seven of the tests were stress-decrement tests ($-\Delta\sigma$), and two were stress-increment tests ($+\Delta\sigma$). Only five of the seven stress-decrement tests (QC specimen 190D2-8 and BRP specimens 165U-6, 165U-13, 165U-12, and 165V-4) exhibited an apparent agreement with the linear-damage rule expressed in Eq. 4-3. The D_c values obtained in these tests varied from 0.846 to 1.007, and the group average ($\overline{D}_c$) was $0.946 \pm .06$. The D_c values for the two remaining stress-decrement tests (BRP specimens 165T-8 and -4) were 0.582 and 0.513, respectively, indicating nonlinear cumulative-damage behavior. Finally, the D_c values for the only two stress-increment tests performed (QC specimen 190D2-7 and BRP specimen 165V-6) were 0.616 and 0.989. Only the value 0.616 is inconsistent with the linear-damage rule expressed in Eq. 4-3. In summary, the results of only six of the nine cumulative-damage tests given in Table 4-7 exhibit apparent agreement with the simple linear-damage rule expressed in Eq. 4-3. Five of these six tests share several points of similarity. All five are stress-decrement tests; they begin with a very high initial stress (σ_1 = 144-211% above the "threshold" stress for BRP cladding and 122% above the "threshold" stress for QC cladding); the residence time at the initial stress is short; and the stress decrements are large. In contrast, the two stress-decrement tests that do not exhibit linear cumulative-damage behavior have a much lower initial stress (approximately 30-50% lower), a correspondingly longer residence time at the initial stress ($\sim$1.6-3.7 times longer), and a smaller stress decrement. Specimens 165T-8 and -4 are also from high-fission-gas-release fuel rods and have significant cesium deposits on the inner surface.

ESTIMATED DATA UNCERTAINTIES

The total uncertainty in the SCC and cumulative-damage tests is estimated to be no greater than $\pm 5\%$. Contributing factors include a ± 2°C uncertainty in temperature, a $\pm 2\%$ uncertainty in specimen pressure, and $\pm 0.1\%$ uncertainty in specimen diameter. The maximum uncertainty in the calculated specimen stress is $\sim 2.7\%$ for specimens with minimum ovality of ≤ 0.02 mm.

TENSILE TESTS

Four tensile tests were conducted during the program. The purpose of these tests was to provide information on the work-hardening characteristics of irradiated cladding and to establish whether tensile data can be used as an indicator of SCC susceptibility. Two samples each of the BRP low-burnup and the QC cladding were tested at two strain rates at 325°C. These tests were successfully run to the desired strain range of 1-2%, but one test (165DB-7) failed to reach the desired strain because of slippage of the grips. Modulus and yield-stress data were still obtained, however. The test results are summarized in Table 4-9 and Figs. 4-7 and 4-8. In general, the increased strain rate resulted in an increased yield strength and elastic modulus and a decreased rate of strain hardening. The stress-strain curves show no evidence of a distinct yield point, except for specimen 165DB-7. The observed yield point in this specimen is probably not real, but rather is the result of grip slippage. The yield strength of the BRP low-burnup cladding is ∿50 MPa less than the yield point of the QC cladding, which is consistent with the higher fluence received by the QC fuel rods. Fracture did not occur in any of the tensile specimens.

POSTTEST EXAMINATIONS

Following the additional SCC testing, selected specimens from HBR, low-burnup BRP, medium-burnup BRP, and high-burnup BRP were examined in detail using optical metallography and SEM in order to characterize the failures. The examinations performed since the interim report are summarized in Table 4-10.

H. B. Robinson Cladding

Cracks that caused the iodine SCC in HBR specimens were examined by both metallography and SEM. A composite photograph of the entire cross section of specimen 155BC7 [360°C, 273 MPa (39.6 ksi), 2.19 ks (0.61 h)]* is shown in Fig. 4-9. The crack that penetrated through the cladding is located at the top of the figure. The most important feature of the cross section is the large number of secondary cracks that are present. A closeup of one section of the cladding is shown in Fig. 4-10. Numerous smaller cracks can be observed between the larger cracks. At higher magnification, the cracks were found to start at either locations where the inner-surface oxide was absent or where a crack in the oxide was present as shown in Fig. 4-11. More than 100 cracks were found in this cross section. Metallographic examination of specimen 155BDC9 [325°C, 275 MPa (40 ksi), 0.1 ks (0.03 h)] revealed a similar amount of secondary cracking around the circumference.

*Test temperature, test stress, and time to failure.

Table 4-9

SUMMARY OF TENSILE TEST RESULTS AT 325°C

Cladding Source	Specimen Number	Strain Rate (s^{-1})	Yield Strength (MPa)	Young's Modulus (MPa)	Strain-Hardening Exponent	$\frac{\Delta D}{Do}$ (%)
BRP	165DB-7	3.3×10^{-5}	500	7.78×10^{4}	--	~0.1
BRP	165DB-8	3.3×10^{-4}	570	8.06×10^{4}	.070	1.1
QC	190D3-5	3.3×10^{-5}	545	8.06×10^{4}	.077	1.2
QC	190D3-6	3.3×10^{-4}	620	8.32×10^{4}	.098	1.1

Table 4-10

SUMMARY OF POSTTEST EXAMINATIONS

Specimen Number	Reactor	Test Conditions: Temp. (°C)	Test Conditions: Stress (MPa)	Test Conditions: Failure Time (h)	Examination	Fracture Characteristics	Remarks
155BC7	HBR	360	273	0.61	Metallography	Crack branching	~100 SCC cracks initiated around circumference
155BC5	HBR	325	414	1.49	SEM	Low crack length to depth ratio - crack branching	Extensive chemical attack on inner surface
165AB1	BRP low burnup	325	409	3.77	SEM	Crack branching - Failure occurred by ductile stress rupture	Multiple cracks on inner surface
165AA10	BRP low burnup	325	275	8.4	SEM	Crack branching	--
165AB12	BRP low burnup	325	227	40.3	SEM	No crack branching - Extensive chemical attack	Areas rich in iron were preferentially attacked
165E4	BRP low burnup	325	311	3.1	SEM	Crack branching - No observable chemical attack	Very clean inner surface - No chemical attack
165E11	BRP medium burnup	325	277	1.02	SEM	Creep rupture	--
165F7C	BRP medium burnup	325	266	0.84	Metallography	Multiple cracks	Many associated with fracture of oxide layer. No massive fission-product deposits.
165T18A	BRP high burnup	325	151	7.7	SEM	No crack branching - Extensive chemical attack	Crystals containing Cs and I observed along crack and on fracture surface

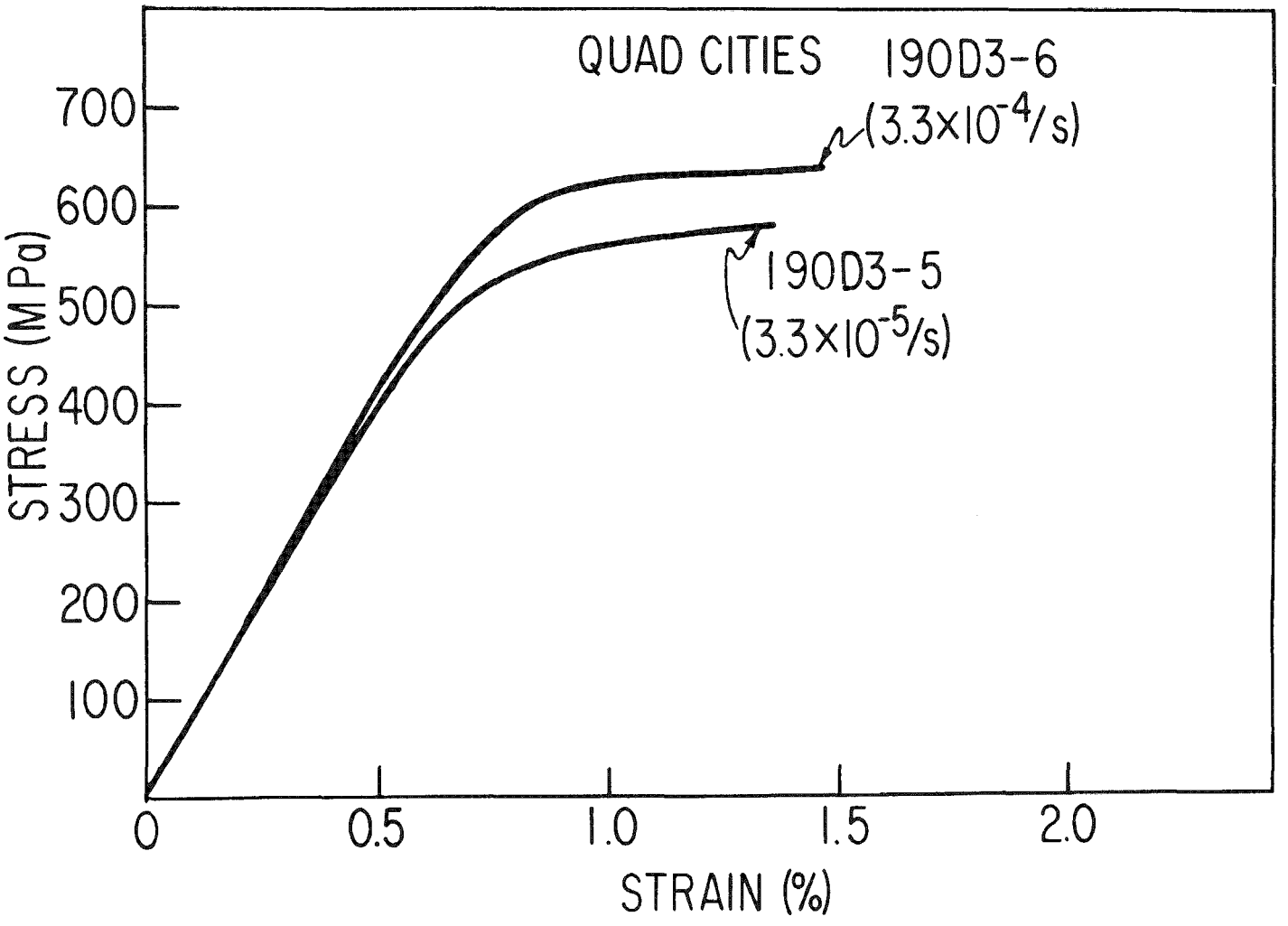

Fig. 4-7. Stress-strain curves for QC specimens tested at 325°C.

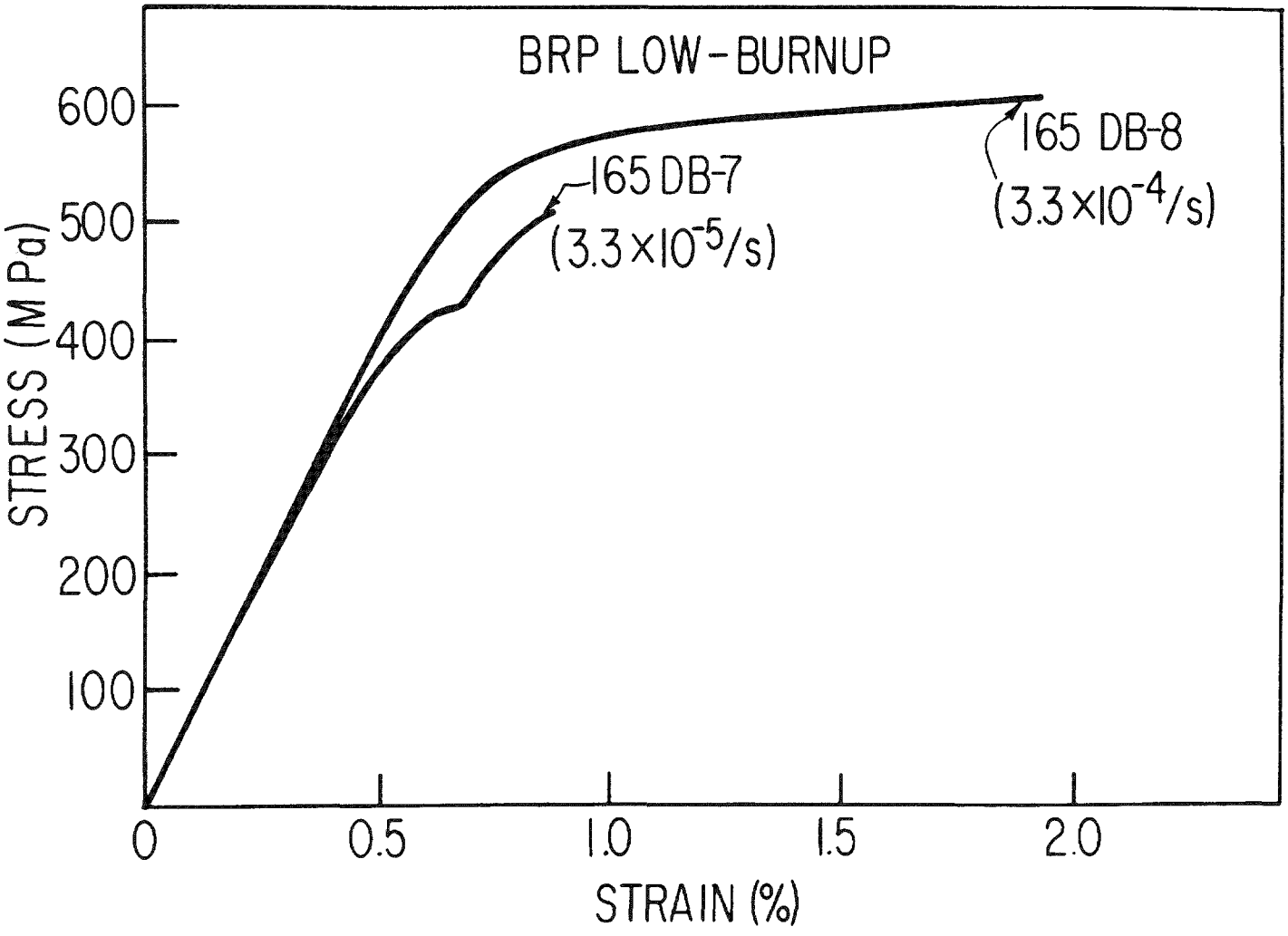

Fig. 4-8. Stress-strain curves for low-burnup BRP specimens tested at 325°C.

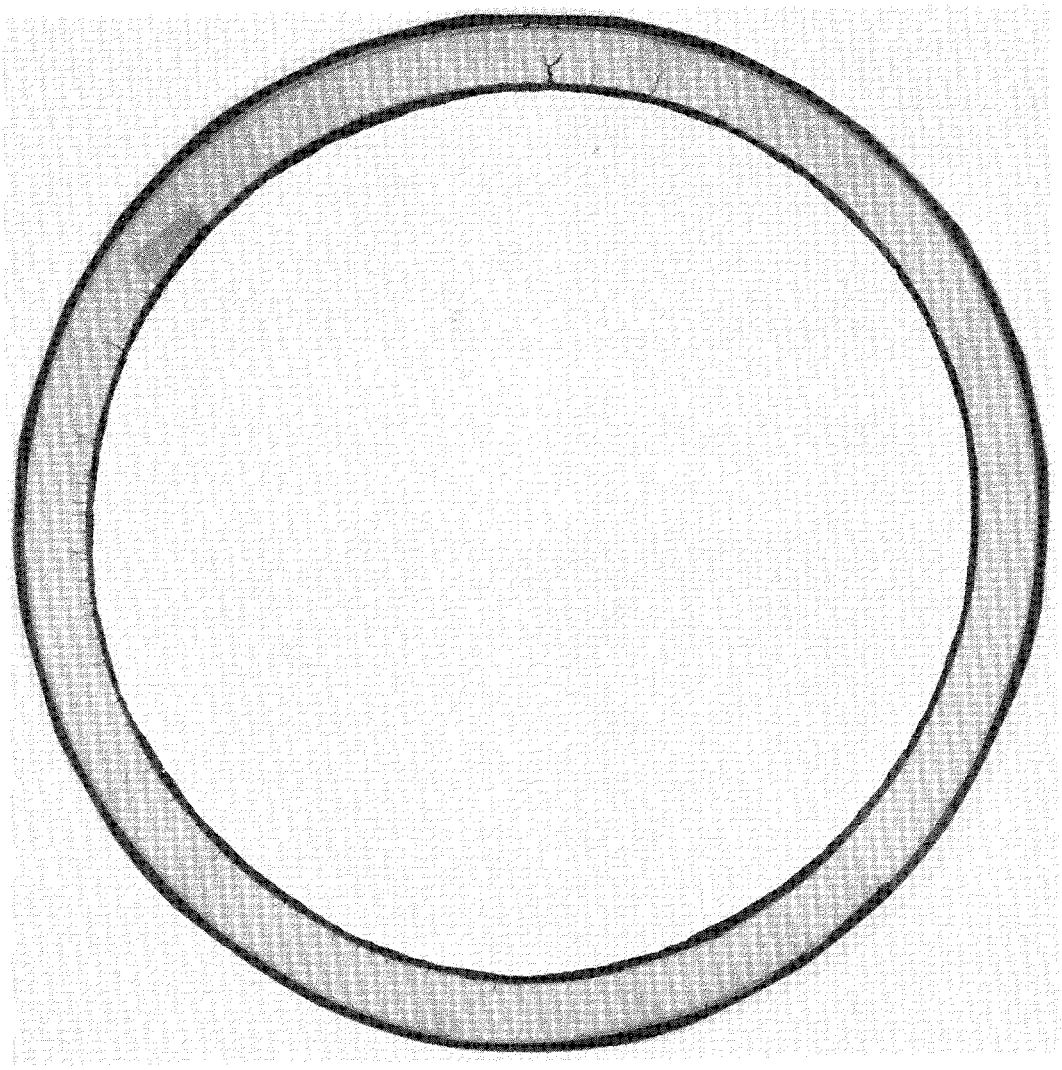

Fig. 4-9. Cross section of HBR specimen 155BC7 showing SCC cracks (15X).

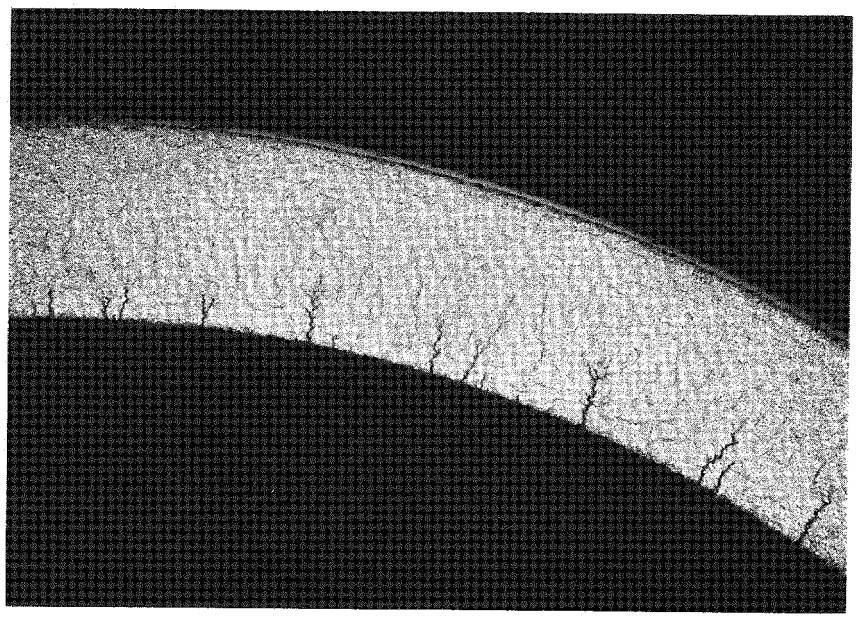

Fig. 4-10. Cross section of HBR specimen 155BC7 showing SCC cracks (50X).

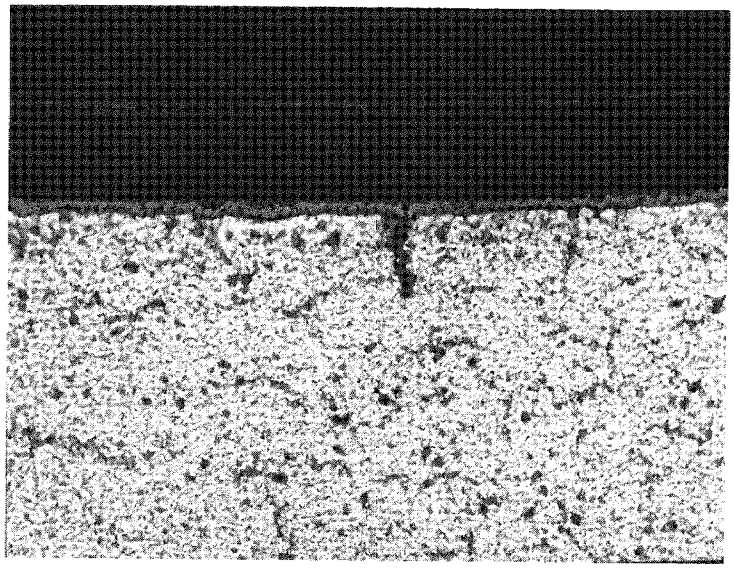

Fig. 4-11. SCC crack at location of oxide crack on inner surface of HBR specimen 155BC7 (250X).

The SCC failure in specimen 155BC5 [325°C, 414 MPa (60.0 ksi), 5.38 ks (1.49 h)] was also examined in the SEM. The failure on the inner surface was first examined in the as-tested condition and then was ultrasonically cleaned and reexamined. The fracture surface was exposed by three-point bending and then examined. Figure 4-12 shows the composite photographs of the failure. The crack was ∿2.5 mm long and was almost completely covered by corrosion product (Fig. 4-12a).

The cleaned surface showed a large amount of pitting. The fracture surface exhibits crack branching at a crack depth of ∿150 μm. The crack length-to-depth ratio is ∿4, which is lower than has been observed in other SCC failures. At high magnification (Fig. 4-13), evidence of pitting and chemical attack can be seen near the inner surface. The rest of the fracture surface exhibits a cleavage-like appearance, with a few isolated areas of fluting. High-magnification photographs of the regions of chemical attack and cleavage are shown in Fig. 4-14.

BRP Low Burnup

Three BRP low-burnup specimens were examined in the SEM. The three specimens were tested at different stresses, but each failed in the pinhole mode. The failure in specimen 165AB1 [325°C, 409 MPa (59.4 ksi), 13.6 ks (3.77 h)] is shown in Fig. 4-15 as tested, after ultrasonic cleaning, and after three-point bending. There are multiple cracks along the 10-mm length of the failure, and one section of the failure is covered with corrosion product. The cleaned surface shows little evidence of gross chemical attack along the failure. The exposed fracture shows crack branching at ∿150 μm from the inner surface. The length-to-depth ratio of this crack is ∿10, similar to that observed in other failed specimens. At high magnification (Fig. 4-16), evidence of chemical attack was observed up to the point of crack branching. This fracture surface is followed by an area ∿250 μm long of cleavage-like fracture, which shows some evidence of ductility. The remaining fracture surface is composed of ductile cup-cone fracture. The final failure mode in this specimen apparently was ductile rupture, which is consistent with the high stress level of the SCC test.

The failure in specimen 165AA10 [325°C, 275 MPa (39.9 ksi), 30.2 ks (8.4 h)] is shown in Fig. 4-17 as tested, after ultrasonic cleaning, and after three point bending. Again, multiple cracks are observed along the failure, but the cracks are narrower than those in 165AB1. Corrosion product is seen along the cracks, but there is little evdience of gross chemical attack. The exposed fracture surface reveals that crack branching occurred at ∿250 μm from the inner surface and that

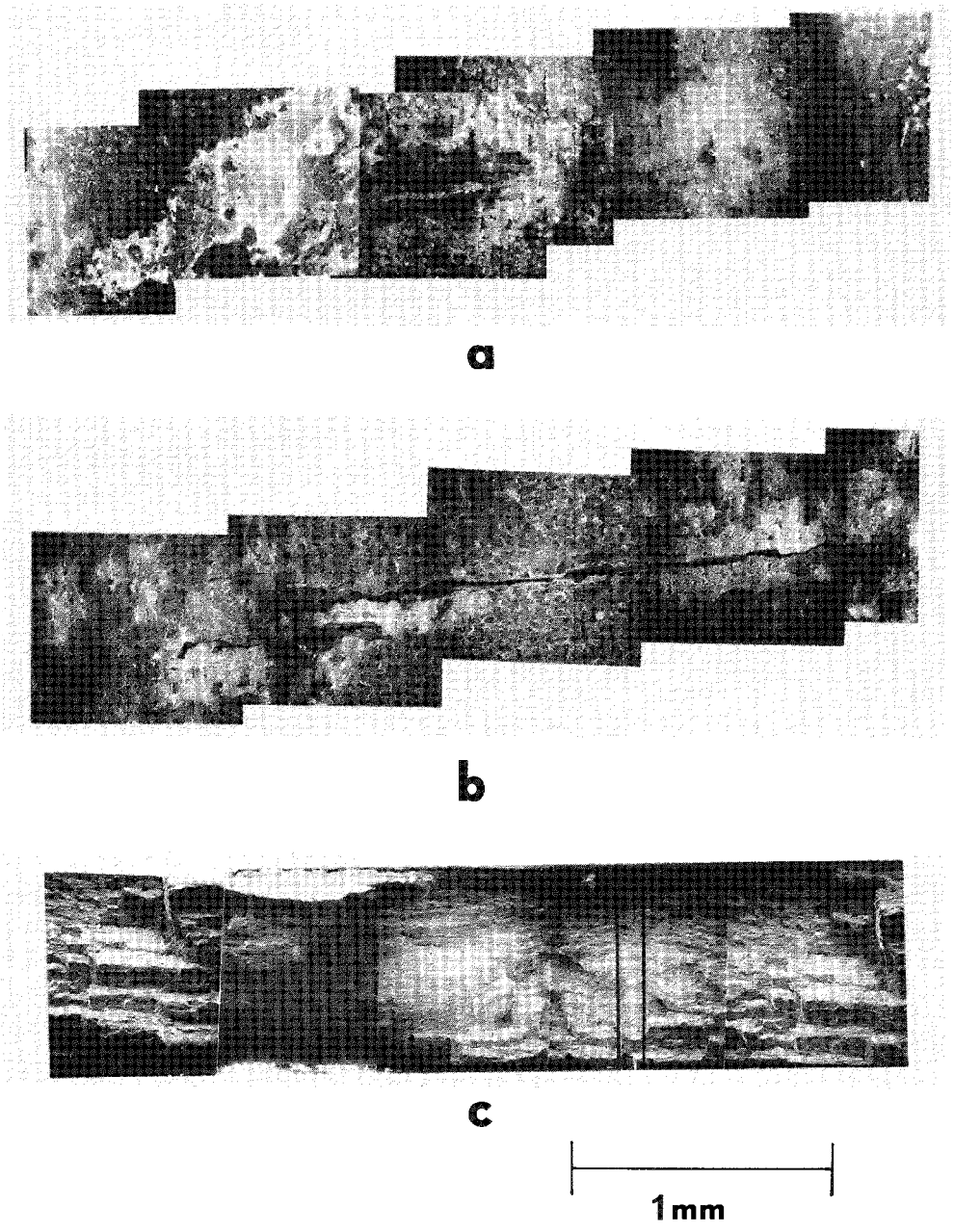

Fig. 4-12. SCC failure in HBR specimen 155BC5 (composite). (a) as tested, (b) after ultrasonic cleaning, (c) after three-point bending.

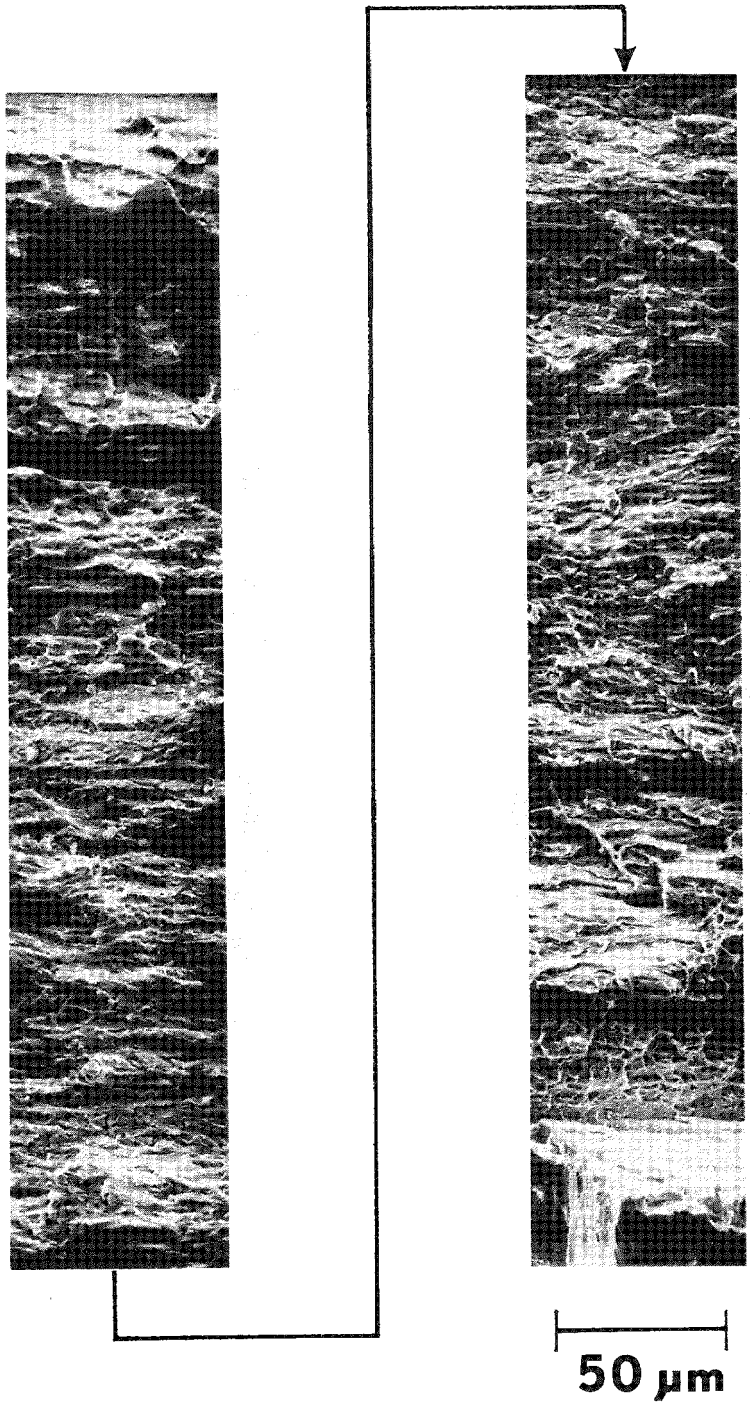

Fig. 4-13. High-magnification composite of fracture surface of HBR specimen 155BC5 located between vertical lines in Fig. 4-12c.

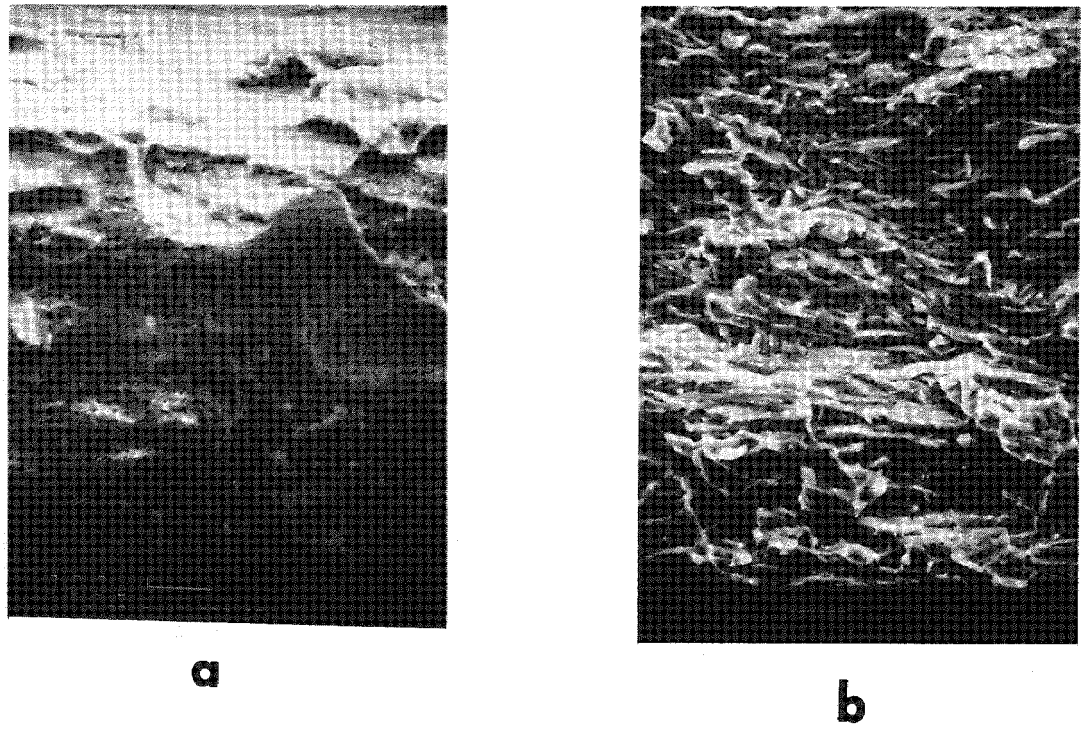

Fig. 4-14. Fracture surface of SCC failure in HBR specimen 155BC5. (a) area of chemical attack, (b) area showing cleavage fracture.

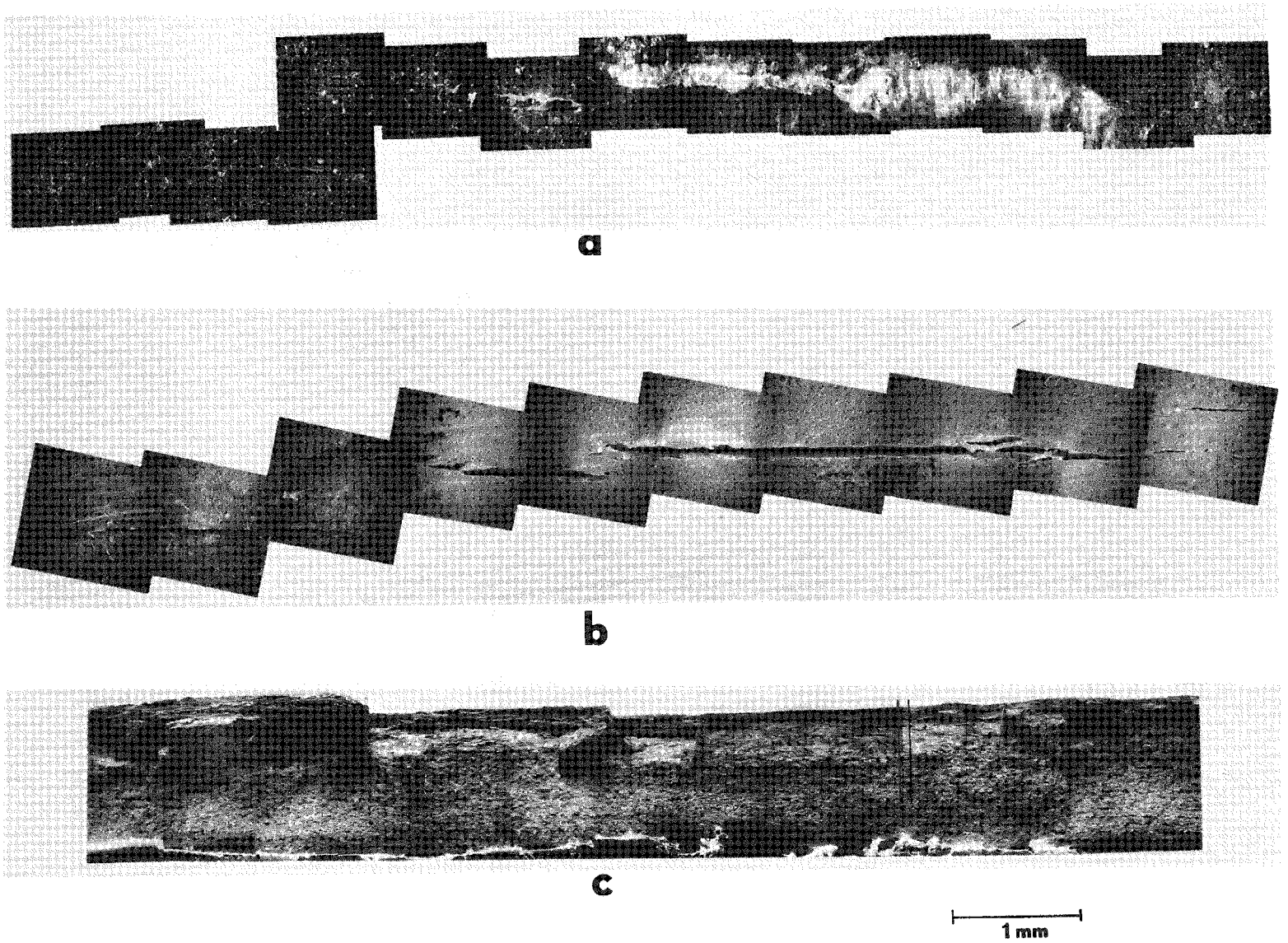

Fig. 4-15. Fracture surface of SCC failure in HBR specimen 165AB1 (composite). (a) as tested, (b) after ultrasonic cleaning, (c) after three-point bending.

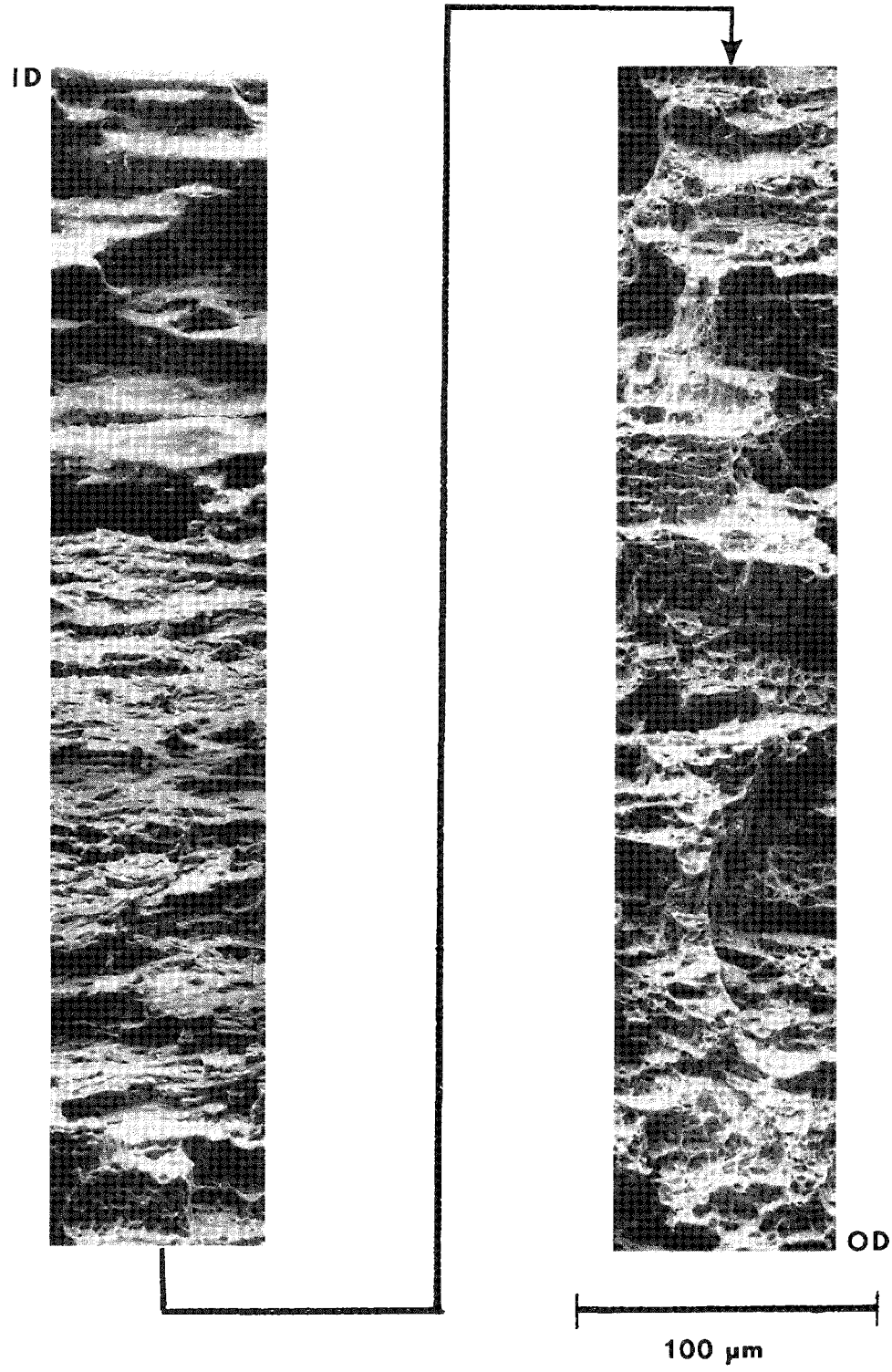

Fig. 4-16. High-magnification composite of fracture surface of BRP specimen 165AB1 located between vertical lines in Fig. 4-15c.

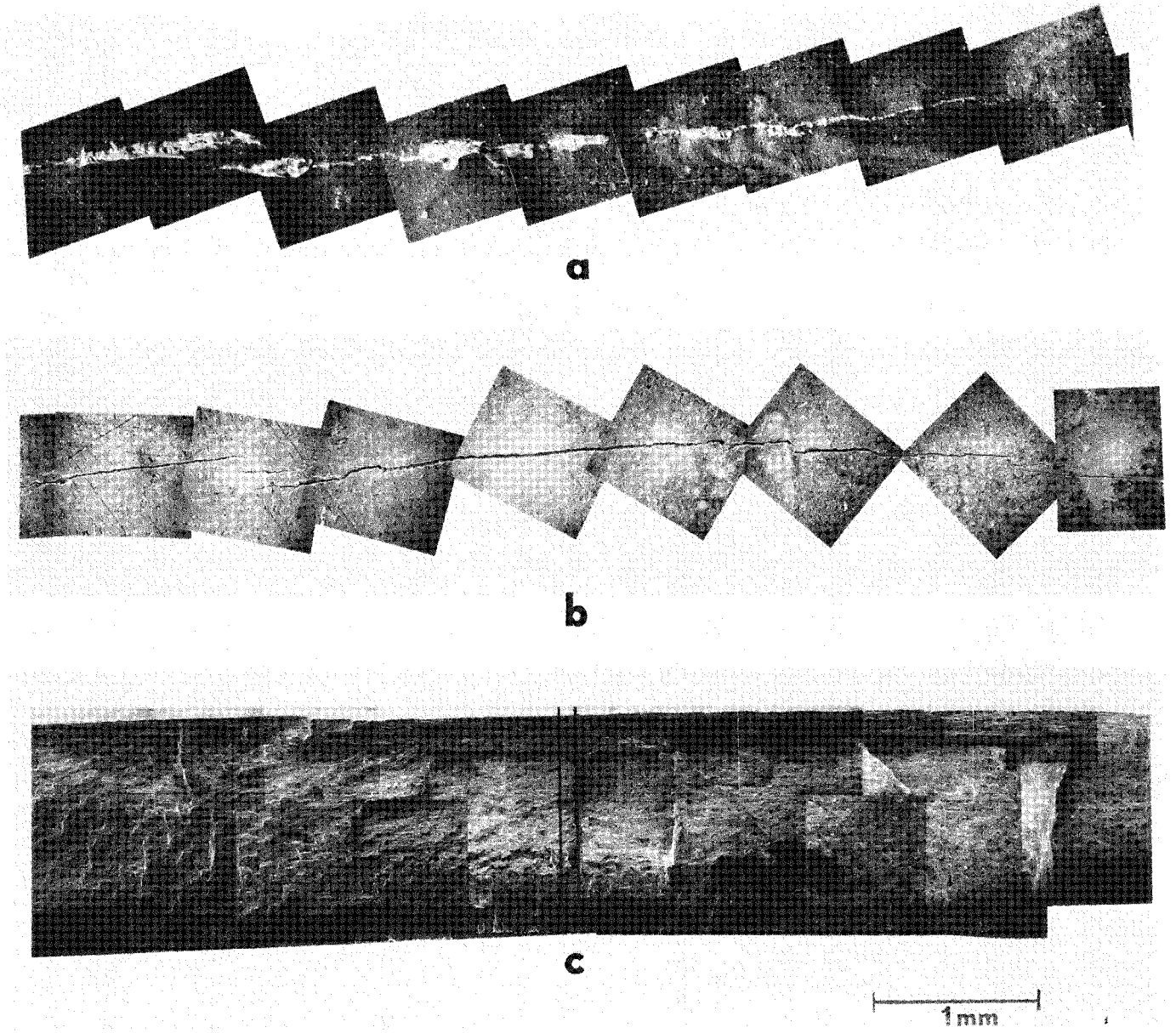

Fig. 4-17. SCC failure in BRP specimen 165AA10. (a) as tested, (b) after ultrasonic cleaning, (c) after three-point bending.

the crack length-to-depth ratio is ∿7. At high magnification (Fig. 4-18), evidence of chemical attack can be seen up to the point of crack branching. This is followed by an area of cleavage-like failure for the next ∿700 μm, which is then followed by ductile cup-cone fracture. Again, as with specimen 165AB1, the final failure mode was ductile rupture, but the depth of the SCC portion of the failure is much greater in specimen 165AB10.

The failure in specimen 165AB12 [325°C, 227 MPa (33.0 ksi), 145.2 ks (40.3 h)] is shown in Fig. 4-19. In contrast to the previous two specimens, the failure in 165AB12 is in the form of one long crack, and there is evidence of substantial chemical attack in the form of severe pitting. The exposed fracture surface shows no evidence of crack branching, and the chemical attack can be seen to continue to the outer surface. At high magnification (Fig. 4-20), the chemical attack is clearly evident near the inner surface. The clean SCC fracture areas following the area of chemical attack are similar in appearance to the fracture surface in specimen 165AA10.

The pitting, observed on the surface of the specimen in the as-tested condition, is shown in Fig. 4-21 at high magnification. The corrosion product at the pit sites was analyzed by X-ray analysis and was determined to be rich in both iodine and iron, as shown in Fig. 4-21b. At locations away from the pits, such as location B in Fig. 4-21a, only zirconium was detected, as shown in Fig. 4-21c. This observation is consistent with those of Cubicciotti, who observed preferential iodine attack at the sites of iron-rich precipitates. (13)

A unique feature was observed on the inner surface of specimen 165AB12 following ultrasonic cleaning. This feature consisted of axial hairline cracks as shown in Fig. 4-22, in patches of oxide that were not removed by ultrasonic cleaning or chemical attack. The hairline cracks are surrounded on either side by dark areas, ∿0.75 μm wide. X-ray analysis of the dark areas indicated the presence of iodine along with zirconium, whereas X-ray analysis of another section of the oxide indicated only the presence of zirconium. This feature is of interest because it could be a precursor to an SCC crack. The axial alignment of the hairline cracks implies an interaction with the applied hoop stress, and the presence of iodine after vigorous ultrasonic cleaning suggests a strong bond between the iodine and the oxide layer.

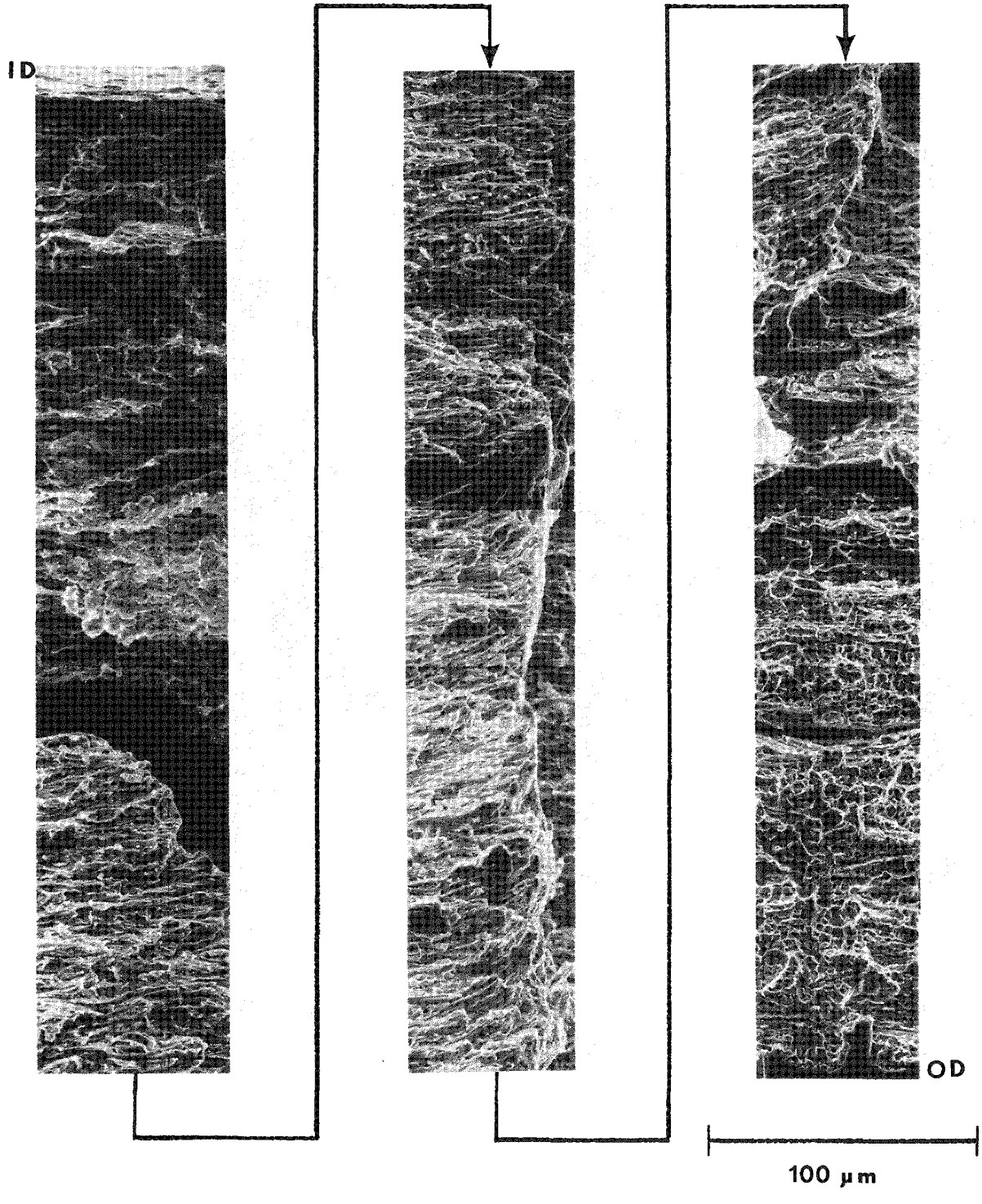

Fig. 4-18. High-magnification composite of fracture surface of BRP specimen 165AA10 located between vertical lines in Fig. 4-17c.

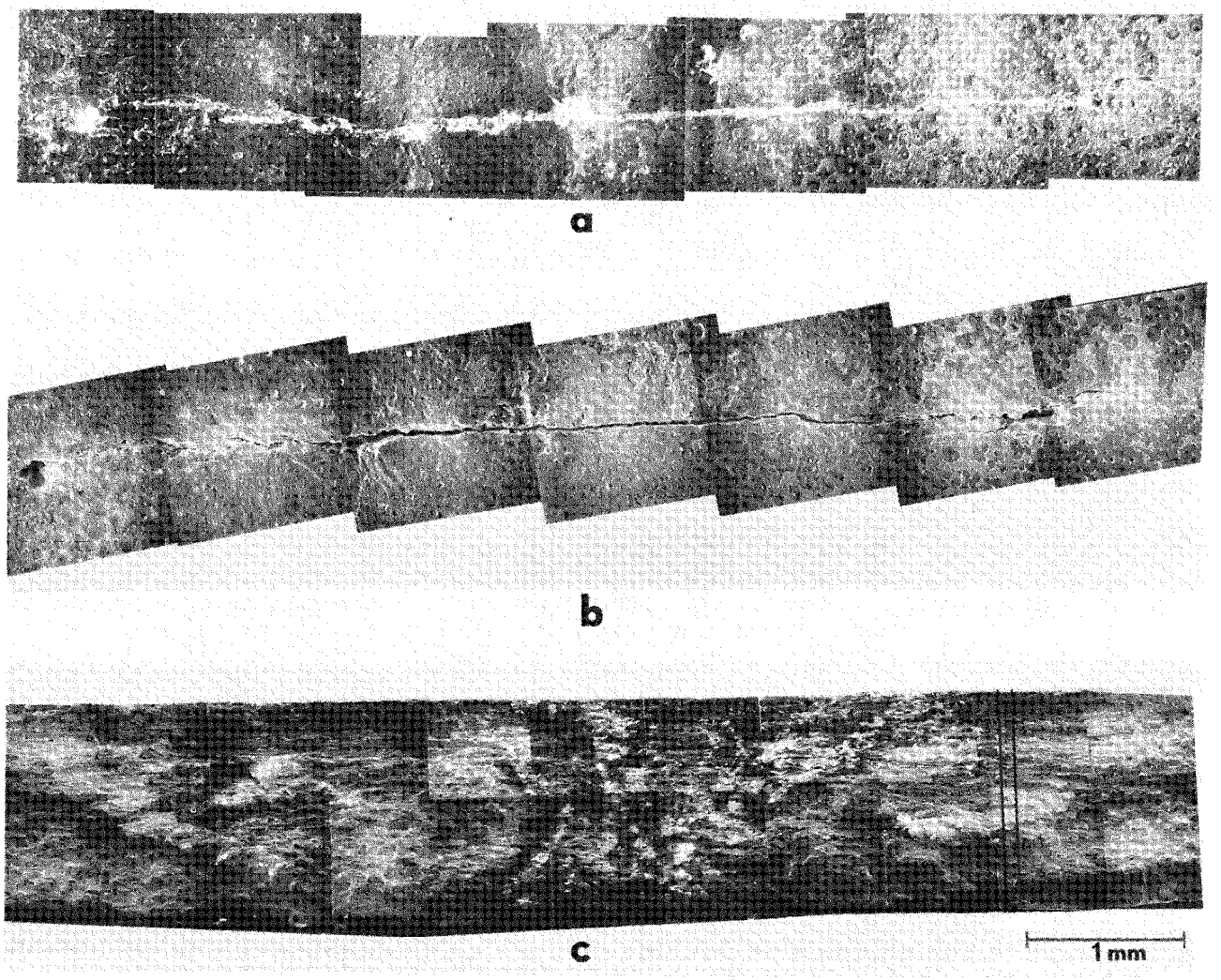

Fig. 4-19. SCC failure in BRP specimen 165AB12. (a) as tested, (b) after ultrasonic cleaning, (c) after three-point bending.

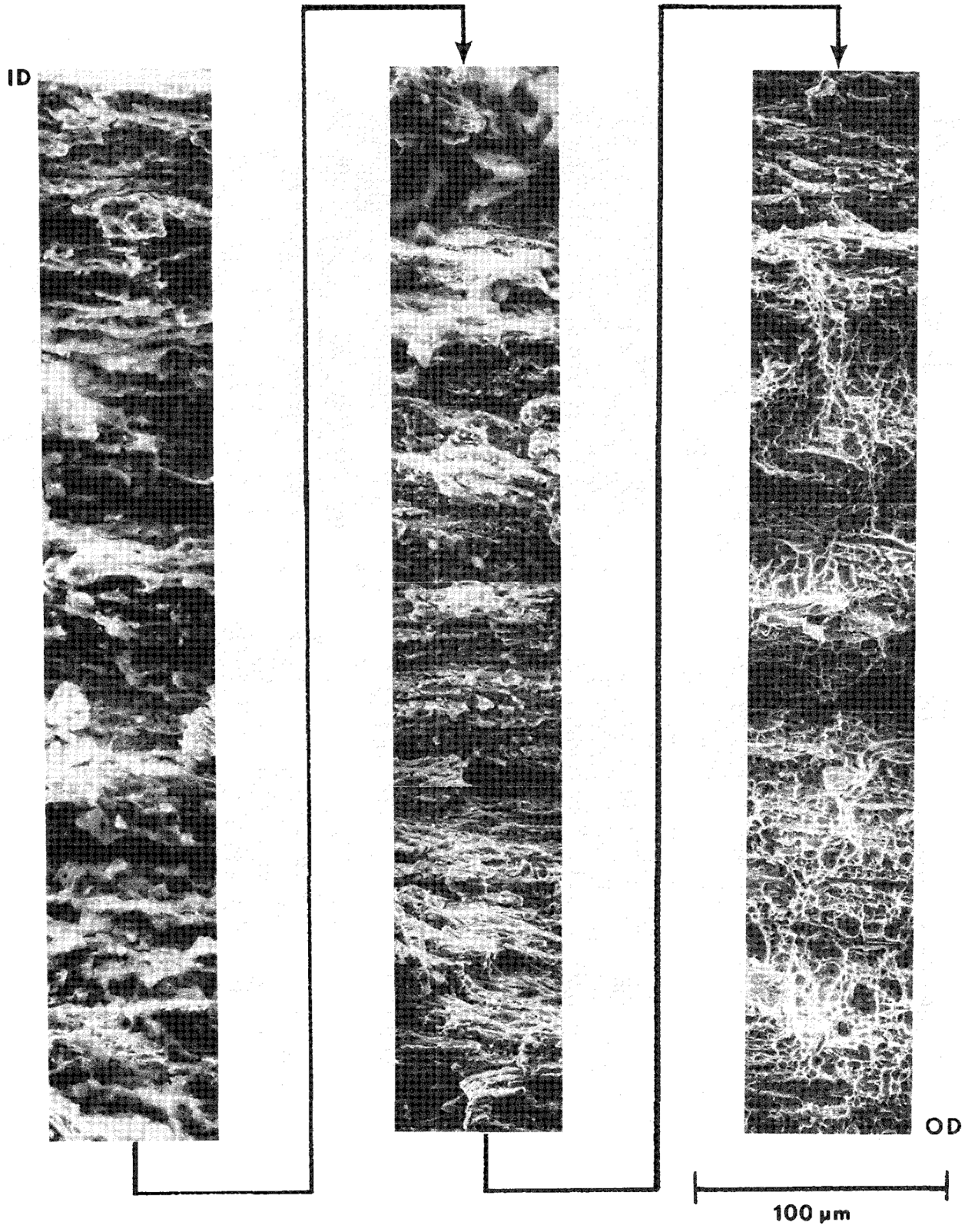

Fig. 4-20. High-magnification composite of fracture surface of BRP specimen 165AB12 located between vertical lines in Fig. 4-19c.

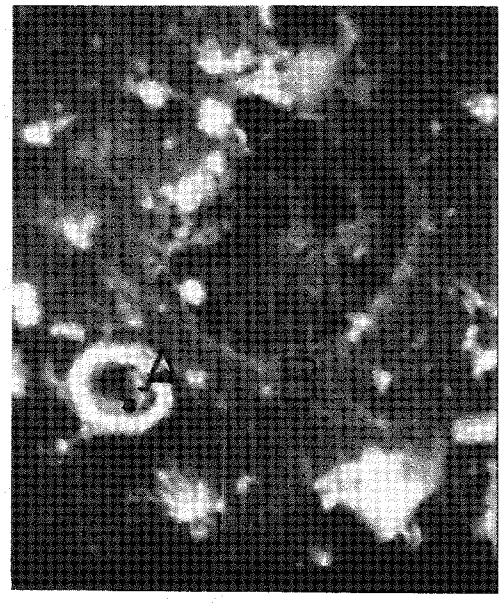

(a)

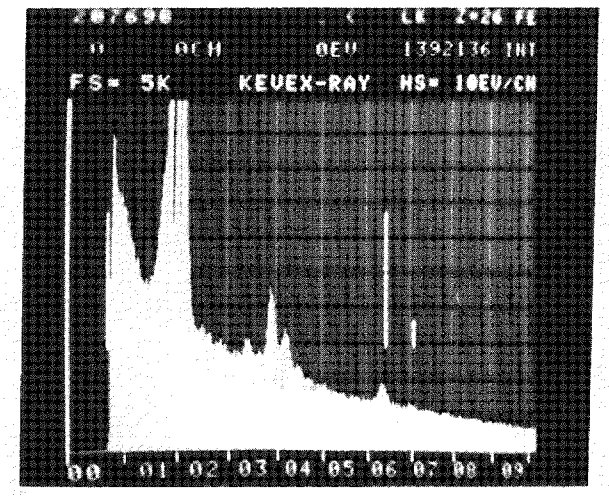

(b)

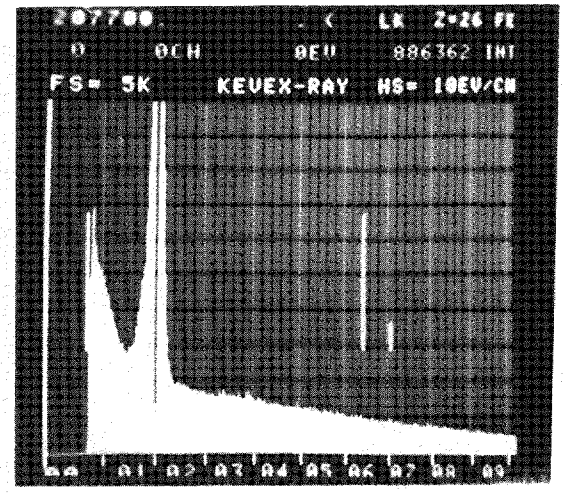

(c)

Fig. 4-21. Photos of SEM examination of inner-surface of BRP specimen 165AB12. (a) pits on inner surface after SCC testing, (b) X-ray spectra from point A showing the presence of iodine and iron, (c) X-ray spectra from point B showing only the Zirconium peak.

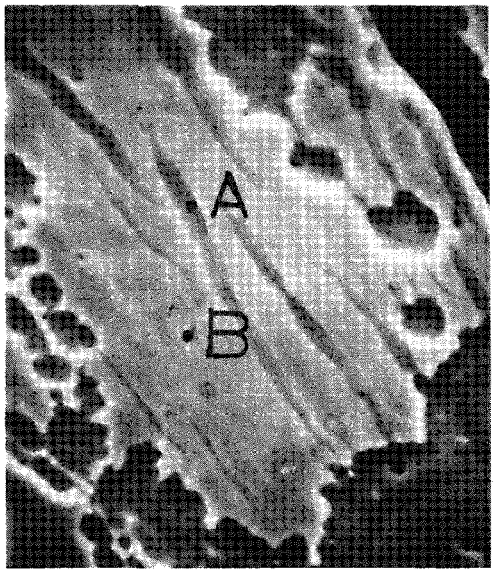

(a)

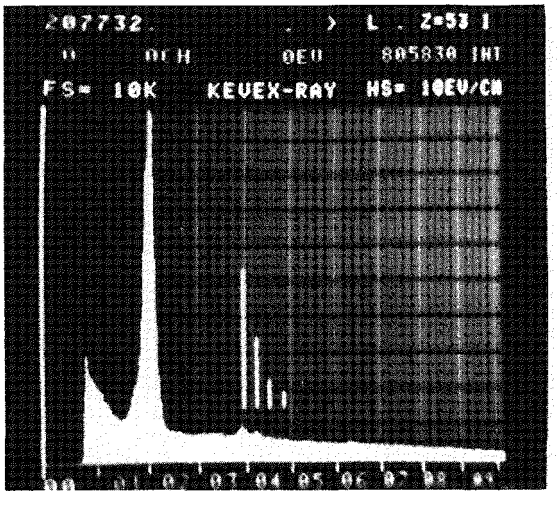

(b)

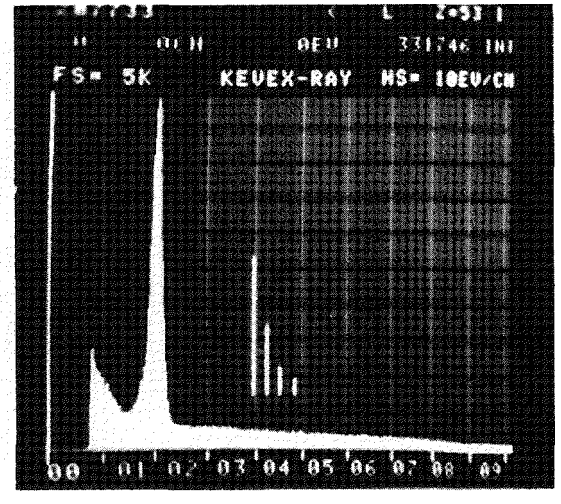

(c)

Fig. 4-22. Photos of SEM examination of inner-surface oxide on BRP specimen 165AB12. (a) oxide patch on inner surface after SCC testing, (b) X-ray spectra of point A showing presence of iodine, (c) X-ray spectra of point B showing no iodine.

BRP Medium Burnup

Only one failure, 165E4, from the BRP medium-burnup specimens was examined in the SEM. Specimen 165E4 came from a low-fission-gas-release rod. Specimens from the high-fission-gas-release rod, 165F, were not examined in the SEM because the failures did not occur in the pinhole mode, and these specimens had a high activity level that prevented handling in a glovebox. The failure in specimen 165E4 [325°C, 311 MPa (45.1 ksi), 11.2 ks (3.1 h), 598.0 ks (166.1 h) total test time] is shown in Fig. 4-23. In contrast to previous samples, this specimen showed no visible corrosion product on the inner surface, and the cleaned surface showed no evidence of chemical attack. The exposed fracture exhibited crack branching at ∿200 μm from the inner surface and had a crack length-to-depth ratio of ∿8. At high magnification (Fig. 4-24), no chemical attack could be detected on the fracture surface. The fracture consists of predominantly cleavage-like planes with a small amount of fluting. The final failure mode in this specimen was ductile stress rupture.

BRP High Burnup

One specimen from the high-gas-release-rod 165T was examined in the SEM. The results of the SEM examination on specimen 165W8 (low gas release) have been reported previously (6). The failure from specimen 165T18A [325°C, 151 MPa (21.9 ksi), 2.76 ks (7.7 h)] is shown in Fig. 4-25. The inner surface in the as-tested condition is covered by a large number of deposits, which obscure much of the failure. Note that in some areas the deposits have lifted from the surface. The ultrasonically cleaned surface revealed a failure that is similar in appearance to other low-stress failures, i.e., a tight, single crack. The exposed fracture surface shows a large amount of chemical attack that continues to the outer surface. Crack branching is not observed. At high magnification (Fig. 4-26), the fracture surface shows the large extent of the chemical attack (chemical attack extends to the bottom of the middle composite). Cleavage-like fracture is observed in those areas that are free of chemical attack.

What apparently are CsI crystals were found on some areas along the crack and on the fracture surface. These octahedron-appearing crystals are shown in Fig. 4-27. The presence of cesium and iodine, in approximately equal quantities, was determined by energy-dispersive X-ray analysis. The presence of these crystals on the fracture surface is evidence that the iodine inserted for the test reacted with fission-product cesium on the inner surface. This finding, however, is not necessarily evidence that CsI was the corroding specie. Rather, it may simply indicate that the amount of iodine added was far in excess of that required to initiate cladding attack.

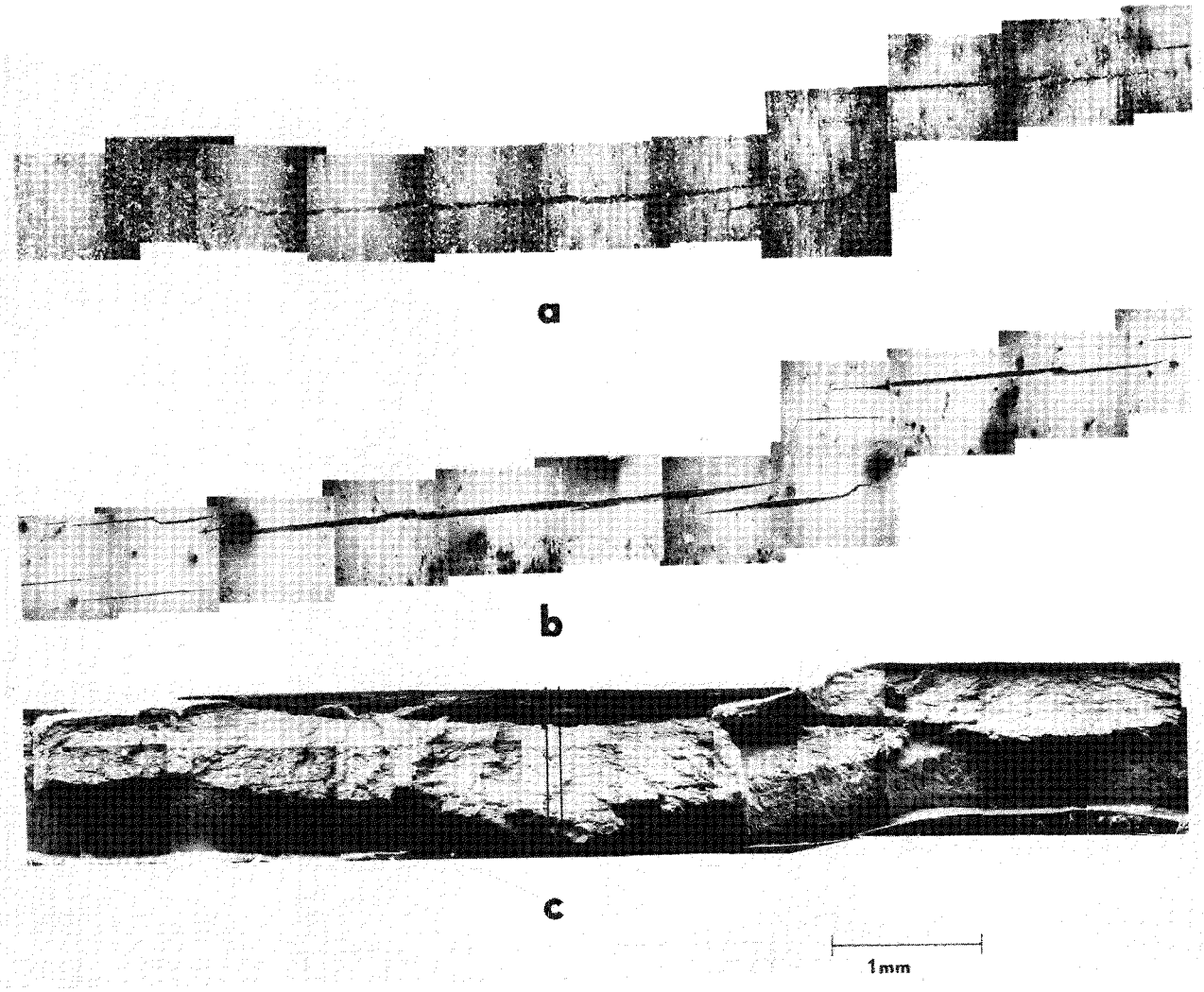

Fig. 4-23. SCC failure in BRP specimen 165E4. (a) as tested, (b) after ultrasonic cleaning, (c) after three-point bending.

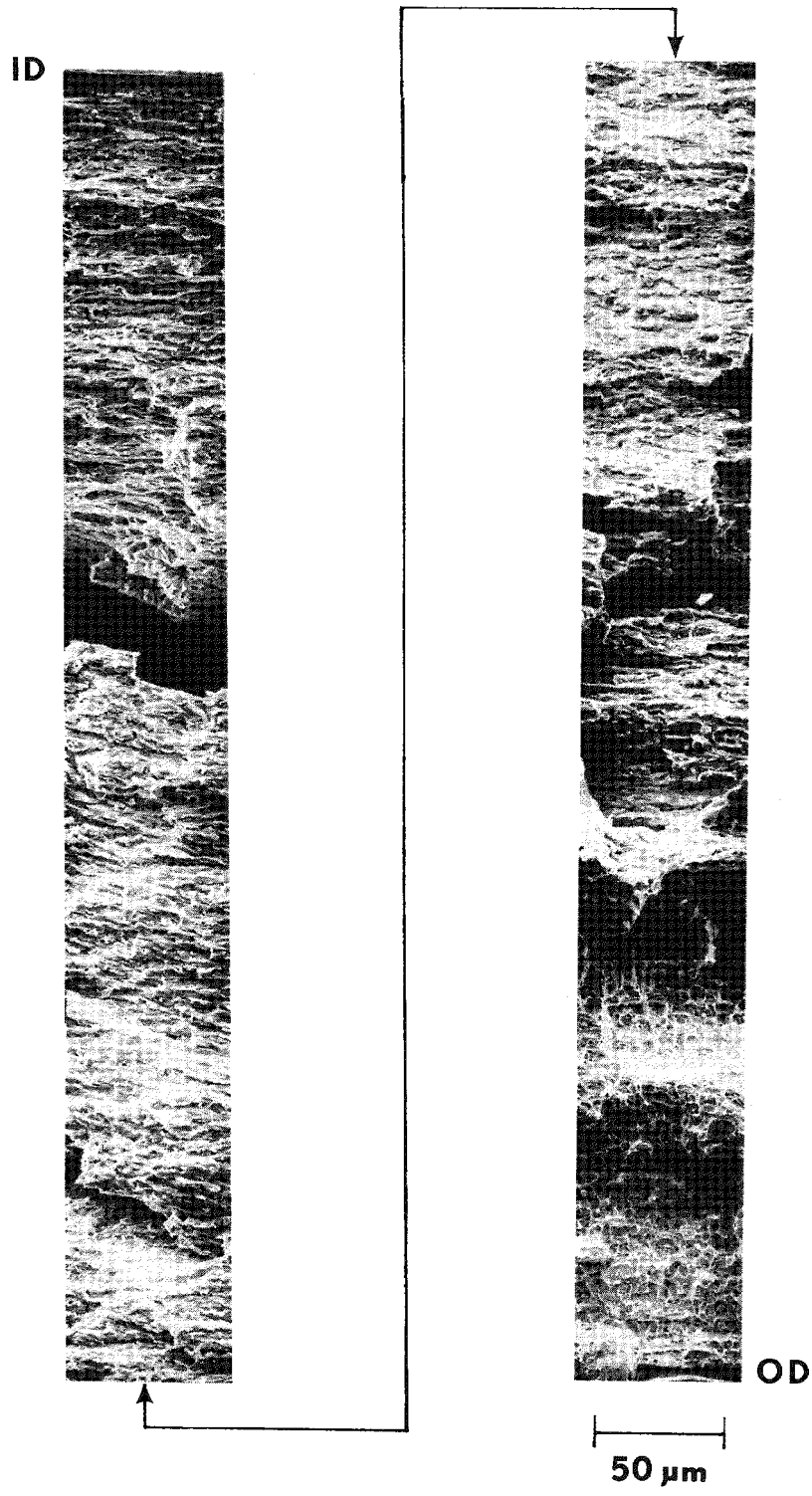

Fig. 4-24. High-magnification composite of fracture surface in BRP specimen 165E4 located between vertical lines in Fig. 4-23c.

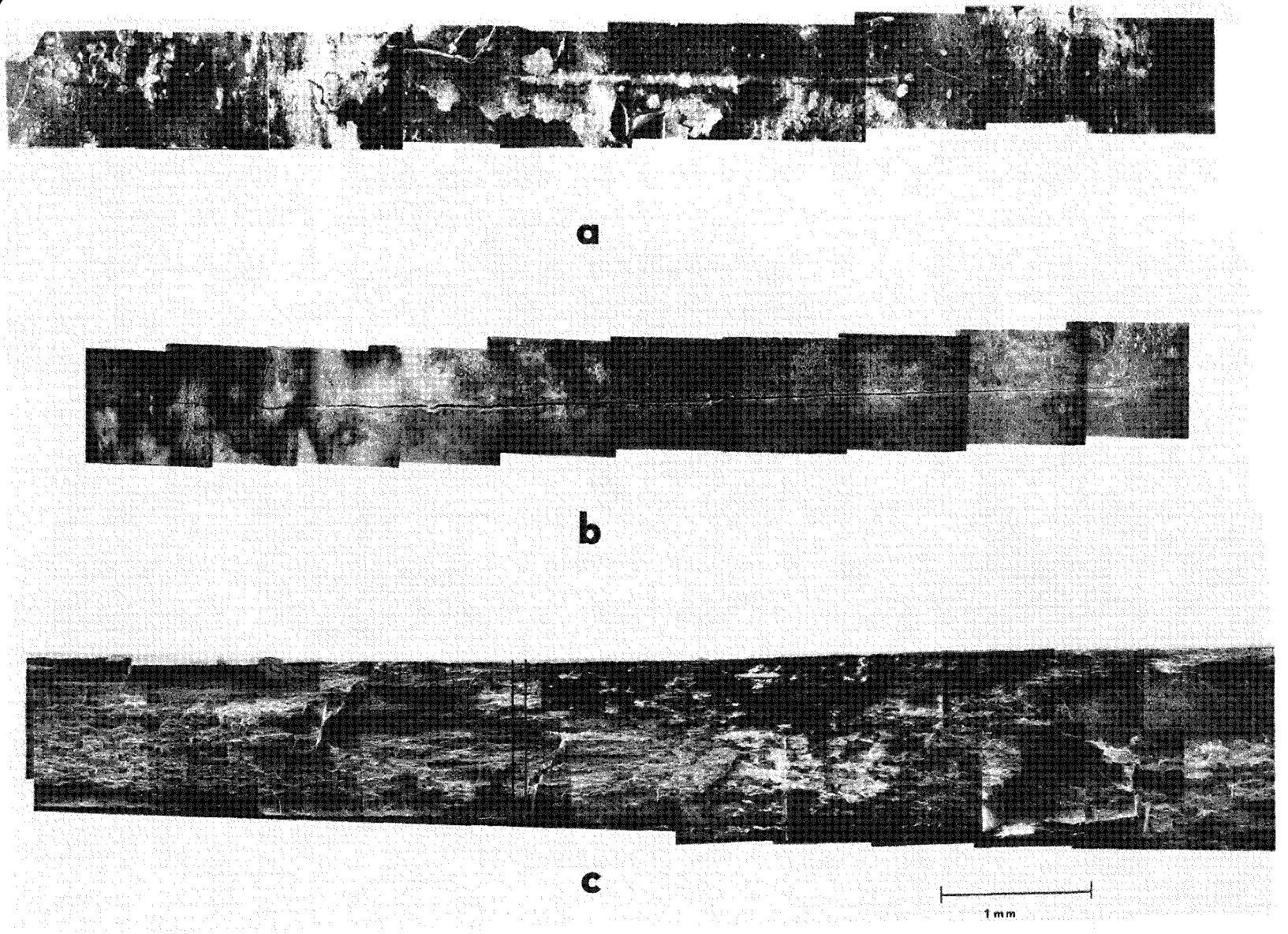

Fig. 4-25. SCC failure in BRP specimen 165T18A. (a) as tested, (b) after ultrasonic cleaning, (c) after three-point bending.

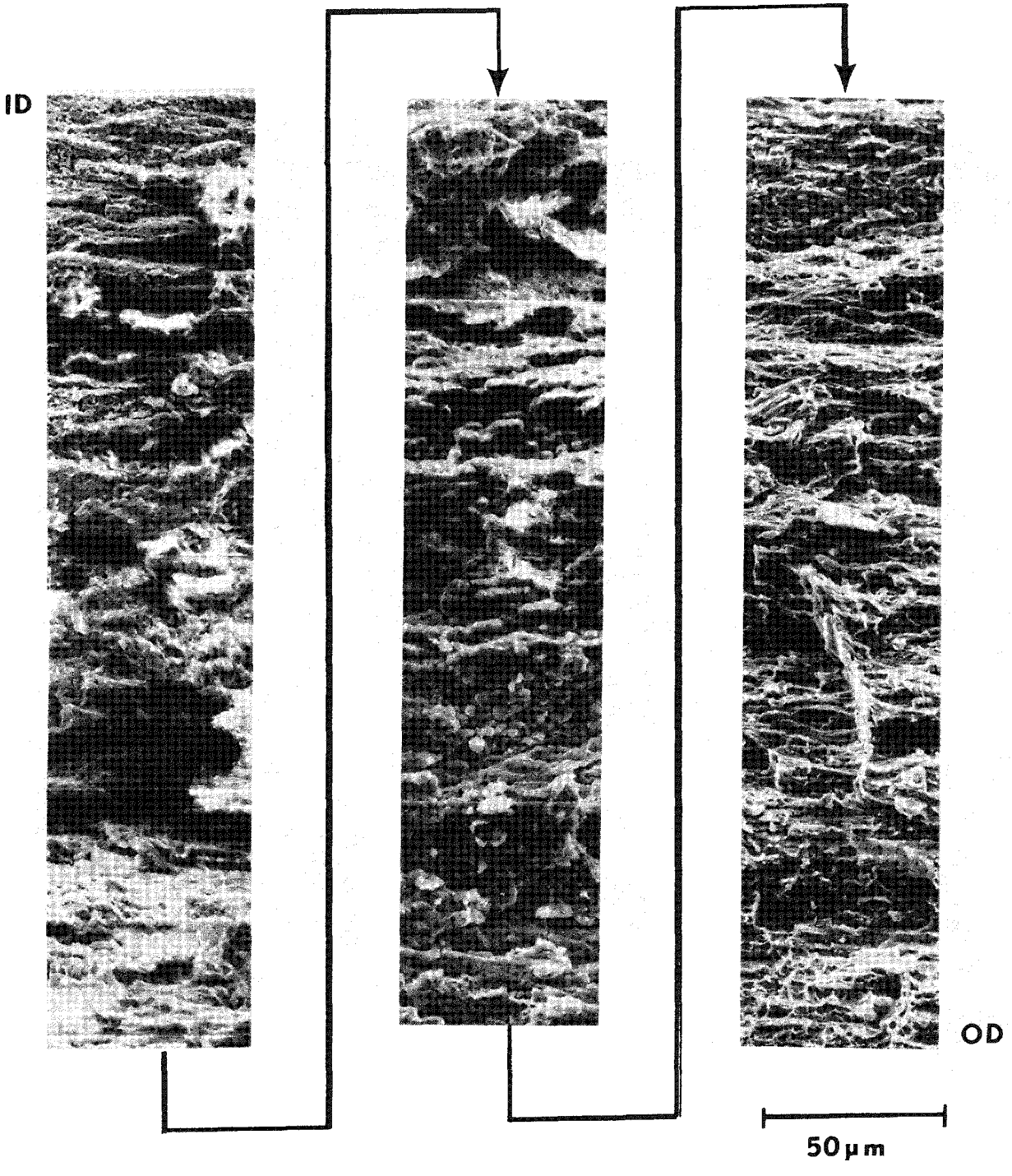

Fig. 4-26. High-magnification composite of fracture surface in BRP specimen 165T18A located between vertical lines in Fig. 4-25c. Chemical attack is observed to the bottom of the middle composite.

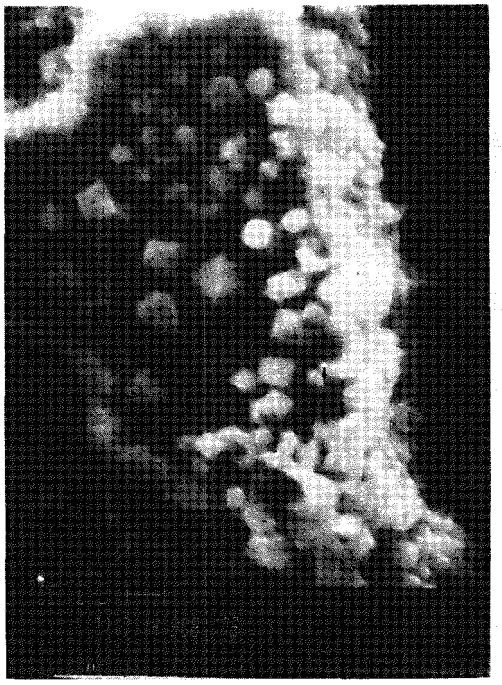

Fig. 4-27. Crystals containing cesium and iodine located along and on crack surface in BRP specimen 165T18A.

Section 5

DISCUSSION

CRACK INITIATION AND GROWTH

Several potential mechanisms can be postulated to affect SCC crack initiation and growth. Crack initiation can be expected to be influenced by both the chemical and physical state of the inner surface as well as the composition and temperature of the environment. The tests and examination performed during the program indicated that the condition of the surface oxide may be an important factor in SCC susceptibility. The presence of a high-quality, thick, unbreached oxide layer was found to provide a barrier to iodine attack, at least to moderate fluence levels of $\sim 1 \times 10^{21}$ n/cm^2. Cladding specimens with this oxide exhibited a high threshold stress of ~280 MPa, which is in the range of the threshold stress for unirradiated stress-relieved cladding (13). It is also higher than what would be expected at that fluence based on the result for lower- and higher-fluence cladding. Failure occurred only after the oxide had been mechanically breached. The absence of chemical degradation of the fracture surface would be indicative of very rapid crack growth following breaching of the oxide. However, when a similar oxide layer was overlaid with significant fission-product deposits, the threshold stress was only ~200 MPa. Metallographic examinations showed that the cracks were located in regions of thinned oxide layer or adjacent to cracks in the oxide. (The latter was simply the result of mechanical loading at the same time the crack was initiated mechanically.) Therefore, it is concluded that a uniform, thick high-quality oxide layer can afford a degree of protection in the absence of significant fission-product deposits, i.e., at gas-release levels of less than ~1%. However, the lifetime to which this protection would be in effect could not be evaluated. The high-burnup BRP cladding from the same manufacturer showed a much smaller difference in threshold stress between low- and high-gas-release rods than the medium-burnup claddings. The observed oxide layers on both the low- and high-gas-release high-burnup claddings were not of the same high quality as that on the medium-burnup cladding that exhibited the high threshold stress, and it is not known whether their preirradiation condition was the same as the medium-burnup cladding. Therefore, it cannot be concluded that a "good" oxide layer degrades with burnup in the absence of fission-product deposits. The slight, but significant, difference

in threshold stress for the high-burnup cladding can then only be attributed to the presence of the fission-product deposits on an already "nonprotective" oxide layer.

The exact role played by these deposits of principally cesium and uranium in affecting crack initiation in our tests, or in-reactor, is a matter of conjecture. Simple mechanical disruption of the oxide exposing the substrate is one possibility, particularly at the edges of the deposits which are distinctly nodular. Another possibility is that the deposits are regions in which the local chemistry existing during irradiation was conducive to the formation of a minor defect, which then grew during our testing. As for the subsequent in-cell tests in which iodine was added, the iodine would be expected to react with the cesium-uranium deposits to form CsI, and indeed crystals containing cesium and iodine were found on a fracture surface. Because CsI has been shown not to cause SCC failure in Zircaloy (15), other surface reactions may have been operative to effect the enhanced cladding attack. The formation of Cs_2ZrO_3, from Cs_2UO_4, at the cladding surface might be one such reaction. In the absence of confirmatory thermodynamic and diffusion data, it would have to be assumed that the penetration of iodine through the cesium reaction products is favored over the penetration through ZrO_2 in order for this mechanism to result in lower threshold stresses for cladding having fission-product deposits.

Impurity inhomogenieties in the cladding would also be sites for the initiation of SCC cracking. Increased attack at sites of iron-rich precipitates has been observed in unirradiated cladding (13). Analysis of pits that formed during our tests indicated that these sites did indeed have an increased iron content. However, close examination of the SCC failures was unable to confirm that the cracks initiated at such iron-rich sites. In the case of a QC specimen, the SCC failure formed directly opposite an inhomogeniety in the form of nodular oxide on the outer surface. The oxide nodule may have acted as a stress intensifier and induced rapid crack initiation and propagation. The time to failure of this specimen was in fact far less than that of other QC specimens tested at similar stresses.

Crack-growth characteristics as inferred from the appearance of the SCC failures were related to the test stress level and time to failure. At stress levels of $\lesssim$241 MPa, the failures consisted of one long crack with a high degree of corrosion product along the crack. The Zircaloy substrate along the cracks exhibited a high degree of chemical attack. The chemical-attack portion of the fracture surfaces was extensive. No evidence of crack branching was observed. At stresses $\gtrsim$241 MPa,

the SCC failures consisted of multiple cracks on the inner surface. The amount of chemical attack was less than that observed in specimens tested at lower stresses. The fractures exhibited crack branching at 100-300 μm from the inner surface. The cleavage-like fracture sometimes ended before the breach reached the outer surface indicating that the final fracture occurred by ductile stress rupture. In either case, the brittle SCC fracture surface cannot be considered to be composed of true cleavage areas, since there are indications of localized ductility. The total amount of fluting observed on the fracture surface represents $\leq$5% of the total area.

EFFECT OF FLUENCE

The interim report showed that specimens from low-gas-release rods receiving a burnup of >10 MWd/Kg U exhibited similar stress vs. time-to-failure curves and an average threshold stress of 177±18 MPa (6). The SCC tests on the low-burnup BRP cladding can be added to these data to examine the effect of fluence over a larger range. The 24-h failure stress for cladding from low-gas-release rods is plotted as a function of fluence in Fig. 5-1. Also shown for comparison is the 24-h failure stress of unirradiated 7AH11-H cladding that was tested at 590 K (17). The general trend shown in Fig. 5-1 is a decreasing failure stress with increasing fluence reflected by an increasing yield strength. The same trend has also been described recently by Lunde and Videm (16). The exceptions to this trend are the medium-burnup BRP cladding and the HBR cladding. As described above, however, it is believed that the reason for the high failure stress of the medium-burnup BRP cladding is the presence of a high-quality oxide layer on the cladding inner surface that prevents iodine penetration to the substrate. The HBR cladding, which came from a PWR, was irradiated at a higher temperature than the other claddings and was tested at 360°C compared with 325°C for the other claddings. Therefore, the relatively high failure stress of the HBR cladding is believed to reflect the different irradiation and test conditions.

The primary effect of irradiation on the bulk properties of Zircaloy cladding from low-gas-release rods is to increase the strength and decrease the ductility (18). The effect of irradiation on the cladding tensile strength is illustrated in Fig. 5-2, which compares the yield strength of 7AH11-7 (17), low-burnup BRP, and QC cladding. Although the number of data points is limited, the trend of a higher yield stress with fluence is clearly evident. The results of Figs. 5-1 and 5-2 can be combined to examine the relationship of the cladding yield stress and the 24-h failure stress. As shown in Fig. 5-3, the limited data indicate that the SCC

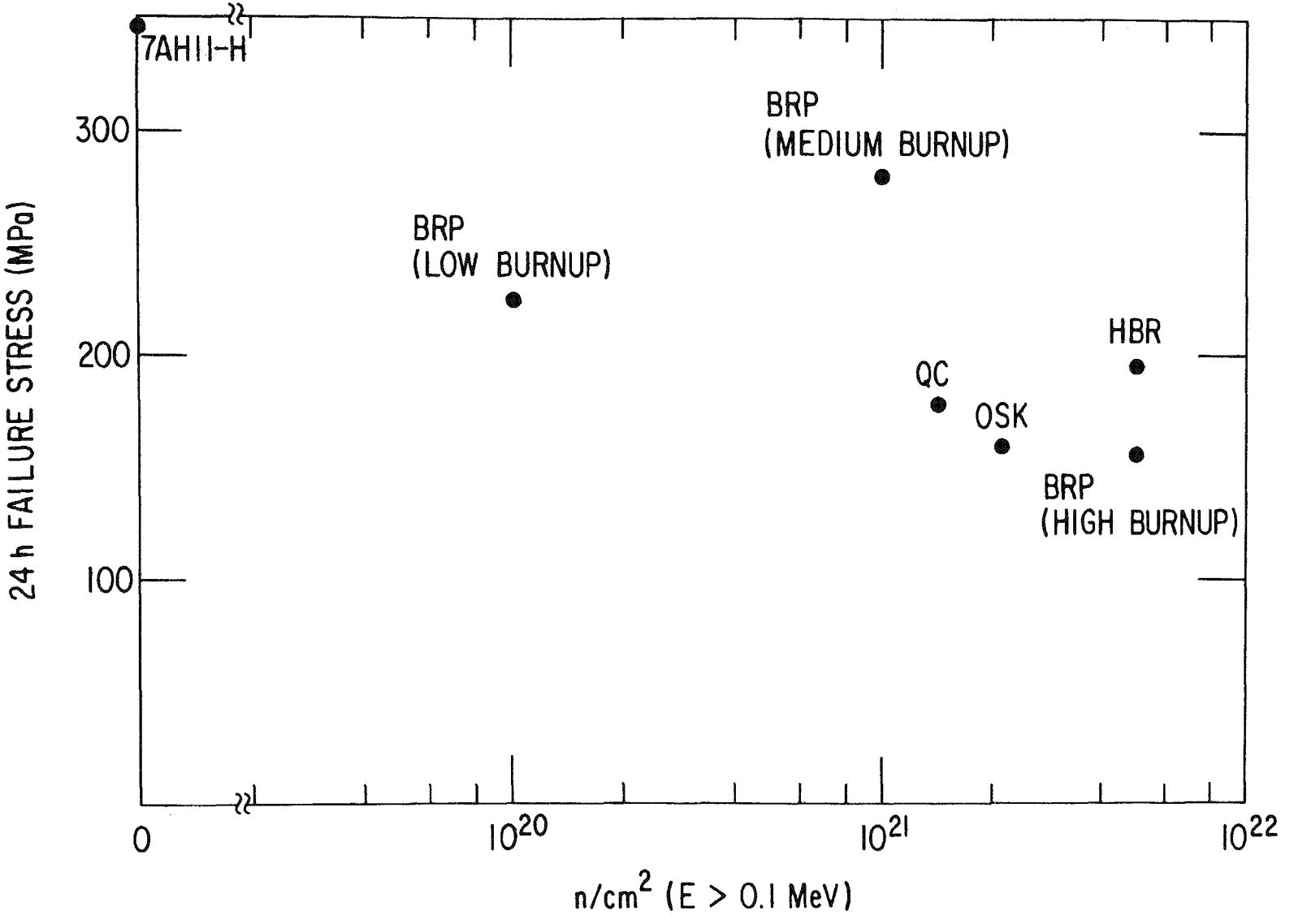

Fig. 5-1. Effect of fluence on the 24-h failure stress of irradiated Zircaloy cladding.

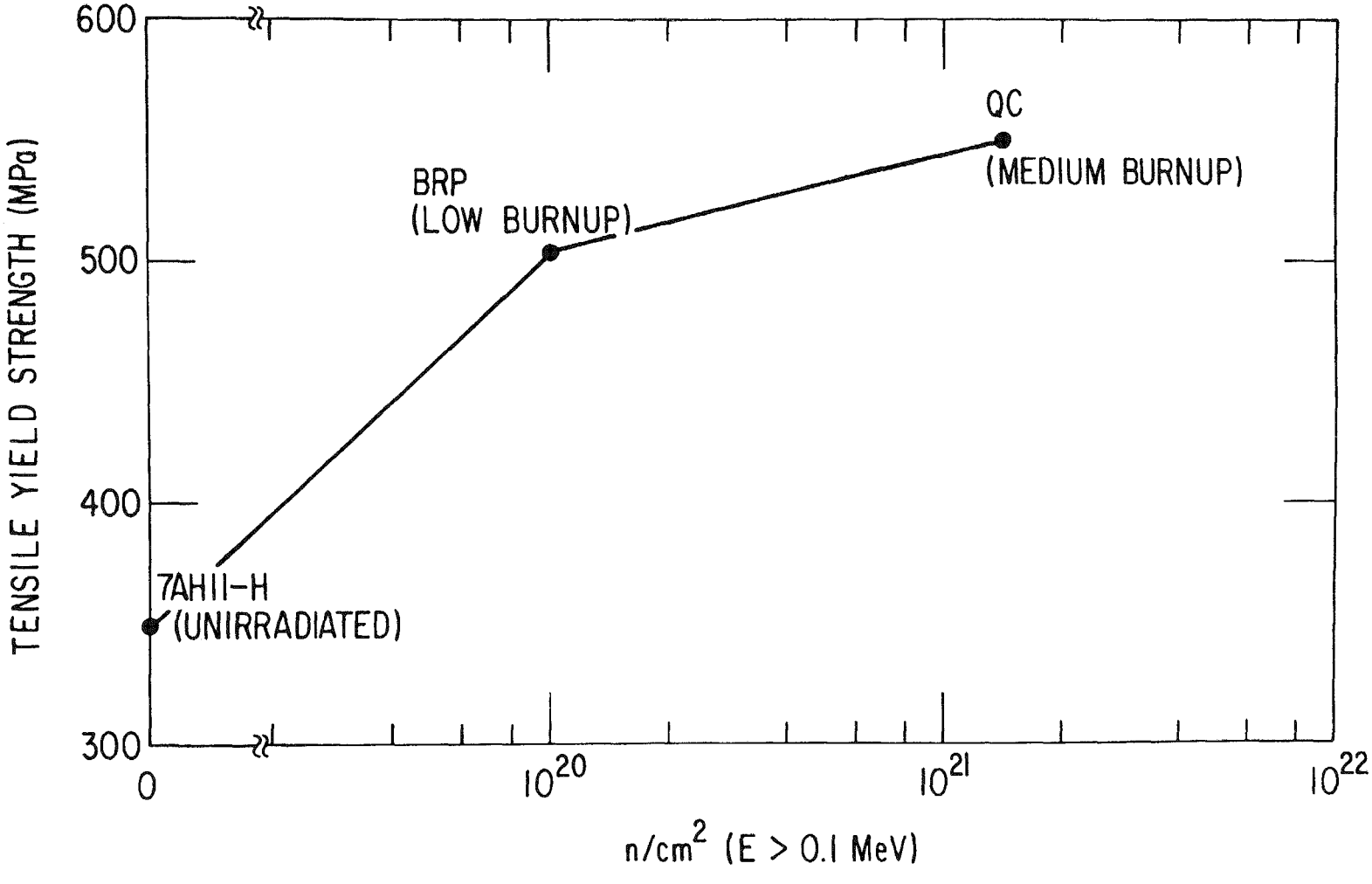

Fig. 5-2. Effect of fluence on the 0.2% yield strength of irradiated Zircaloy cladding.

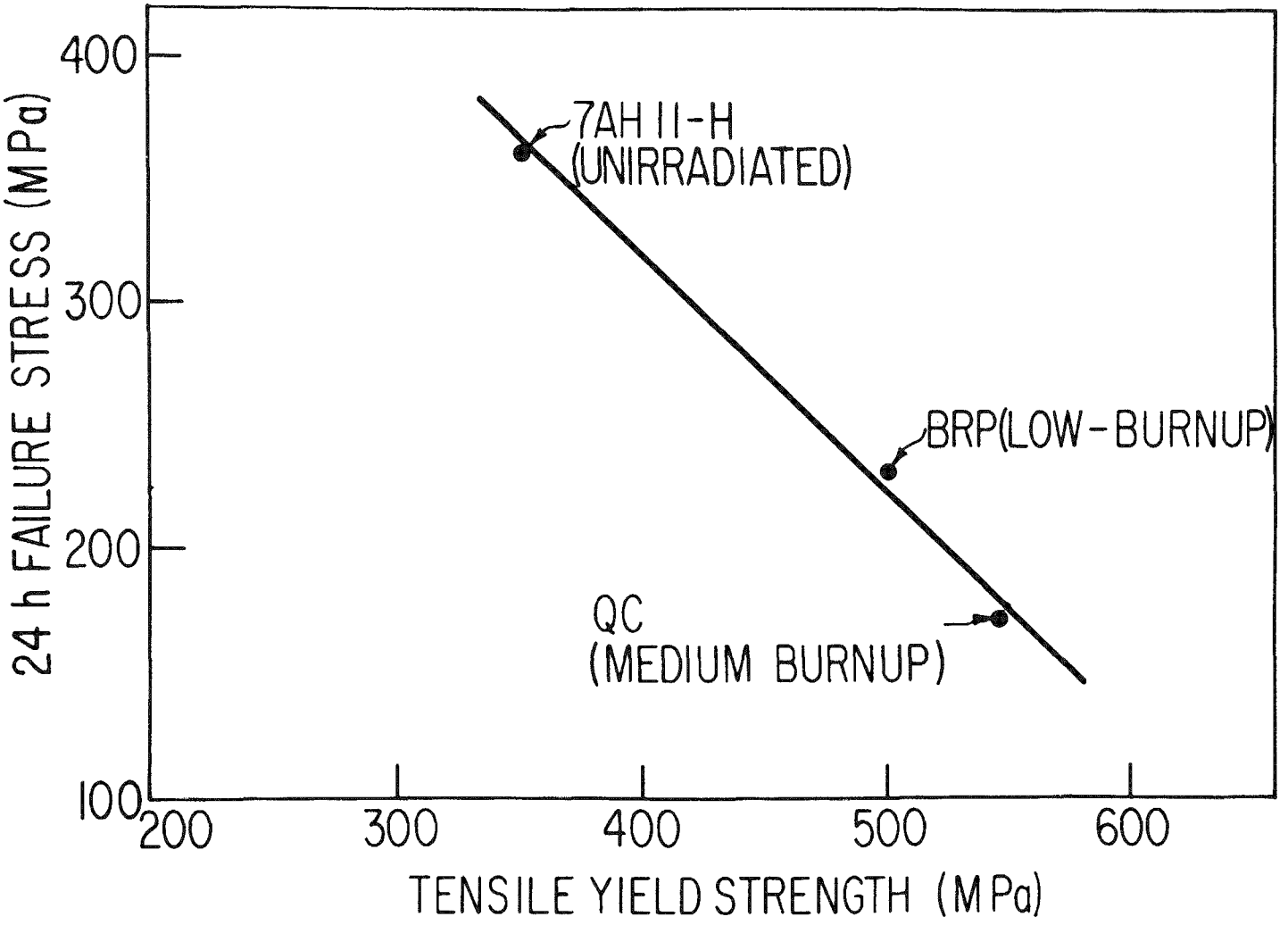

Fig. 5-3. Comparison of 0.2% yield strength and 24-h failure stress for 7AH11-H, QC, and low-burnup BRP cladding.

failure stress decreases linearly with an increasing yield stress. Such a relationship between yield stress and stress-corrosion susceptibility is not unexpected, since similar relationships have been observed in other alloy systems (19). The effect of yield stress on stress-corrosion susceptibility is discussed more completely in the section describing the SCC model.

EFFECT OF TEMPERATURE

The tests of HBR cladding at 276 and 414 MPa (40 and 60 ksi) show a decrease in the time to failure by a factor of 20 and 8, respectively, when the test temperature is increased from 325 to 360°C. A similar effect of temperature has been reported in other experiments with unirradiated cladding (14,18). In one case, the temperature effect was attributed to the variation in tensile properties with temperature; in the other case, the effect was attributed to a thermally activated process, such as the rate at which iodine chemically reacts with the Zircaloy. As shown in the previous section, a change in yield strength, due to a temperature change, may influence the SCC susceptibility (18). Therefore, both the changes in tensile properties and chemical reaction rates with temperature are likely to influence the SCC susceptibility. The effect of temperature on chemical reaction rates is discussed in more detail in the section on the SCC model, where the HBR data are used to ascertain activation energies and rate constants for crack growth.

Cumulative Damage

The results of the cumulative-damage tests are compared in Table 5-1 with the predictions for linear damage accumulation (LDA) and for the SCC model. The predictions for LDA have been made assuming

$$\frac{t_1}{t_{f_1}} + \frac{t_2}{t_{f_2}} = 1 \quad , \tag{5-1}$$

where t_1 is the hold time at the initial stress level σ_1, t_{f_1} is the time to failure at σ_1, t_2 is the time held at the second stress level σ_2, and t_{f_2} is the time to failure at σ_2. The method used for evaluating the time to failure with the SCC model is described later.

The comparison of the results and predictions indicates that, except for tests in which σ_2 is low (<240 MPa), both sets of calculations reasonably approximate the times to failure. In most cases, the LDA calculations are closer to the experimen-

Table 5-1

COMPARISON OF-CUMULATIVE DAMAGE RESULTS AND TIME-TO-FAILURE PREDICTIONS

Specimen Number	Cladding Type	σ_1 MPa	σ_1 (ksi)	t_1 s	σ_2 MPa	σ_2 (ksi)	t_2 s	$\Delta\sigma$* MPa	Total Time s	t_f LDA** s	t_f SCC Model s
190D2-7	QC	274	(39.8)	3.43×10^3	412	(59.7)	4.08×10^2	+138	3.84×10^3	4.72×10^3	4.32×10^3
190D2-8	QC	418	(60.4)	1.15×10^3	279	(40.4)	3.59×10^3	-139	4.74×10^3	5.07×10^3	9.00×10^3
165U-6	BRP	486	(70.5)	7.20×10^2	278	(40.3)	2.71×10^3	-208	3.43×10^3	3.86×10^3	5.04×10^3
165U-13	BRP	480	(69.7)	7.50×10^2	279	(40.5)	3.20×10^3	-201	3.95×10^3	3.78×10^3	5.04×10^3
165U-12	BRP	449	(65.2)	9.6×10^2	242	(35.1)	3.91×10^3	-207	4.87×10^3	4.83×10^3	7.56×10^3
165V-4	BRP	381	(55.2)	1.68×10^3	246	(35.6)	3.10×10^3	-135	4.78×10^3	4.75×10^3	7.20×10^3
165V-6	BRP	189	(27.4)	3.42×10^3	298	(43.1)	3.15×10^3	+109	6.57×10^3	7.44×10^3	9.36×10^3
165T-4	BRP	275	(39.9)	2.70×10^3	152	(22.0)	6.18×10^3	-123	8.88×10^3	1.85×10^6	5.67×10^4
165T-8	BRP	275	(39.9)	2.70×10^3	179	(26.0)	1.31×10^3	-96	4.01×10^3	1.04×10^4	1.64×10^4

*$\Delta\sigma = \sigma_2 - \sigma_1$

** LDA = Linear Damage Accumulation

tal results than the SCC calculations. At low final stresses, both sets of calculations predict much longer times to failure than are observed experimentally. However, the low-stress portion of the time-to-failure curve is close to horizontal, so that a small difference in the assumed position of the curve will lead to large differences in the predicted failure times. Therefore, the large differences between the results and calculations may reflect a lack of sufficient knowledge of the exact form of the low-stress portion of the curve.

The cumulative-damage results are in conflict with tests performed on unirradiated cladding where nonlinear damage accumulation is observed (14). The reasons for the apparent conflict will require further experimentation to resolve. More accurate cumulative-damage measurements will require a more precise stress vs. time-to-failure base curve. Because of the potential influence of inner-surface conditions on the time to failure and the variation of those conditions from rod to rod, each rod should be thoroughly characterized, and specimens from a single rod should be used for both the tests establishing the base curve and the cumulative-damage tests.

MODEL FOR SCC BEHAVIOR

A semiempirical model for the SCC of Zircaloy cladding was developed based on the experimental results of this program. The following paragraphs update the model from its original presentation in the interim report (6) with data that have since been generated.

Temperature Effects

The influence of temperature has been shown experimentally for the HBR cladding. Decreasing the test temperature from 360 to 325°C increased the time-to-failure by factors of 8 and 25. These data have been used to revise the parameters of the original model. The total time to failure, t_f, for an SCC pressurization test is given by

$$t_f = \frac{B}{A_o}\left[\left(\exp\frac{K_{ISCC}^2}{\sigma^2 y^2 B} - 1\right)\right] + \frac{C}{\sigma^4 y^4}\left[\frac{\sigma^2 y^2}{K_{ISCC}^2} - \frac{B}{w(\sigma_B - \sigma)}\right] \qquad (5\text{-}2)$$

where K_{ISCC} is the threshold stress intensity for cleavage and fluting, σ_B is the cladding burst strength, w is the cladding wall thickness, y is a geometric factor ~ 2, σ is the applied stress, and A_o, B, and C are coefficients determined from the test data on irradiated cladding. The first term of Eq. 5-2 represents the time required to chemically grow a crack to a critical length where cleavage and fluting begins; the second term represents the time required to propagate a crack by cleavage and fluting to failure. The coefficient B is assumed to be constant for all cladding and test parameters; A_o and C have been assumed to obey an Arrhenius temperature dependence given by

$$A_o = A_1 \exp(-\Delta H_1/RT);\ C = C_1 K^4_{ISCC} \exp(-\Delta H_2/RT). \quad (5\text{-}3)$$

The threshold stress intensity is assumed to decrease linearly with cladding yield strength.

$$K_{ISCC} = K_o - K_1 \sigma_{ys} \quad (5\text{-}4)$$

The revised coefficients used in Eq. 5-2 are listed in Table 5-2.

The effect of temperature can be related to the rate of crack growth due to chemical attack and cleavage and fluting through the parameters A_o, B, and C. The rate of crack growth, $\dot{a}$, due to chemical attack is assumed to be

$$\dot{a} = A_o \exp(-a/B). \quad (5\text{-}5)$$

From Table 5-2, the initial rate of crack growth is calculated to be 0.64 μm/s at 360°C and 0.067 μm/s at 325°C. The rate of crack growth is predicted to decrease by a factor of 1/e every 36.5 μm. The crack growth rate due to cleavage and fluting is assumed to be

$$\dot{a} = K^4/C \quad (5\text{-}6)$$

For a stress intensity on the order of 10 MPa · $m^{1/2}$, the crack growth rate is predicted to be 1.3 μm/s at 360°C and 0.26 μm/s at 325°C. The difference in the rates of crack growth for chemical attack and for cleavage and fluting indicates that most of the total time to failure is spent growing the crack by chemical attack and a relatively short period of time is spent propagating the crack by cleavage and fluting.

Table 5-2

SCC MODEL PARAMETERS

Parameter	Value
A_1	4.14×10^{10} m/s
ΔH_1	49 kcal/mole
B	36.5 μm
C_1	1.18×10^{-5} m·s^{-1}·MPa^{-4}
ΔH_2	35 kcal/mole
K_o	25.1 MPa·m$^{1/2}$
K_1	0.032 m$^{1/2}$

Effect of Yield Strength on Time to Failure

As shown in Eq. 5-4, a linear relationship has been assumed to exist between K_{ISCC} and the cladding yield stress. The tensile tests conducted in the program make it possible to test this hypothesis. At long times to failure (>10 h), the time to chemically grow a crack to a critical length where cleavage and fluting begins is predicted to take the great majority of the total time to failure, i.e.,

$$t_f \approx \frac{B}{A_o} \exp \left(\frac{K^2_{ISCC}}{\sigma^2 y^2 B} \right) \tag{5-7}$$

For a constant time to failure, say 24 h, Eq. 5-6 can be reduced to

$$K_{ISCC} \propto \sigma \text{ (24-h failure stress)}$$

or

$$K_o - K_1 \sigma_{ys} \propto \sigma \text{ (24-h failure stress)} \tag{5-8}$$

The SCC model thus predicts that a linear relationship should exist between the cladding yield stress and the stress required to produce an SCC failure in 24 h.

The 24-h failure stress and the tensile yield stress is compared in Fig. 5-3 for the QC and BRP-low-burnup cladding tested at 325°C and for unirradiated 7AH11-H cladding tested at 320°C (17). The relationship between the 24-h failure stress and the tensile yield stress is approximately linear, which means that the SCC model is self-consistent. Other factors, notably the inner-surface condition, may influence the SCC susceptibility. However, the irradiated claddings compared in Fig. 5-3 had both relatively clean inner surfaces and a thin or nonuniform oxide layer. Therefore, the differences in the mechanical properties are believed responsible for the different susceptibilities to iodine SCC. The impact of the inner-surface condition on SCC has been discussed previously.

Time-dependent Parameters

The SCC model has been modified to calculate the crack growth and time to failure for time-dependent input parameters. The model has already incorporated the effects of temperature and stress, but not the effects of iodine concentration. The

effect of iodine concentration on time to failure has been evaluated by Kreyns et al. (20) and Peehs et al. (21) and was determined to be an inverse relationship. This inverse relationship has been assumed for both the coefficients A_o and C up to a saturation level of 0.5 mg/cm^2. This value of 0.5 mg/cm^2 was chosen, somewhat arbitrarily, as the saturation level, because it is near the 0.6-mg/cm^2 iodine concentration used for this investigation and is considerably above the value of 0.06 mg/cm^2 that has been shown to result in greatly increased time to failure in unirradiated cladding (13).

The crack length increase is evaluated for short time increments, where the change in test parameters is small, using the relationships

$$\frac{\Delta a}{\Delta t} = A_o \exp(-a/B) \tag{5-9}$$

when $a < a_c$, and

$$\frac{\Delta a}{\Delta t} = \frac{K^4}{C} \tag{5-10}$$

when $a_c < a < a_f$. The parameters a_c and a_f represent the crack lengths where cleavage fracture begins and where cladding failure occurs by stress rupture, respectively. They are given by

$$a_c = \frac{K^2_{ISCC}}{\sigma^2 y^2} \tag{5-11}$$

and

$$a_f = \frac{w(\sigma_B - \sigma)}{\sigma_B}$$

As an illustration, the crack growth in unirradiated and irradiated cladding has been modeled for a hypothetical power ramp (Fig. 5-4). In this power ramp, the cladding temperature, hoop stress, and iodine concentration are allowed to increase with time up to 0.6 h. The crack growth has been calculated using the above relationships with the additional assumption that iodine attack of the

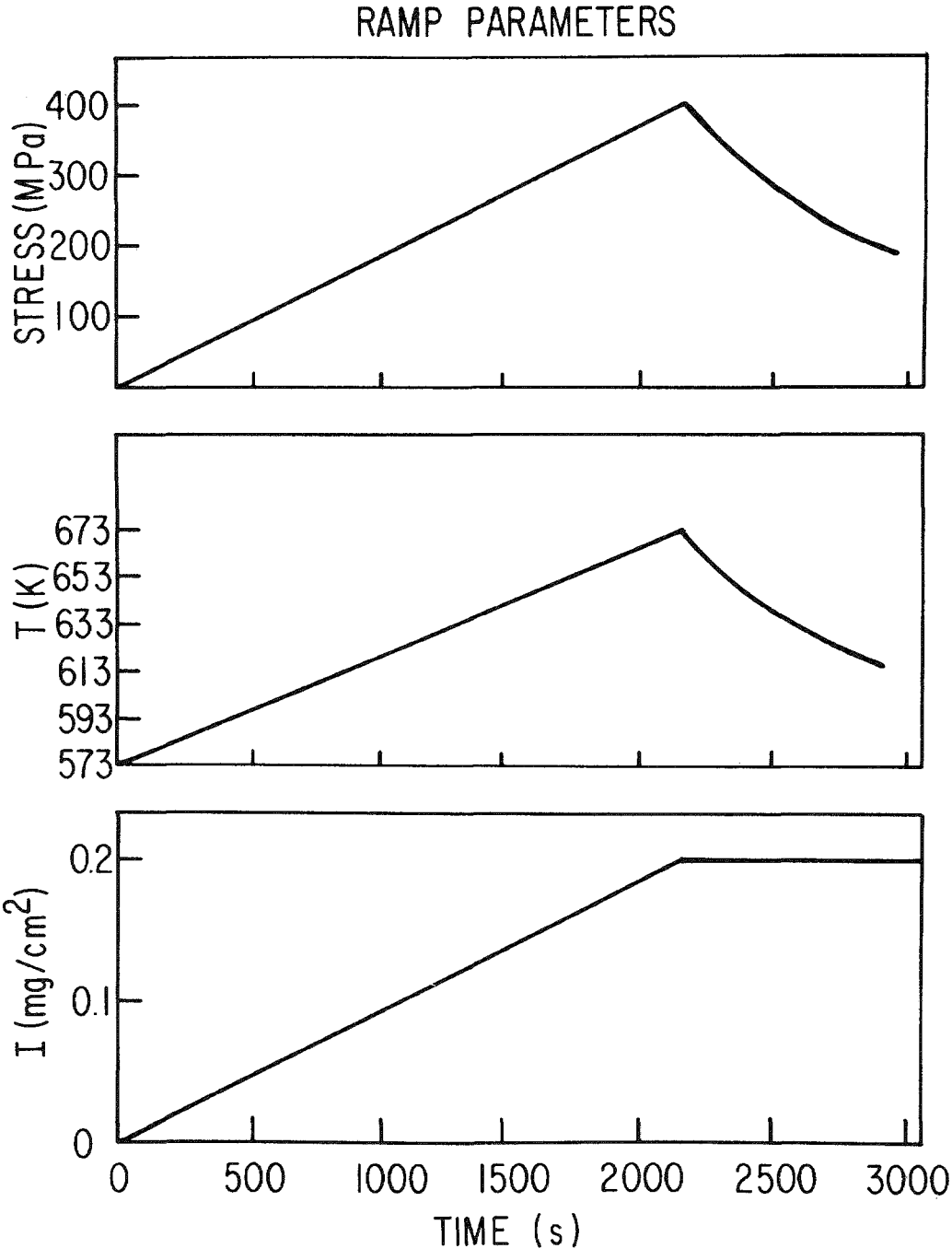

Fig. 5-4. Change in variables with time for a hypothetical power ramp.

cladding cannot occur until the inner-surface oxide has cracked. The stress level chosen as that necessary for oxide cracking is 135 MPa. The results of crack-growth calculations for unirradiated cladding (σ_{ys} = 483 MPa, σ_B = 550 MPa) and irradiated cladding (σ_{ys} = 620 MPa, σ_B = 690 MPa) are shown in Figs. 5-5 and 5-6, respectively. For the unirradiated cladding, crack growth by chemical attack begins at 0.2 h and continues during the ramp. However, the crack length never reaches the critical length, a_c, for the initiation of cleavage and fluting. In the irradiated cladding, chemical attack occurs in the same way, but the critical length, a_c, is reached after ~0.48 h. Failure occurs shortly thereafter because of the rapid crack growth by cleavage and fluting. About 85% of the time to failure for this illustration is spent chemically growing a crack to <10% of the cladding thickness. The predictions of the cumulative-damage tests shown in Table 5-1 have been calculated with these techniques.

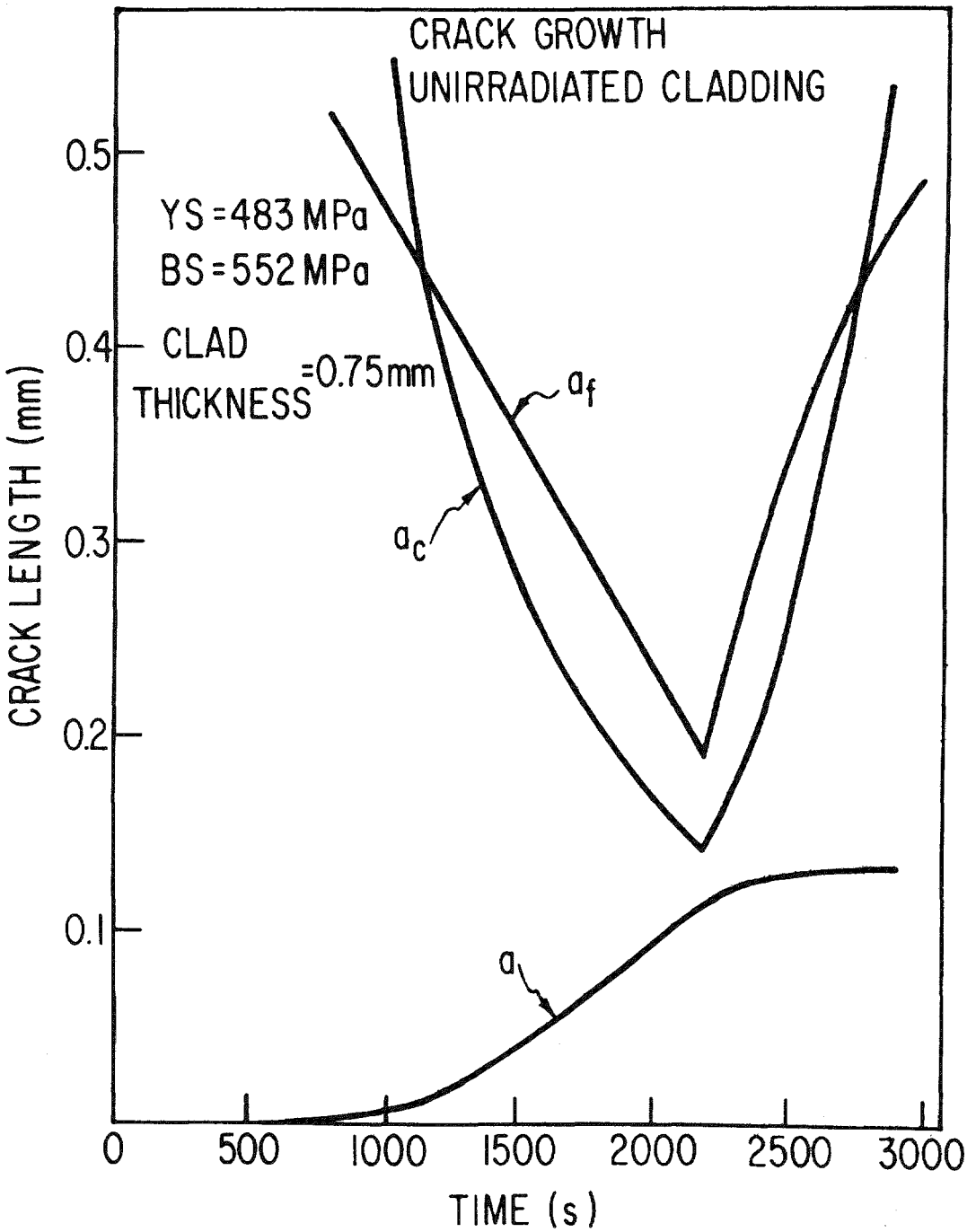

Fig. 5-5. Change in crack length in unirradiated Zircaloy cladding for the power-ramp conditions illustrated in Fig. 5-4. Also shown are the critical crack lengths where cleavage and fluting begin (a_c) and where failure occurs by stress rupture (a_f).

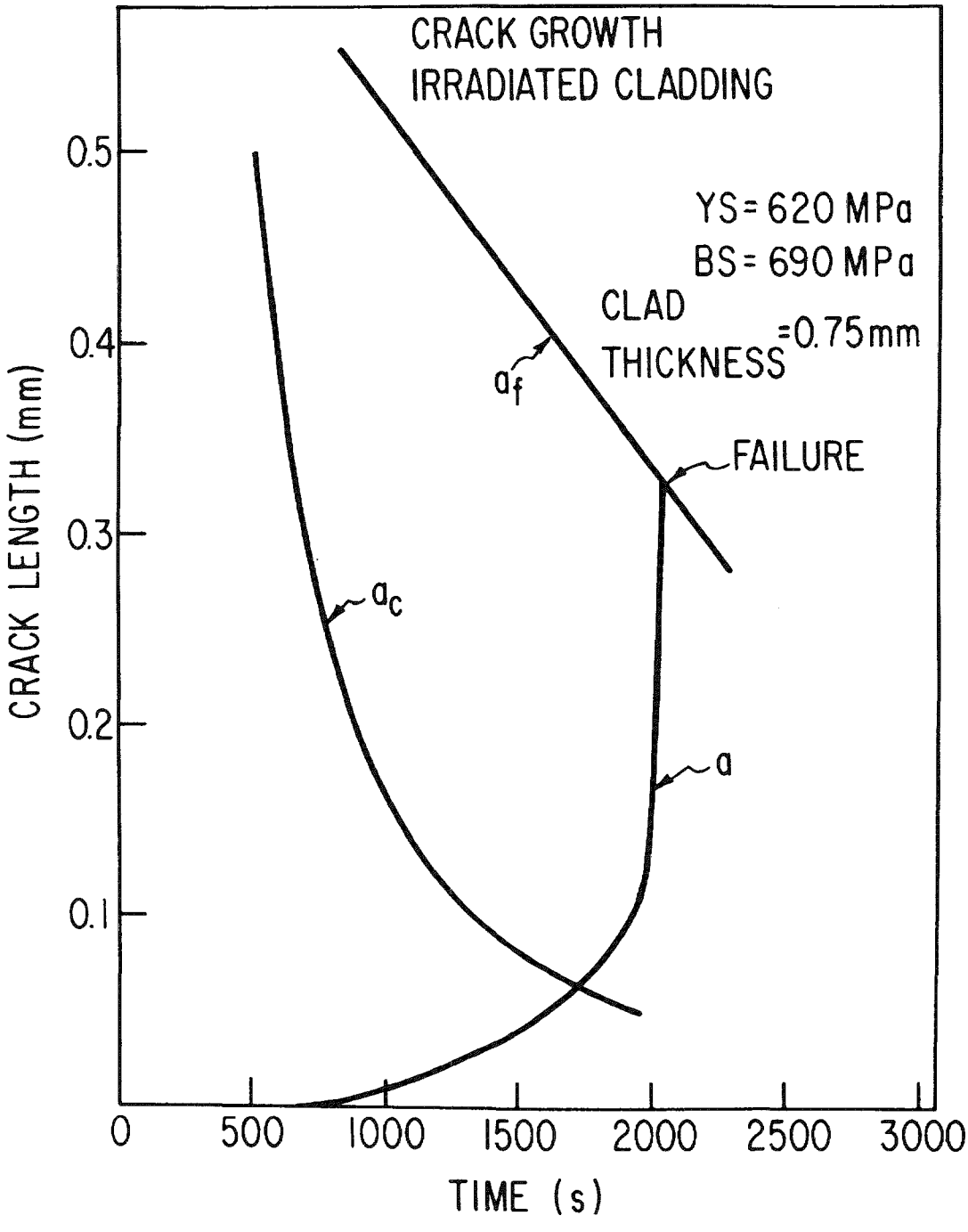

Fig. 5-6. Change in crack length, a, in irradiated cladding for the power ramp conditions illustrated in Fig. 5-2. Also shown are the critical crack lengths where cleavage and fluting begin (a_c) and where failure occurs by stress rupture (a_f).

Section 6

CONCLUSIONS

Several conclusions can be drawn from the work performed on irradiated Zircaloys.

1. Irradiation, in general, increases the susceptibility of Zircaloy to iodine SCC. For cladding from low-gas-release rods with burnups $\geq$10 MWd/kg U, the 24-h failure stress is $\sim$171$\pm$18 MPa (24.8$\pm$2.6 ksi) at 325°C, regardless of the preirradiation metallurgical condition.

2. Both temperature and fluence can have significant effects on the time to failure. Increasing the temperature from 325 to 360°C reduces the time to failure by a factor of 8 to 25. The effect of fluence on SCC appears to be related to the change in mechanical properties with irradiation.

3. A uniformly thick zirconium oxide layer can reduce the susceptibility of irradiated cladding to SCC in the absence of extensive fission-product deposits.

4. SCC susceptibility can be related to fission-gas release and the quantity of fission products on the cladding surface. For medium-burnup BRP ($\sim$8 MWd/kg U) cladding, the fission products appear to break down the protective oxide layer on the inner surface. For high-burnup BRP cladding (24 MWd/kg U), the exact nature of the fission-product-cladding interaction is unknown.

5. SCC failures usually occur at very low strains. In many cases, there was no observable posttest strain.

6. For the test conditions used, SCC crack initiation was not difficult, and multiple crack sites were always found around the circumference of the cladding.

7. The appearance of SCC failures can be related to the test stress. At stress $<\sim$250 MPa, the failures consisted of a single crack which did not exhibit crack branching. Chemical attack of the inner surface and fracture surface was extensive. At stresses $>\sim$270 MPa, the failures consist of multiple cracks, which exhibited crack branching 100-300 μm from the inner surface.

8. Limited data suggest a correlation between postirradiation tensile yield strength and the threshold stress for SCC failure, with the higher the yield strength the lower the threshold stress.

9. Limited cumulative-damage data show that irradiated Zircaloy exhibits a linear cumulative-damage behavior at 325°C in stress decrement tests when $-\Delta\sigma$ is large. This is in contrast to the nonlinear cumulative-damage behavior reported for unirradiated Zircaloy.

Section 7

REFERENCES

1. N. Fuhrman et al., Evaluation of Fuel Performance in Maine Yankee Core I - Task C, EPRI NP-218 (1976).

2. E. Smith and A. K. Miller, Stress Corrosion Fracture of Zircaloy Cladding in Fuel Rods Subjected to Power Increases: A Model for Crack Propagation and Failure Threshold Stress, J. Nucl. Mater., 80, 291 (1979).

3. B. Cox, J. C. Wood, Iodine Induced Cracking of Zircaloy Fuel Cladding - A Review, Corrosion Problems in Energy Conversion and Generation, p. 298 (1974).

4. H. S. Rosenbaum, Electrochem. Technol. 4, 153 (1966).

5. W. T. Grubb and M. H. Morgan III, Cadmium Embrittlement of Zircaloy-2, Proc. ANS Topical Meeting on Water Reactor Fuel Performance, p. 295 (1977).

6. F. L. Yaggee, R. F. Mattas, and L. A. Neimark, Characterization of Irradiated Zircaloys: Susceptibility to Stress-Corrosion Cracking, EPRI-NP-1155 (1979).

7. F. L. Yaggee, R. C. Haglund, and R. F. Mattas, In-Cell Test Facility for Performing Mechanical-Property Tests on Irradiated Cladding, Proc. 26th Conf. on Remote Systems Technology (March 1979).

8. D. G. Farwick and R. A. Moerr, Properties of Light Water Reactor Spent Fuel Cladding, HEDL-TME-78-70 (August 1979).

9. Handbook of Chemistry and Physics, 53rd Edition, Chemical Rubber Company (1972-1973).

10. O. Kubaschweshi, E. L. Evans, and C. B. Alcook, Metallurgical Thermochemistry, 4th Edition, Pergamon Press, New York, 1967.

11. F. Gazarolli, R. Manzel, M. Peeks, and H. Stehle, Observations and Hypothesis on Pellet-Clad Interaction Failures, Kerntechnik, 20 27-30 (1978).

12. R. J. Roache, Formulas for Stress and Strain, McGraw Hill Book Co., New York, 4th Edition (1965).

13. D. Cubicciotti and R. L. Jones, EPRI-NASA Cooperative Project on Stress Corrosion Cracking of Zircaloys

14. D. Cubicciotti, R. L. Jones, and B. C. Syrett, Stress Corrosion Cracking of Zircaloys, EPRI-NP-1329 (1980).

15. K. Une, Influences of Cs and Cs Oxide on Iodine Stress Corrosion Cracking, J. Nucl. Mater., 87, 207 (1979).

16. L. Lunde and K. Videm, The Influence of Environmental Variables and Irradiation on Iodine Stress Corrosion Crack Initiation and Growth in Zircaloy, presented at IAEA Specialists' Meeting on Water Reactor Fuel Element Performance Computer Modeling, Blackpool, March 17-21, 1980

17. H. Ocken, private communication.

18. D. L. Hagman and G. A. Reymann, editors, "MATPRO-Version II," NUREG/CR-0497 TREE-1280 (1979).

19. W. H. Gerberich, "Effects of Hydrogen on High-Strength and Martensitic Steels," Hydrogen in Metals, American Society for Metals, 115, (1973).

20. P. H. Kreyns, G. L. Spahr, and J. E. McCauley, An Analysis of Iodine Stress Corrosion Cracking of Zircaloy-4 Tubing, J. Nucl. Mater., 61, 203 (1976).

21. M. Peehs, H. Stehle, and E. Steinberg, Out-of-Pile Testing of Iodine Stress Corrosion Cracking in Zircaloy Tubing Under the Aspect of the PCI-Phenomena, presented at the Fourth Int. Conf. on Zirconium in the Nuclear Industry, Stratford-upon-Avon, England, June 26-29, 1978.